CONSTRAINING THE FORMATION HISTORY OF THE GALACTIC DISK AND HALO SYSTEMS THROUGH KINEMATIC STUDIES OF METAL-POOR STARS

A Dissertation

Submitted to the Graduate School
of the University of Notre Dame
in Partial Fulfillment of the Requirements
for the Degree of

Doctor of Philosophy

by

Sarah E. Dietz

Timothy C. Beers, Co-Director

Vinicius M. Placco, Co-Director

Graduate Program in Physics
Notre Dame, Indiana
December 2020

CONSTRAINING THE FORMATION HISTORY OF THE GALACTIC DISK AND HALO SYSTEMS THROUGH KINEMATIC STUDIES OF METAL-POOR STARS

Abstract

by

Sarah E. Dietz

The analyses presented in this work all fall under the umbrella term “Galactic archaeology”, the sub-field of astronomy dedicated to reconstructing the assembly and chemical-evolution history of the Galaxy. The following chapters chart a journey through the Milky Way, from the disk system to the stellar halo and the outskirts of the Galaxy, identifying stellar chemo-dynamical patterns that may shed light on the complex mechanisms involved in forming these components. In particular, I use metal-poor stars, and their close associates, carbon-enhanced metal-poor (CEMP) stars, throughout my analyses as tracer populations (or stellar “fossils”) to map features of interest. In the thick-disk, I identify two unusual CEMP populations, and describe their potential implications for the history of the disk system, potentially supporting a separable metal-weak thick-disk (MWTD) component. In the halo, I compare two CEMP-based methods for verifying the inner- and outer-halo separation, and cover the recent changes to our understanding of the halo following the release of high-precision astrometry from the *Gaia* satellite. At the outskirts of the halo, I present evidence of an asymmetric metallicity gradient within this region, and discuss its implications for the complex accretion history of the outer-halo component.

CONTENTS

FIGURES

TABLES

ACKNOWLEDGMENTS

The text within this document represents all my efforts as a graduate student over the last six years; it would not have been possible to produce without significant support from so many people.

To my family and friends—thank you for acting as a sounding board for my graduate school-related worries and anxieties. Without your constant presence, emotional support, and uplifting humor, I would not have been able to come so far.

To my advisors, colleagues, and mentors—thank you for all you've done over the past several years to help me navigate graduate school. Your knowledge, passion, and kindness have helped mold me into a better researcher and a better person.

CHAPTER 1

INTRODUCTION: GALACTIC ARCHAEOLOGY

Researching the history of our Universe from our limited vantage point within it is a complex undertaking. Information on even the planets inside our own Solar System can be immensely difficult to obtain, let alone estimations on the ages, masses, and compositions of stars thousands of light-years away and galaxies billions of light-years from our own. Despite this, astronomers across various sub-fields have developed methods to accumulate a wealth of data on the planets, the stars, and the Universe at large.

The main components of the Milky Way, as we understand it today, consist of a central bulge, a disk system (with a "thin" and "thick" component), a halo system (with an "inner" and "outer" component), and a dark-matter halo, as shown in the lower panel of Figure 1.1. The upper panel of Figure 1.1 contains, for contrast, a schematic of the Galaxy from Herschel (1785). Our understanding of the Milky Way has evolved dramatically in the $\sim$200 years since this figure was produced, a result of both the progresses made in the field of physics and ever-improving observational technologies.

The analyses presented in this work concern the area of "Galactic archaeology": the scientific effort to reconstruct the formation history and chemical evolution of the Milky Way's components, in order to better understand the past and present Universe. This field has progressed rapidly in the past century, and with it so has our understanding of the structure and history of our Galaxy; some of the most notable findings are outlined below.

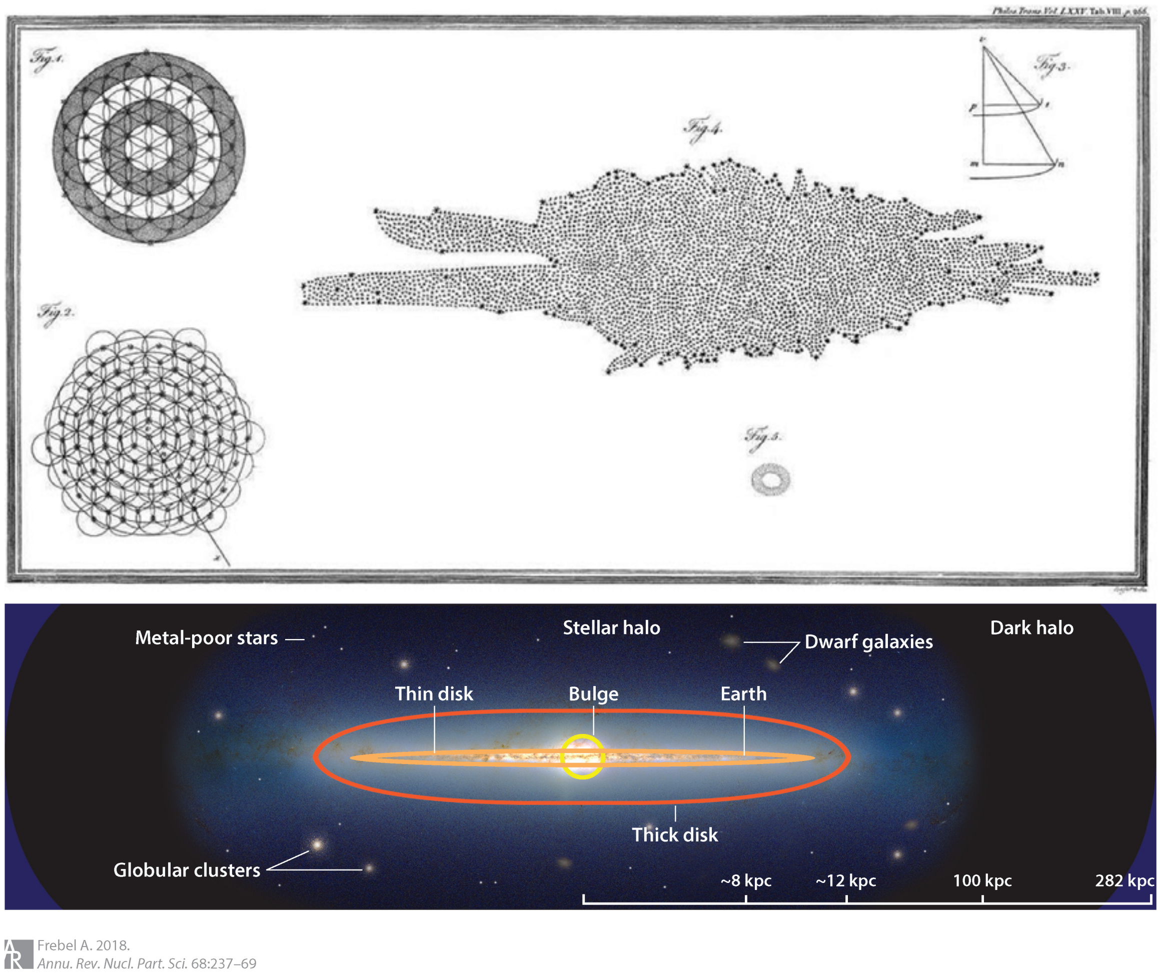

Figure 1.1. Top: Diagram of the Milky Way (with the Sun near the center) from Herschel (1785). Bottom: Diagram of the Milky Way, with key Galactic components and features highlighted, from Frebel (2018).

In the early 1950s we see the first recognition of the now-ubiquitous metal-poor star phenomenon (Chamberlain and Aller 1951; see Section 1.1), and even the first hints of the carbon-enhancement signature now strongly associated with this category (Schwarzschild and Schwarzschild 1950; see Section 1.2). Eggen et al. (1962) famously attempted a reconstruction of the Galactic assembly history, positing a "monolithic collapse" scenario, with only $\sim$200 data points—a history challenged by the accretion-based model of Searle and Zinn (1978), who used a similarly small number of globular clusters in their analyses. The 1980s saw the introduction of the thick-disk component, first formally proposed by Yoshii (1982) and confirmed by Gilmore and Reid (1983), who demonstrated the need for an additional disk component when constructing Galactic density models. The existence of a further, and perhaps even more ancient, disk component was later suggested by Morrison et al. (1990), the so-called metal-weak thick-disk (MWTD). Ibata et al. (1994) provided the scientific community with a stellar example of galactic accretion in real-time by identifying the ongoing tidal disruption of the Sagittarius dwarf galaxy. The long-established ancient stellar halo was shown by Carollo et al. (2007) to contain both an inner and outer (counter-rotating) component, a dichotomy which had been suggested by previous analyses (e.g., Norris 1994) but not yet formally recognized.

Even more recently, a new era of "big data astronomy" is dawning. Thirty years ago, the launch of the Hipparcos satellite produced a catalog of high-precision astrometric data for $\sim$100,000 stars (Perryman et al., 1997); today, the *Gaia* space telescope provides high-quality astrometry for some billion objects within the Milky Way (Gaia Collaboration et al., 2016, 2018). This data, in combination with chemical abundance measurements from massive surveys such as the Sloan Digital Sky Survey (SDSS; York et al. 2000), Large Sky Area Multi-Object Fiber Spectroscopic Telescope (LAMOST; Zhao et al. 2012) survey, or SkyMapper Southern Sky Survey (SMSS; Keller et al. 2007), provides unprecedented insight into the history of our

Galaxy. The *Gaia* data releases have birthed more discoveries than can briefly be mentioned here, among them: the massive *Gaia*-Enceladus/*Gaia* Sausage inner-halo progenitor, the Sequoia galaxy that formed a large portion of the outer-halo, the Splashed Disk, and so on.[1]

Through Galactic archaeology we aim to improve our understanding of the stars, our Galaxy, and the early Universe. In this work I utilize a combination of precise, *Gaia*-sourced stellar kinematics and both spectroscopic and photometric chemical abundances to analyze the behaviors of stellar populations in the disk and halo systems of our Galaxy, beginning with the thick-disk system in Chapter 3, then moving into the dual halo in Chapter 4, finally traveling to the outer edges of the Milky Way in Chapter 5. In each of these chapters I examine the chemo-dynamical traits of various stellar populations to help constrain the assembly histories of these Galactic components. Below, I give an overview of a topic key to all following chapters: the role of metal-poor stars in Galactic archaeology.

1.1 Metal-Poor Stars as Stellar Fossils

In astronomy, all elements heavier than hydrogen and helium are commonly referred to as "metals". The sole elemental by-products of the Big Bang were hydrogen, helium, and a minuscule amount of lithium; today, the Universe is still largely comprised of hydrogen and helium, but heavier elements have since been synthesized by stars via a variety of nucleosynthetic processes, and spread into the Universe through mechanisms including stellar winds and supernova explosions.

The first generation of stars in the Universe were born from pristine natal clouds of hydrogen and helium—these are referred to as "Population III" stars (subsequent

[1] For more on the history of Galactic archaeology, the properties of the main Galactic components, and recent breakthroughs in the field, see the reviews by Beers and Christlieb (2005), Frebel and Norris (2015), and Helmi (2020), which were instrumental in constructing the brief outline included above.

generations of stars are divided into two age tiers: Population II immediately follows Population III, while Population I refers to more recently-born stars like our Sun). These gas clouds could not fragment easily due to the limited cooling mechanisms available in the early Universe, creating massive stars that burned through their available fuel quickly and died explosively, seeding nearby gas clouds with the new elements synthesized in their cores, including carbon, nitrogen, oxygen, and iron. Because these massive stars were so short-lived, we are not able to observe them directly (if there exist any lower-mass, long-lived Pop. III stars, we have not yet discovered them). But the metals ejected by these stars into the Universe, in particular carbon and oxygen, provided new and more-efficient cooling pathways, allowing the gas clouds they polluted to more easily fragment into smaller parts. From these clouds a second generation of lower-mass, more long-lived stars was born. These ancient objects retain the traces of the first stars' chemical fingerprints, and we may still be able to observe some of them today.

From this cycle of stellar processing, the Universe becomes more and more metal-rich over time, with each successive generation of stars being born from a natal gas cloud containing more metals than its predecessors'. This "stellar inheritance" that enriches younger stars with the fruits of their predecessors' labor makes metallicity a useful tracer of stellar age. More precise means of stellar dating, for example, through radioactive elemental abundances, require time-intensive high-resolution spectroscopic measurements, which are not realistic for large data-sets. Instead, astronomers use relative iron abundance as a benchmark for metal enrichment and for age as a whole, as iron lines are one of the most easily measured heavy elements in stellar spectra.

The formalism used to express stellar abundance is $[\mathrm{A/B}] \equiv \log_{10}(N_\mathrm{A}/N_\mathrm{B})_* - \log_{10}(N_\mathrm{A}/N_\mathrm{B})_\odot$, where N_A and N_B are the number densities of atoms of element A and element B, measured for the star in question ($(N_\mathrm{A}/N_\mathrm{B})_*$) compared to the Sun

TABLE 1.1

METALLICITY NOMENCLATURE

[Fe/H]	Term	Acronym
$> +0.5$	super metal-rich	SMR
~ 0.0	solar metallicity	—
< -1.0	metal-poor	MP
< -2.0	very metal-poor	VMP
< -3.0	extremely metal-poor	EMP
< -4.0	ultra metal-poor	UMP
< -5.0	hyper metal-poor	HMP
< -6.0	mega metal-poor	MMP
< -7.0	septa metal-poor	SMP
< -8.0	octa metal-poor	OMP
< -9.0	giga metal-poor	GMP

Table of stellar metallicity nomenclature (and corresponding acronyms), adapted from Beers and Christlieb (2005).

$((N_{\rm A}/N_{\rm B})_\odot)$, our most well-measured star. Stellar metallicity with respect to the Sun is then given as [Fe/H]. We refer to low-metallicity stars as "metal-poor", defined by the criteria [Fe/H] < -1.0. Table 1.1 summarizes the nomenclature used to define the subsequent varying degrees of ever-lower metallicity present in different stars.

The first generation of stars, Pop. III, would be made up of zero-metallicity stars ([Fe/H] $= -\infty$). Pop. I contains younger, more metal-enriched stars like our Sun. Pop. II consists of the aforementioned second generation of stars—these would be created from natal clouds enriched by Pop. III supernovae (SNe), and posses much lower metallicities than Pop. I stars. The ideal method of investigating the nature of Pop. III stars, and thus the nature of the early Universe, would be to measure them directly, but our next best option is to study their descendants, the Pop. II stars.

Metal-poor stars have been widely recognized as "fossils" of the earliest generation of stars in the Universe and as important tracers of the assembly history of our Galaxy—many of the key discoveries in Galactic archaeology outlined at the start of this chapter included analyses of metal-poor stars and the metallicity distribution functions (MDFs) of various stellar populations. In particular, the most metal-poor stars are likely to be among the most ancient, possibly even true second-generation stars (e.g., Beers and Christlieb, 2005; Frebel and Norris, 2015; Hansen et al., 2016a; Hartwig et al., 2018). Discerning the origins of different metal-poor populations in the Milky Way is crucial for understanding when, where, and how different Galactic components formed.

1.2 Carbon-Enhanced Metal-Poor (CEMP) Stars

It has been observed that a significant fraction of metal-poor stars exhibit an enhancement in carbon relative to iron—they contain more carbon than they could have synthesized themselves during their lifetimes, considering their current stage of stellar evolution.[2] The more metal-poor a star is, the more likely it is to be carbon-enhanced (e.g., Lee et al. 2013; Placco et al. 2014; Yoon et al. 2018; see Figure 1.2), leading to the classification of a new category of interest: carbon-enhanced metal-poor (CEMP; [C/Fe]$> +0.7$) stars.

A variety of possible explanations for this carbon-enhancement phenomenon have

[2] A note on evolutionary stages: Placco et al. (2014) developed a useful set of carbon evolutionary corrections to take into account the surface carbon-abundance depletion expected to occur in the upper red giant branch (RGB)—these should be applied to any CEMP data-sets containing giants prior to analyses. I have provided a script in Appendix A.2.1, useful for preparing large data-sets of stars to be processed for correction, which can be used on any system with the Placco et al. (2014) program installed.

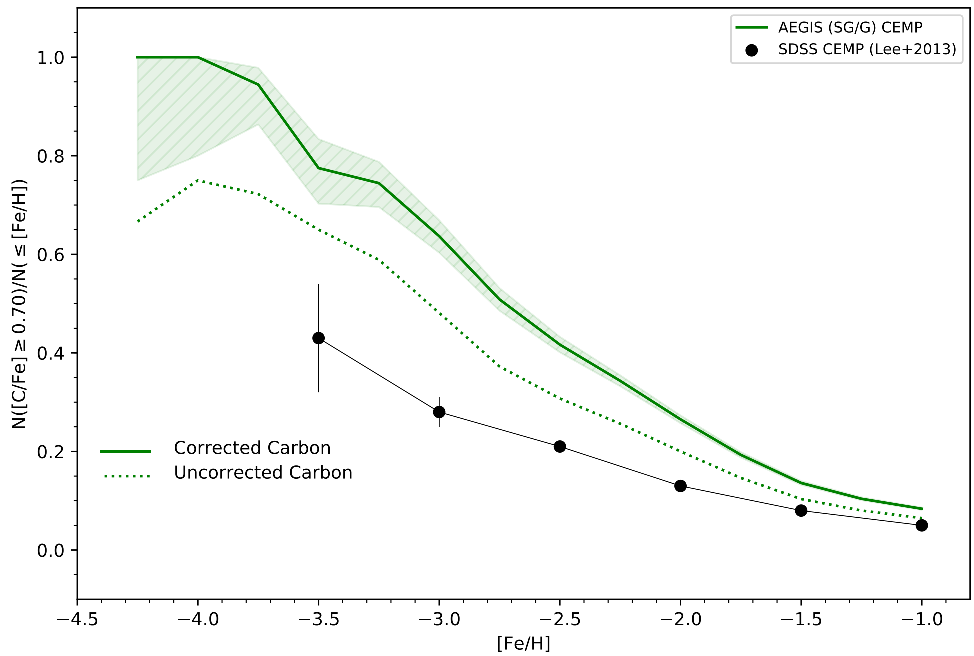

Figure 1.2. Cumulative CEMP fractions over metallicity; figure from Yoon et al. (2018). The black dots represent fractions calculated by Lee et al. (2013). The green lines represent fractions for the AEGIS sample introduced in Yoon et al. (2018) (see Chapter 3 for an introduction to the AEGIS data-set). The solid green line indicates estimates made using the evolutionary carbon corrections developed by Placco et al. (2014). The green shaded area represents the one-sigma Wilson proportion confidence interval for these frequencies (Wilson, 1927). The dashed green line denotes the original, uncorrected estimates.

been posited. For example, a metal-poor star with a binary companion on the asymptotic giant branch (AGB) stage of evolution could acquire some of its partner's surface carbon via binary mass transfer—this is indeed the case with some CEMP stars, as noted in the section below. The more interesting (from a Galactic archaeology standpoint) explanation is that some of these stars inherited their excess carbon from a previous generation of stars. As many CEMP stars are potential Pop. II candidates, this chemical signature could be directly linked to the properties of the first stars.

This first-star link is undergoing continuous investigation. The enhanced [C/Fe] ratio could, as some studies suggest, be produced by faint SNe of Pop. III stars—these (relatively) lower-energy explosions would preferentially eject lighter elements like carbon into the interstellar medium over heavier elements like iron. Other explanations include stellar winds from massive spin-stars or inhomogeneous cooling of natal gas clouds. Our search for the origin of CEMP stars is made no less complicated by the fact that multiple progenitors are likely responsible for the CEMP signature. This possibility is supported by the presence of several sub-classes of CEMP stars, outlined below.

1.2.1 CEMP Sub-Classes: Neutron-Capture Signatures

CEMP stars can be further separated into several sub-groups, based on their enhancements, or lack of enhancements, of elements associated with neutron-capture processes (see Table 1.2). CEMP-s and CEMP-r stars exhibit over-abundances of elements associated with the slow neutron-capture process (s-process) and rapid neutron-capture process (r-process), respectively. CEMP-r/s stars exhibit over-abundances associated with both the s-process and the r-process,[3] while CEMP-no stars exhibit no strong over-abundances of elements associated with neutron-capture processes.

Lucatello et al. (2005), and later Hansen et al. (2016b), showed that a significant fraction of CEMP-s stars occur in binary pairs—most CEMP-s stars likely acquire their excess carbon and their s-process enhancements from a more evolved AGB binary companion. The AGB star is able to synthesize its s-process elements and carbon, which reach surface through dredge-up events and may then be donated to

[3]Some studies suggest the CEMP-r/s elemental abundance pattern is a product of the intermediate neutron-capture process (i-process), and so the CEMP-r/s category should be renamed as "CEMP-i" (Hampel et al., 2016).

TABLE 1.2

CEMP CRITERIA

Class	Criteria
CEMP-s	[Ba/Fe]$>+1.0$, [Ba/Eu]$>+0.5$
CEMP-r	[Eu/Fe]$>+1.0$
CEMP-r/s	$0.0<$[Ba/Eu]$<+0.5$
CEMP-no	[Ba/Fe]<0.0

Required criteria for CEMP sub-classes (*in addition* to the [Fe/H]<-1.0, [C/Fe]>0.7 criteria required for all CEMP stars). Table adapted from Beers and Christlieb (2005).

its companion (Ostlie and Carroll, 1996; Ryan and Norton, 2010). But this mass-transfer scenario does not fit all categories of CEMP stars—Hansen et al. (2015) and Hansen et al. (2016a) found that CEMP-r and CEMP-no stars do *not* preferentially occur in binaries. For these sub-classes it remains a viable explanation that the excess carbon they display was contained in their natal clouds prior to their formation—the chemical fingerprint of the first stars.

1.2.2 CEMP Sub-Classes: Groups I, II, III

We can understand more about the origins of these CEMP sub-classes through the CEMP group morphology presented in Yoon et al. (2016). Traditionally, high-resolution spectroscopy is used to provide accurate estimates for the barium and europium abundances needed to sort CEMP stars into the sub-classes outlined above. Yoon et al. (2016) found that CEMP-no and CEMP-s membership can be determined using only absolute carbon abundance, A(C), defined by $A(\mathrm{C}) = \log\epsilon(\mathrm{C}) = \log(N_{\mathrm{C}}/N_{\mathrm{H}}) + 12$, where N indicates the number density of each species. They showed that CEMP-no stars are mainly found at A(C)$\leq$ 7.1 while CEMP-s and CEMP-r/s stars are mainly found at A(C)> 7.1.[4] They categorized the CEMP-s and CEMP-r/s stars as "Group I". CEMP-no stars appear to populate at least two separate regions in A(C)-[Fe/H] space, leading the authors to propose two separate classifications, Group II and Group III, for the CEMP-no sub-class, as seen in Figure 1.3.

The physical explanation behind the separation between Groups II and III is not yet fully understood, though a variety of possible scenarios have been suggested. For example, Chiaki et al. (2017) posit that this separation may represent a transition from dust cooling dominated by carbon grains (Group III) to dust cooling dominated by silicate grains (Group II). The more efficient silicate grain cooling would create more low-mass, long-lived stars (hence the well-populated Group II region), while the less efficient carbon grain cooling would create fewer stars, but with higher carbon abundances. Yoon et al. (2019) investigated the link between CEMP-no stars in the Galactic halo and those observed in external dwarf galaxies (widely acknowledged as candidate "building blocks" of the outer-halo), finding Group III to be preferentially associated with ancient, ultra-faint dwarf (UFD) galaxies, while Group II was found in both UFDs and the (relatively) more massive and chemically evolved dwarf spheroidal (dSph) category. Just as the origin of CEMP stars as a whole is still being explored, our understanding of this Group II/Group III dichotomy is continuously evolving and may undergo significant revision in the coming years.

The various sub-classes of CEMP stars detailed above serve as useful tracers of different Galactic populations. As theorists work to better understand the progenitors responsible for these different chemical signatures, observational astronomers use these differences to make inferences about Galactic components based on their CEMP sub-class ratios. Studies of this nature can be used to draw connections or distinctions

[4] Note that this division can vary for different luminosity classes.

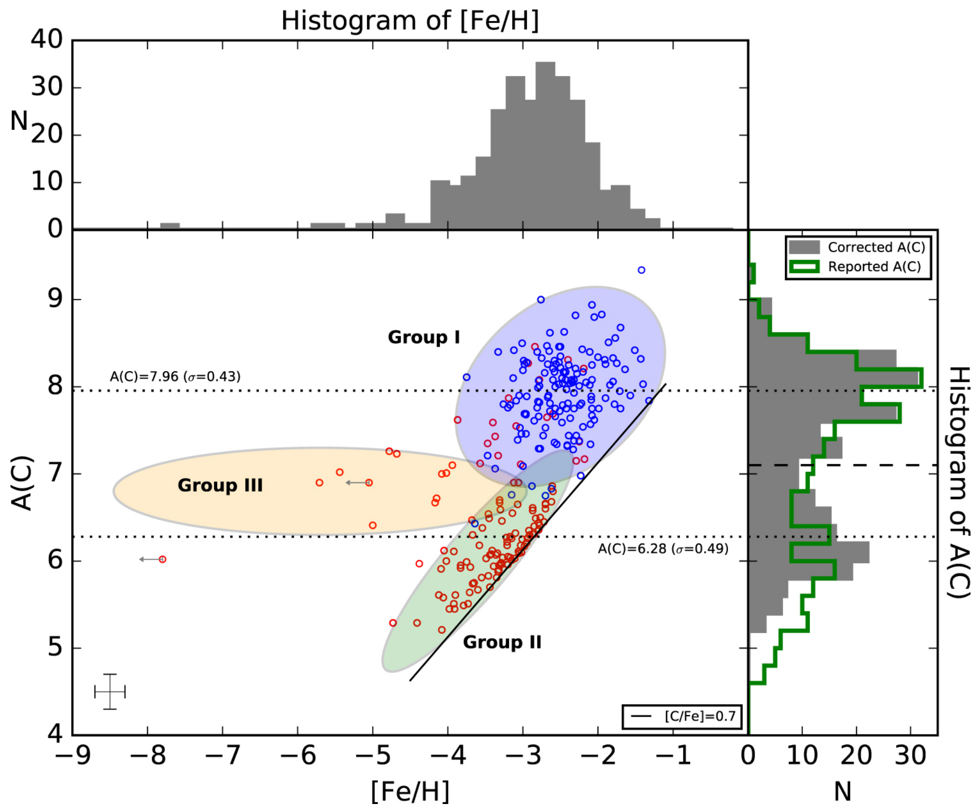

Figure 1.3. Scatter diagram of $A(\mathrm{C})$ vs. [Fe/H] from Yoon et al. (2016) (caption adapted from original text). Blue and red open circles represent CEMP-s/rs stars and CEMP-no stars, respectively. Black dotted lines indicate the locations of the carbon peaks, based on a two-component Gaussian fit to the $A(\mathrm{C})$ distribution. The black solid line provides a reference at $[\mathrm{C/Fe}] = +0.7$. The shaded histogram in the top margin shows the metallicity distribution of the full sample. The shaded histogram in the right margin is the corrected $A(\mathrm{C})$ distribution (includes the Placco et al. 2014 corrections); the green unfilled histogram is the "as reported" $A(\mathrm{C})$ distribution. The black dashed line in the $A(\mathrm{C})$ histogram represents the midpoint of the $A(\mathrm{C})$ peaks, used for separation of CEMP-s/rs stars from CEMP-no stars. A typical error bar for the sample considered is shown at the bottom left.

between Galactic components, identify evidence of past mergers, constrain Galactic formation scenarios, and more.

1.3 This Work, in Brief

In this work I use metal-poor stars and CEMP stars, in tandem with high-precision *Gaia* astrometry, to explore chemical and kinematic patterns within the disk and halo systems of our Galaxy, in order to constrain the formation histories of these components.

Chapter 2 provides an overview of stellar kinematics, which is key in identifying tracer populations, and descriptions of the kinematic methods and programs used in subsequent analyses. Chapter 3 presents a set of CEMP populations within the thick-disk system, focusing on these stars' implications for the evolution of the disk region and whether they support the case for the MWTD as a component distinct from the canonical thick-disk. Chapter 4 tackles the dual-halo, following two approaches for separating the inner- and outer-halo, as well as changes to our understanding of the halo's history following *Gaia* DR2. Chapter 5 continues the study of the halo to its observational outskirts, presenting evidence for an asymmetrical metallicity gradient in the outer-halo and its potential implications for the formation history of the outermost parts of our Galaxy. Finally, Chapter 6 provides an abridged summary of all major results, including a brief discussion on the current and future state of Galactic archaeology.

CHAPTER 2

KINEMATICS

Figure 2.1 provides the reader with a simple yet effective picture regarding the role of stellar kinematics within Galactic archaeology. The metal-poor and CEMP stellar "fossils" introduced in the previous chapter can be used as tracer populations to track the Milky Way's formation history, if we are able to accurately discern which larger Galactic populations (i.e., which Galactic components) they belong to. This chapter provides an introduction to basic kinematic concepts, parameters, and derivations used throughout this work. Section 2.1 outlines the necessary observed quantities required to derive a star's position and full-space motion. Section 2.2 presents several useful transformations and derivations. Section 2.3 introduces the primary Galactic potential used in this work.

I have included any stellar kinematic codes mentioned here in Appendix A.2 and made them publicly available via GitHub (astrodietz/stellar_kinematics).

2.1 Observed Quantities

2.1.1 Position

A star's observed position in the "equatorial system" is given by its location on the celestial sphere, as shown in Figure 2.2. "Right ascension" (α, range: $0°$ to $360°$) gives its displacement along the celestial equator from the vernal equinox (Υ in Figure 2.2), while "declination" (δ, range: $-90°$ to $+90°$) indicates its displacement

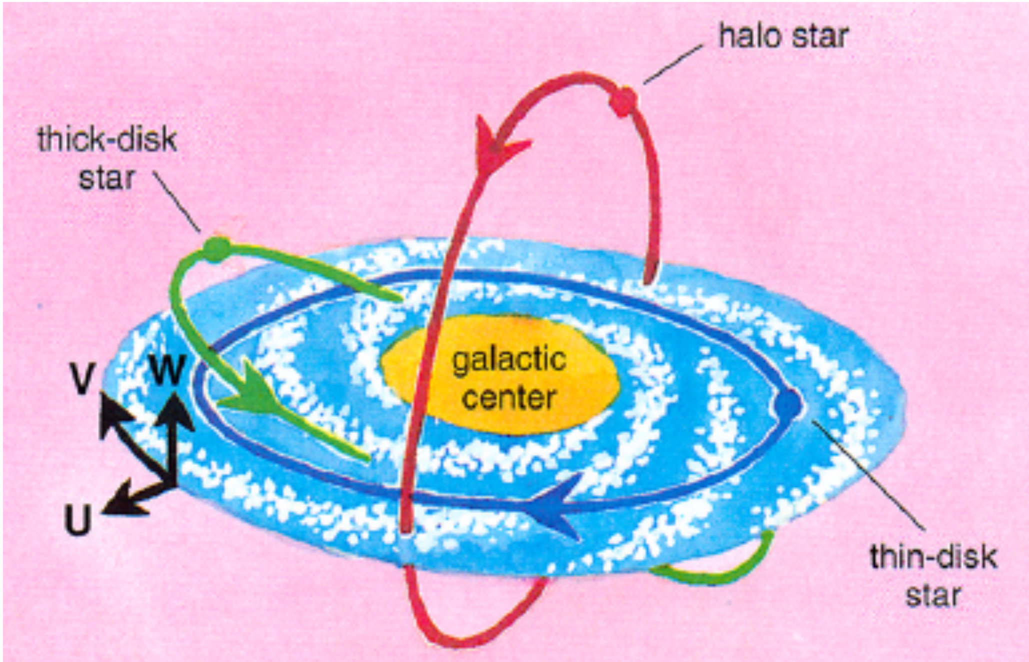

Figure 2.1. Diagram of Milky Way stellar kinematics from Chiappini (2001). Includes example orbits characteristic of thin-disk, thick-disk, and halo stars. Directions of velocity components U, V, and W within the Galactic reference frame (see Section 2.2) are shown in the lower left-hand corner.

along the hour circle drawn from the celestial equator through the celestial poles. Position-related coordinate transformations are included in Section 2.2.

2.1.2 Velocity

The three orthogonal velocity components astronomers measure in order to acquire the full-space motion for a star are radial velocity (v_r) and proper motion (in two directions: α and δ). Radial velocity is a measure of a star's motion along the observer's line of sight, and can be calculated via the Doppler shift in a star's spectrum. By measuring the shift, $\Delta\lambda$, between the rest-frame wavelength (λ_0) and observed wavelength of a spectral feature, an estimate for the radial velocity can be made using the relation $v_r = c\Delta\lambda/\lambda_0$, where $c = 3 \times 10^5\,\mathrm{km\,s^{-1}}$ is the speed of light.

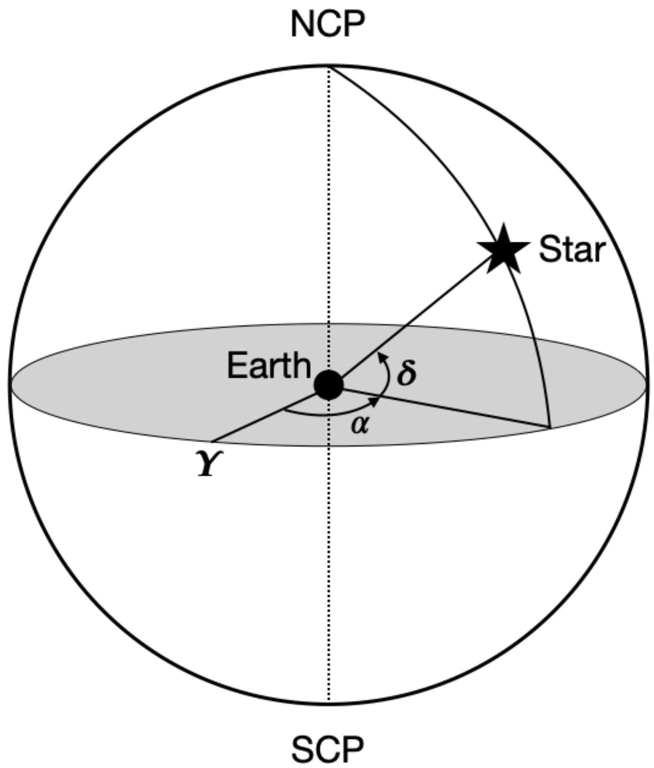

Figure 2.2. The celestial sphere and the equatorial coordinate system. ♈ marks the vernal equinox, used as the zero-point for right ascension. The celestial equator, encircling the shaded area, marks the zero-point for declination. The south celestial pole (SCP) has a declination of $-90°$, and the north celestial pole (NCP) has a declination of $+90°$.

Proper motion (μ) describes a star's motion across the celestial sphere in the direction of α (μ_α) or δ (μ_δ), often given in milli-arcseconds per year ($\mathrm{mas\,yr^{-1}}$), and must be obtained over the course of multiple observations.

Velocity-related coordinate transformations are included in Section 2.2.

2.1.3 Distance

The final observed quantity required for stellar kinematic analyses is distance, d. The distances used in this work are derived either astrometrically or photometrically.

Astrometric distances are derived using parallaxes, such as those provided by the *Gaia* survey (Gaia Collaboration et al., 2016). A parallax describes the change in apparent position of a star when observed at two different vantage points (at two different points in the Earth's orbit, see Figure 2.3). The trigonometric relation between this angle (p) and the distance is:

$$\tan p = 1\,\mathrm{A.U.}/\mathrm{d}, \tag{2.1}$$

where 1 A.U. is one astronomical unit, the average Earth-Sun distance. As $d \gg 1\,\mathrm{A.U.}$ for all our observations, we can further simplify this equation using the small-angle approximation.

$$\begin{aligned} d &= 1\,\mathrm{A.U.}/\tan\mathrm{p} \\ &\simeq 1\,\mathrm{A.U.}/\sin\mathrm{p} \\ &\simeq 1\,\mathrm{A.U.}/\mathrm{p} \end{aligned} \tag{2.2}$$

Note that, in the lines above above, p must be given in radians. A new unit of distance is introduced for convenience: the parsec ($\sim 3 \times 10^{13}\,\mathrm{km}$), defined as the stellar distance at which the measurements made at t_1 and t_2 (see Figure 2.3) will produce a parallax of one arcsecond. Using units of parsecs and arcseconds for d and p, Equation 2.2 can be expressed as $d = 1/p$.

It is worth noting here that the *Gaia* astrometric survey, used throughout this work, has a systematic parallax bias, which should be considered prior to any analyses. For consistency, I use the Bailer-Jones et al. (2018) treatment of the *Gaia* parallaxes throughout this work. This method adopts a prior with a smoothly-varying Galactic

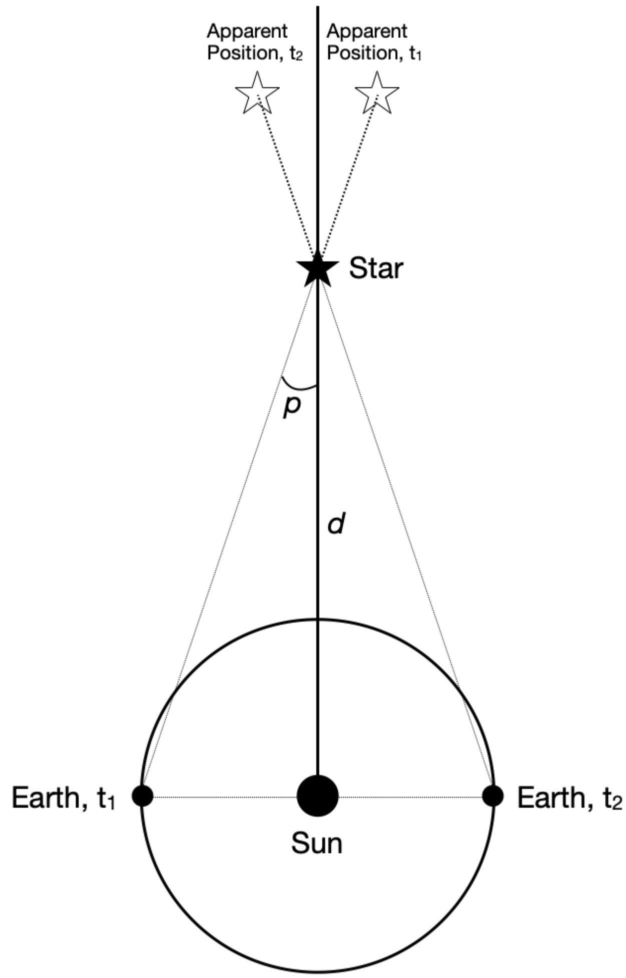

Figure 2.3. A diagram illustrating the parallax-distance relation. The positions within the Earth's orbital path marked with t_1 and t_2 indicate two separate observations of the same star, taken half a year apart (separated by 2 A.U.). The observed position of the star on the celestial sphere shifts by a total angle $2p$ between observations. The distance between the Sun and the observed star is marked d.

length scale parameter to infer *Gaia* distances in a probabilistic manner.

When a parallax measurement is not available, a star's distance can be estimated photometrically. For a star of absolute (intrinsic) magnitude M and apparent (observed) magnitude m, the distance d in parsecs to the star is given by:

$$m - M = 5\log(d) - 5, \tag{2.3}$$

where the term $m - M$ is called the distance modulus. This work employs the process outlined in Beers et al. (2000) for photometric distance estimates. The authors use well-measured fiducial sequences (e.g., globular clusters) to create polynomial fits in magnitude-color space for stars of different luminosity classes and metallicities. Stars are then matched to the appropriate fit to estimate absolute magnitude, and thus the distance modulus.

2.2 Transformations

Using the parameters outlined above, a star's position and velocity can be transformed, for convenience, to different reference frames and coordinate systems.

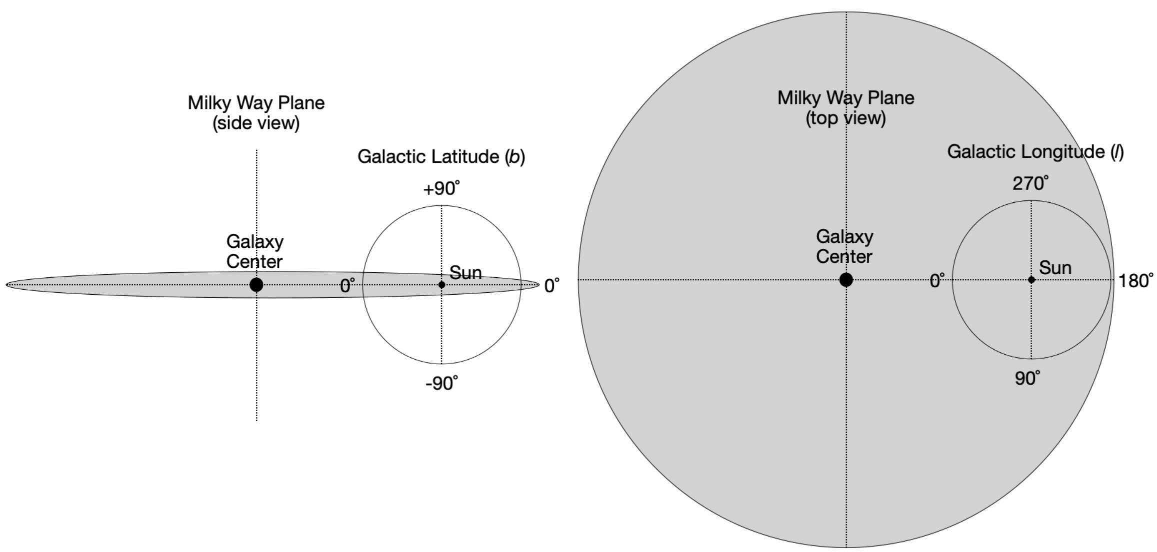

Figure 2.4. Left: the Galactic coordinate system, side view. Right: the Galactic coordinate system, top view.

The Galactic reference frame gives a star's position with respect to an equator aligned to the plane of the Milky Way. Coordinates are given in Galactic longitude (l, range: $0°$ to $360°$) and latitude (b, range: $-90°$ to $+90°$), as indicated in Figure 2.4. The transformation between the two frames can be given most simply using rotation matrices. We want to form a transformation matrix $\mathbf{T}$, satisfying:

$$\begin{bmatrix} x_{\text{gal}} \\ y_{\text{gal}} \\ z_{\text{gal}} \end{bmatrix} = \mathbf{T} \begin{bmatrix} x_{\text{equ}} \\ y_{\text{equ}} \\ z_{\text{equ}} \end{bmatrix} . \tag{2.4}$$

Some basic trigonometry can be applied to show:

$$\begin{bmatrix} x_{\text{equ}} \\ y_{\text{equ}} \\ z_{\text{equ}} \end{bmatrix} = d \begin{bmatrix} \cos\delta\cos\alpha \\ \cos\delta\sin\alpha \\ \sin\delta \end{bmatrix} , \tag{2.5}$$

$$\begin{bmatrix} x_{\text{gal}} \\ y_{\text{gal}} \\ z_{\text{gal}} \end{bmatrix} = d \begin{bmatrix} \cos b\cos l \\ \cos b\sin l \\ \sin b \end{bmatrix} , \tag{2.6}$$

which allows us to rewrite Equation 2.4 as:

$$\begin{bmatrix} \cos b\cos l \\ \cos b\sin l \\ \sin b \end{bmatrix} = \mathbf{T} \begin{bmatrix} \cos\delta\cos\alpha \\ \cos\delta\sin\alpha \\ \sin\delta \end{bmatrix} . \tag{2.7}$$

For the following derivations, it is useful to define the angles α_{NGP}, δ_{NGP}, and θ_0; α_{NGP} and δ_{NGP} are the equatorial coordinates for the North Galactic Pole (NGP; $192.25°$, $27.4°$) and θ_0 is the position of the North Celestial Pole with respect to the circle passing through the NGP and the line marking $l = 0°$.

The equatorial-Galactic coordinate transformation can be expressed through three successive rotations: a rotation about the z-axis (to shift the x-axis from its vernal equinox zero-point to α_{NGP}), a rotation about the y-axis (to align the z-axis with the NGP), and a final rotation about the z-axis (to align the x-axis with the zero-point of galactic longitude).

The general forms for (counter-clockwise) rotations about the y- and z-axes are given by Equations 2.8 and 2.9, respectively.

$$\mathbf{R}_y(\theta_y) = \begin{bmatrix} \cos\theta_y & 0 & -\sin\theta_y \\ 0 & 1 & 0 \\ \sin\theta_y & 0 & \cos\theta_y \end{bmatrix} \tag{2.8}$$

$$\mathbf{R}_z(\theta_z) = \begin{bmatrix} \cos\theta_z & \sin\theta_z & 0 \\ -\sin\theta_z & \cos\theta_z & 0 \\ 0 & 0 & 1 \end{bmatrix} \tag{2.9}$$

$\mathbf{T}$ can then be expressed as $\mathbf{R}_3(\theta_3)\mathbf{R}_2(\theta_2)\mathbf{R}_1(\theta_1)$. For the rotations described above, $\theta_1 = \alpha_{\mathrm{NGP}}$, $\theta_2 = \pi/2 - \delta_{\mathrm{NGP}}$, and $\theta_3 = \pi - \theta_0$.

$$\mathbf{R}_1 = \begin{bmatrix} \cos\alpha_{\mathrm{NGP}} & \sin\alpha_{\mathrm{NGP}} & 0 \\ -\sin\alpha_{\mathrm{NGP}} & \cos\alpha_{\mathrm{NGP}} & 0 \\ 0 & 0 & 1 \end{bmatrix} \tag{2.10}$$

$$\mathbf{R}_2 = \begin{bmatrix} \cos(\pi/2 - \delta_{\mathrm{NGP}}) & 0 & -\sin(\pi/2 - \delta_{\mathrm{NGP}}) \\ 0 & 1 & 0 \\ \sin(\pi/2 - \delta_{\mathrm{NGP}}) & 0 & \cos(\pi/2 - \delta_{\mathrm{NGP}}) \end{bmatrix} \tag{2.11}$$

$$\mathbf{R}_3 = \begin{bmatrix} \cos(\pi - \theta_0) & \sin(\pi - \theta_0) & 0 \\ -\sin(\pi - \theta_0) & \cos(\pi - \theta_0) & 0 \\ 0 & 0 & 1 \end{bmatrix} \tag{2.12}$$

Combining the above,

$$\mathbf{T} = \begin{bmatrix} -\cos\theta_0 \sin\delta_{\rm NGP}\cos\alpha_{\rm NGP} - \sin\theta_0 \sin\alpha_{\rm NGP} & -\cos\theta_0 \sin\delta_{\rm NGP}\sin\alpha_{\rm NGP} + \sin\theta_0\cos\alpha_{\rm NGP} & \cos\theta_0\cos\delta_{\rm NGP} \\ -\sin\theta_0 \sin\delta_{\rm NGP}\cos\alpha_{\rm NGP} + \cos\theta_0 \sin\alpha_{\rm NGP} & -\sin\theta_0\sin\delta_{\rm NGP}\sin\alpha_{\rm NGP} - \cos\theta_0\cos\alpha_{\rm NGP} & \sin\theta_0\cos\delta_{\rm NGP} \\ \cos\delta_{\rm NGP}\cos\alpha_{\rm NGP} & \cos\delta_{\rm NGP}\sin\alpha_{\rm NGP} & \sin\delta_{\rm NGP} \end{bmatrix}. \tag{2.13}$$

From this, the Galactic coordinates l and b can be solved directly using:

$$\cos b \cos l = T_{00}(\cos\delta\cos\alpha) + T_{01}(\cos\delta\sin\alpha) + T_{02}(\sin\delta), \tag{2.14}$$

$$\cos b \sin l = T_{10}(\cos\delta\cos\alpha) + T_{11}(\cos\delta\sin\alpha) + T_{12}(\sin\delta), \tag{2.15}$$

$$\sin b = T_{20}(\cos\delta\cos\alpha) + T_{21}(\cos\delta\sin\alpha) + T_{22}(\sin\delta). \tag{2.16}$$

Using an additional matrix, $\mathbf{A}$, we can transform the observed velocity quantities v_r, μ_α, and μ_δ from the equatorial coordinate system to the Galactic coordinate system (with velocity components U, V, W). The observed full-space velocity vector $(v_r, v_\alpha, v_\delta)$ can be rewritten as $(v_r, \mu_\alpha d, \mu_\delta d)$. To convert from kpc mas yr^{-1} to km s^{-1}, we calculate a conversion factor, k.

$$\begin{aligned} k &= \frac{10^3\,\mathrm{pc}}{1\,\mathrm{kpc}}\frac{1\,\mathrm{as}}{10^3\,\mathrm{mas}}\frac{1\,\mathrm{A.U.}}{1\,\mathrm{pc\,as}}\frac{1.496\times10^8\,\mathrm{km}}{1\,\mathrm{A.U.}}\frac{1\,\mathrm{yr}}{365\,\mathrm{days}}\frac{1\,\mathrm{day}}{24\,\mathrm{hr}}\frac{1\,\mathrm{hr}}{3600\,\mathrm{sec}} \\ &= 4.74\,\mathrm{km\,yr\,kpc^{-1}\,mas^{-1}\,s^{-1}} \end{aligned} \tag{2.17}$$

The velocity vector can now be written as $(v_r, \mu_\alpha kd, \mu_\delta kd)$.

To find the Cartesian velocity components within the equatorial coordinate system, we perform two rotations to align the observed velocity vectors with the x-, y-, and z-axes: one counterclockwise rotation by δ about the y-axis followed by one counterclockwise rotation of $2\pi - \alpha$ about the z-axis. Using the general rotation matrices listed above (Equations 2.8 and 2.9), we can express the transformation matrix $\mathbf{A}$ as:

$$\begin{aligned}
\mathbf{A} &= \begin{bmatrix} \cos(2\pi-\alpha) & \sin(2\pi-\alpha) & 0 \\ -\sin(2\pi-\alpha) & \cos(2\pi-\alpha) & 0 \\ 0 & 0 & 1 \end{bmatrix} \begin{bmatrix} \cos\delta & 0 & -\sin\delta \\ 0 & 1 & 0 \\ \sin\delta & 0 & \cos\delta \end{bmatrix} \\
&= \begin{bmatrix} \cos\alpha & -\sin\alpha & 0 \\ \sin\alpha & \cos\alpha & 0 \\ 0 & 0 & 1 \end{bmatrix} \begin{bmatrix} \cos\delta & 0 & -\sin\delta \\ 0 & 1 & 0 \\ \sin\delta & 0 & \cos\delta \end{bmatrix} \\
&= \begin{bmatrix} \cos\alpha\cos\delta & -\sin\alpha & -\cos\alpha\sin\delta \\ \sin\alpha\cos\delta & \cos\alpha & -\sin\alpha\sin\delta \\ \sin\delta & 0 & \cos\delta \end{bmatrix} .
\end{aligned} \tag{2.18}$$

Cartesian equatorial velocities can then be obtained with

$$\begin{bmatrix} v_{x,\mathrm{equ}} \\ v_{y,\mathrm{equ}} \\ v_{z,\mathrm{equ}} \end{bmatrix} = \mathbf{A} \begin{bmatrix} v_r \\ \mu_\alpha k d \\ \mu_\delta k d \end{bmatrix} , \tag{2.19}$$

where the corresponding Galactic velocities are

$$\begin{bmatrix} U \\ V \\ W \end{bmatrix} = \mathbf{T} \cdot \mathbf{A} \begin{bmatrix} v_r \\ \mu_\alpha k d \\ \mu_\delta k d \end{bmatrix} . \tag{2.20}$$

The Galactic velocity vectors should be appropriately modified to take into account the Sun's motion ($v_\odot$) with respect to the local standard of rest (LSR); in the majority of this work I use $v_\odot = (-9, 12, 7)\,\mathrm{km\,s^{-1}}$ (Mihalas, 1981).

$$\begin{bmatrix} U_{\mathrm{LSR}} \\ V_{\mathrm{LSR}} \\ W_{\mathrm{LSR}} \end{bmatrix} = \begin{bmatrix} U - 9\,\mathrm{km\,s^{-1}} \\ V + 12\,\mathrm{km\,s^{-1}} \\ W + 7\,\mathrm{km\,s^{-1}} \end{bmatrix} \tag{2.21}$$

To express a star's position and velocity with respect to a Galactocentric coordinate system, we need to consider the Sun's position with respect to the Galactic center and the motion of the LSR with respect to the Galactic center. Although all coordinate systems used in this chapter so far have been right-handed, by convention the Galactocentric coordinate frame is left-handed, with the $+x$-axis pointing in the direction of the Galaxy's anti-center. Practically, all that is needed is to invert the sign of the x-components of the position and velocity vectors. Using $R_\odot = 8\,\mathrm{kpc}$ as the Sun's distance from the Galactic center and $v_{\mathrm{LSR}} = 220\,\mathrm{km\,s^{-1}}$ (Kerr and Lynden-Bell, 1986) as the local rotation of the disk about the Galaxy's center, we can write:

$$\begin{bmatrix} x_{\mathrm{gc}} \\ y_{\mathrm{gc}} \\ z_{\mathrm{gc}} \end{bmatrix} = \begin{bmatrix} -x_{\mathrm{gal}} \\ y_{\mathrm{gal}} + 8\,\mathrm{kpc} \\ z_{\mathrm{gal}} \end{bmatrix}, \tag{2.22}$$

$$\begin{bmatrix} v_{x,\mathrm{gc}} \\ v_{y,\mathrm{gc}} \\ v_{z,\mathrm{gc}} \end{bmatrix} = \begin{bmatrix} -U_{\mathrm{LSR}} \\ V_{\mathrm{LSR}} + 220\,\mathrm{km\,s^{-1}} \\ W_{\mathrm{LSR}} \end{bmatrix}. \tag{2.23}$$

It can be most useful to express a star's Galactocentric velocity vector in cylindrical coordinates as well. Starting with position coordinates $R = \sqrt{x_{\mathrm{gc}}^2 + y_{\mathrm{gc}}^2}$ and $\phi = \arctan(y_{\mathrm{gc}}/x_{\mathrm{gc}})$, we can write:

$$v_r = \dot{R} = \frac{x_{\mathrm{gc}} v_{x,\mathrm{gc}} + y_{\mathrm{gc}} v_{y,\mathrm{gc}}}{\sqrt{x_{\mathrm{gc}}^2 + y_{\mathrm{gc}}^2}}, \tag{2.24}$$

$$v_\phi = R\dot{\phi} = \frac{x_{\rm gc} v_{y,\rm gc} - y_{\rm gc} v_{x,\rm gc}}{\sqrt{x_{\rm gc}^2 + y_{\rm gc}^2}}. \tag{2.25}$$

The z-component of the Galactocentric cylindrical velocity is equal to the z-component of the Galactocentric Cartesian velocity. Here I make note of some terminology that will be used frequently in the following chapters: "prograde" motion refers to $v_\phi > 0$ rotation about the Galactic center, and "retrograde" motion refers to $v_\phi < 0$ rotation about the Galactic center.

These transformations need not be calculated by hand, as they can easily be computed in Python through the `galpy` galactic dynamics package (Bovy, 2015). Appendix A.2.2.1 contains a "kinematic pipeline" program that reads in the observed quantities listed in Section 2.1 and calls the necessary `galpy` functions to compute the various positions and velocities derived above, in addition to providing orbital parameters using the Galactic potential introduced below. This pipeline can process values for large numbers of stars inputted in a CSV file format; I provide a shorter example code stepping through the derivations shown above and their associated `galpy` functions on GitHub.

2.3 The Galactic Potential

In order to extrapolate additional information about a star's motion relating to its orbital path, a model for the Galaxy's potential must be adopted. In this work I implement a version of the Fortran Galactic potential code used in Chiba and Beers (2000), which I have updated to run in Python (see Appendix A.2.2.2). This code adopts the analytic Stäckel potential developed by Sommer-Larsen and Zhen (1990), consisting of a flattened, oblate disk and a nearly spherical massive halo. I use this potential in part to more easily compare my results to previous literature findings using the same potential.

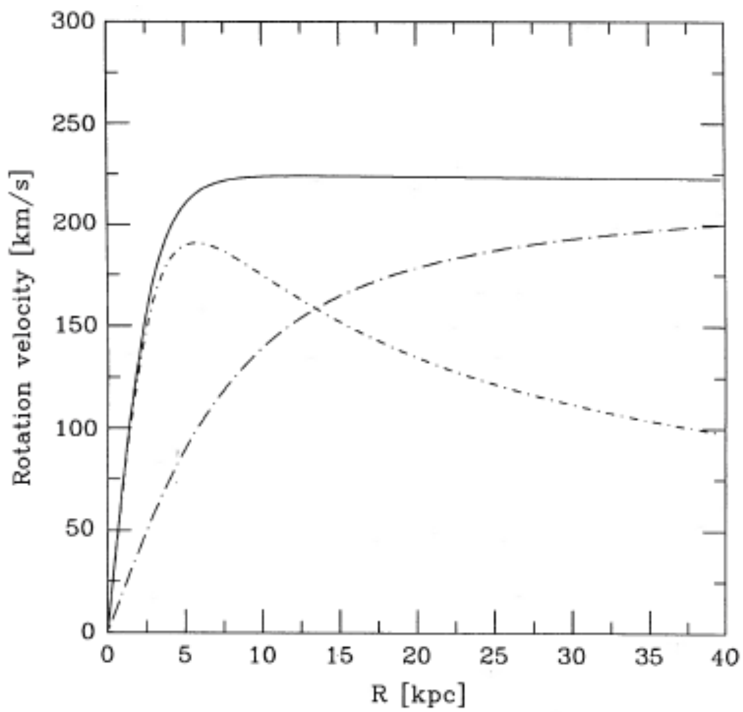

Figure 2.5. Rotation curve for the chosen Galactic model, image from Sommer-Larsen and Zhen (1990). The short-dashed line indicates contributions from the disk component, the long-dashed line indicates contributions from the halo component, and the solid line gives their sum.

Sommer-Larsen and Zhen (1990) define a spheroidal coordinate system with components (λ, ϕ, ν), where ϕ is the same angle used in a cylindrical coordinate system (R, ϕ, z). Coordinates λ and ν are the roots of τ in the equation below.

$$\frac{R^2}{\tau+\alpha} + \frac{z^2}{\tau+\gamma} = 1 \tag{2.26}$$

The potential, Ψ, takes the general form:

$$\Psi = -\frac{(\lambda+\gamma)G(\lambda) - (\nu+\gamma)G(\nu)}{\lambda-\nu}. \tag{2.27}$$

The gravitational term $G(\tau)$ is split into a disk component, G_{D}, and a massive halo component, G_{MH}. The disk is modeled as a perfect oblate spheroid with mass

$M_{\rm D} = 9.0 \times 10^{10}\, M_{\odot}$. The halo is an oblate model characterized by a density profile $\rho(0, z) \propto 1/(z^2 + c^2)$, where c is a constant. See Sommer-Larsen and Zhen (1990) for further details.

The Hamiltonian per unit mass can be expressed in terms of Ψ and the momenta $(p_\lambda,\, p_\Phi,\, p_\nu)$ as:

$$H' = \frac{p_\lambda^2}{2P^2} + \frac{p_\Phi^2}{2R^2} + \frac{p_\nu^2}{2Q^2} + \Psi(\lambda, \nu), \tag{2.28}$$

where P, R, and Q are the metric coefficients of the chosen coordinate system. The coefficients P and Q are given below (R is the simply the radial cylindrical coordinate); see Appendix A.1.1 for a full derivation.

$$P^2 = \frac{\lambda - \nu}{4(\lambda + \alpha)(\lambda + \gamma)} \tag{2.29}$$

$$Q^2 = -\frac{\lambda - \nu}{4(\nu + \alpha)(\nu + \gamma)} \tag{2.30}$$

The integrals of motion (useful orbital constants) for this potential are energy (E), I_2, and I_3, where $I_2 = \frac{1}{2}L_z^2$ and I_3 is given by de Zeeuw and Lynden-Bell (1985) as

$$I_3 = \frac{1}{2}(L_x^2 - L_y^2) + \Delta^2 E_z, \tag{2.31}$$

where Δ is a constant (see Appendix A.1.2 for more details).

The potential program given in Appendix A.2.2.2 has two main functionalities: 1) it calculates the integrals of motion E, I_2, and I_3 and 2) it simulates a star's orbital path, looking for "turning points" in the orbit where $p_\lambda = 0$ or $p_\nu = 0$. The latter process allows it to determine if a star should be considered as bound or unbound to the Galaxy, and solving for the turning-point coordinates allows useful parameters including apocentric radius ($r_{\rm apo}$), pericentric radius ($r_{\rm peri}$), and orbital eccentricity (e) to be calculated.

Uncertainties on these orbital parameters are calculated with a Monte Carlo approach. Assuming that the uncertainty ranges given for input parameters are normally distributed about their observed values, 1,000 new orbits are randomly generated from these distributions. I adopt the standard deviations of the resulting orbital parameter distributions as my orbital uncertainties (see Figure 2.6).

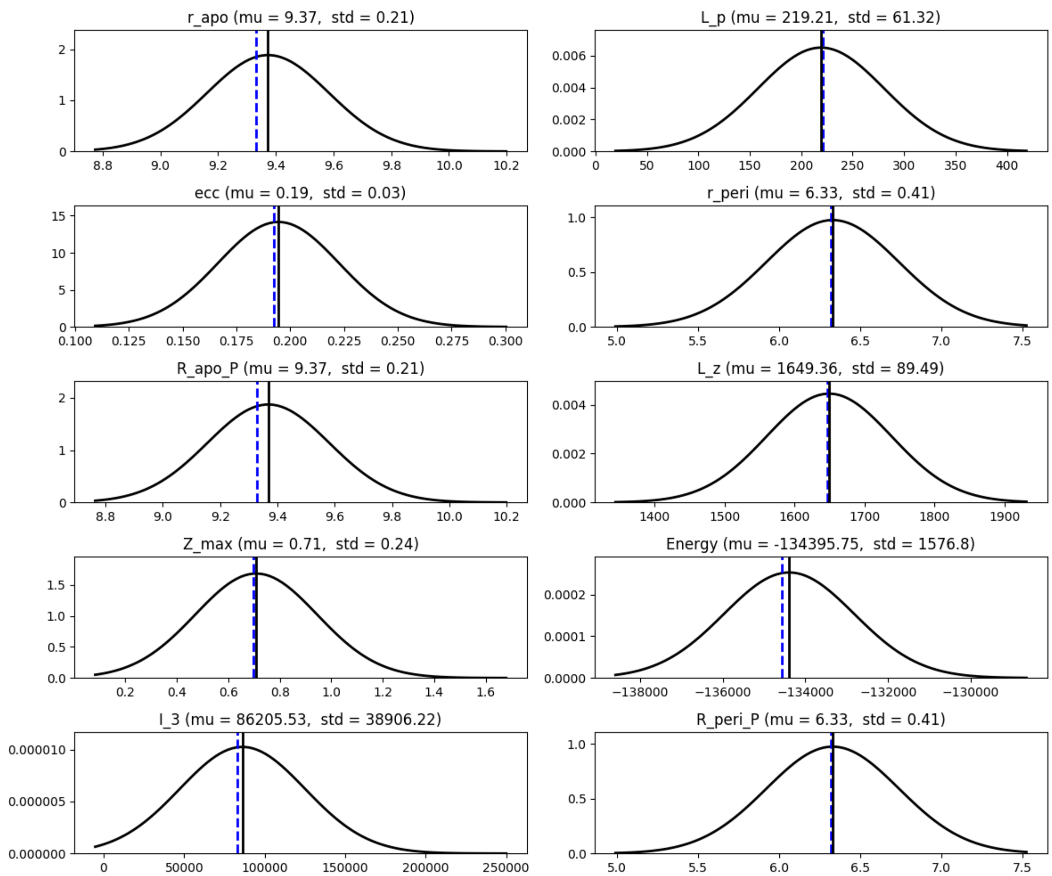

Figure 2.6. A set of orbital uncertainty fits, automatically generated by the kinematic pipeline. Each sub-plot shows data for a different orbital parameter. The black curves are Gaussian fits of the underlying data. The black lines and blue-dashed lines indicate the mean of the fit and the calculated value of the parameter, respectively.

Estimations on orbital uncertainties are useful for kinematic analyses, but this random orbit generation process can be computationally expensive for large data-sets. In these cases, the University of Notre Dame's HTCondor pool, which distributes computational tasks to idle workstations across the campus network, has proven exceptionally useful. Appendix A.2.3 includes an example of the set of scripts I use to break up large kinematics runs into many small HTCondor jobs, and then re-assemble the resulting output.

CHAPTER 3

THE DISK SYSTEM

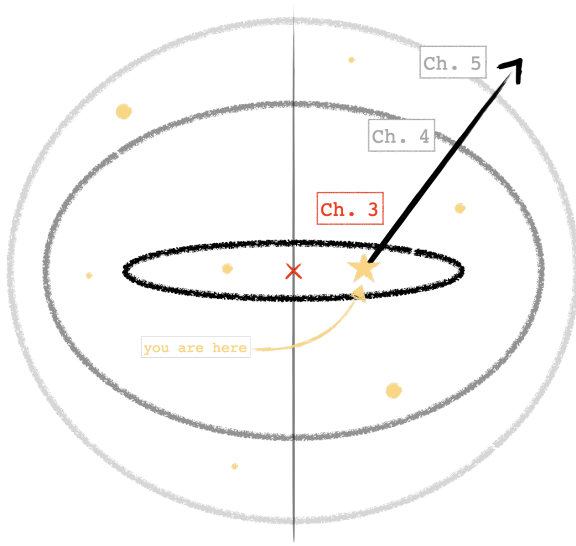

Figure 3.1. Traveling through our Galaxy: the disk system.

The following chapter is adapted from Dietz et al. (submitted).

3.1 Introduction

The Milky Way's disk system is the most highly populated region of our Galaxy, and our position within this system enables the accumulation of a wealth of data to produce highly detailed characterizations to compare with numerical simulations of the thin- and thick-disk populations.

The thick-disk component was first formally proposed by Yoshii (1982) and confirmed by Gilmore and Reid (1983), who demonstrated the need for an additional disk component when constructing Galactic stellar-density models. Since then, studies have uncovered rich substructure within the disk system, including the identification (Morrison et al., 1990) and subsequent confirmation (Beers et al., 2014; Chiba and Beers, 2000) of the metal-weak thick disk (MWTD). However, for almost three decades, despite numerous analyses, it remained unclear whether the MWTD was a separate population, or the metal-poor tail of the canonical thick disk. This situation may now be resolved; two recent analyses indicate that the MWTD comprises a distinct component with its own unique formation history. Carollo et al. (2019) used a sample of 9,258 local stars from the Sloan Extension for Galactic Understanding and Exploration (SEGUE; Yanny et al. 2009) program of the Sloan Digital Sky Survey (SDSS; York et al. 2000) to separate the MWTD from the thick-disk, finding the two populations to possess different characteristic kinematics, metallicities, and α-element abundances. An and Beers (2019) constructed a chemo-dynamical "blueprint" of Galactic components using photometric data from SDSS DR14 supplemented with deeper u-band photometry from the South Galactic Cap u-band Sky Survey (SCUSS; Gu et al. 2015) and astrometry from *Gaia* DR2 (Gaia Collaboration et al., 2018), which is less subject to bias compared to targeted spectroscopic data. These authors identified several key stellar populations in their chemo-dynamical maps, including a MWTD component that is clearly separable from the canonical thick-disk stellar population.

The origin story for the disk system has also become more complex with the discovery of a relatively massive accreted satellite, known alternatively as the *Gaia* Sausage or *Gaia*-Enceladus (the exact characteristics and potentially overlapping origins of these two proposed progenitors are still under debate; see, e.g., Evans 2020), which may have contributed to the formation of the thick disk via dynamical heating as it merged with the Milky Way (Belokurov et al., 2018; Helmi et al., 2018). The identification of a Splashed Disk population of stars (An and Beers, 2019; Belokurov et al., 2020) that may be connected with the proposed satellite collision(s) contributes an additional feature that could help constrain models for the formation of the disk system.

Recent reports of larger-than-expected populations of metal-poor stars within the disk system are also raising new questions about the assembly history of the Galaxy. The thin- and thick-disk metallicity distribution functions (MDFs) peak at approximately [Fe/H][1] = −0.1 and [Fe/H] = −0.6, respectively, with the MWTD covering an approximate range of $-1.8 <$ [Fe/H] < -0.8 (Carollo et al., 2007, 2010). However, Sestito et al. (2019) identified a significant population of ultra metal-poor stars (UMP; [Fe/H] < -4.0), well outside of the disk system's usual metallicity range, traveling on prograde orbits within 3 kpc of the Galactic plane. They followed-up on this finding in Sestito et al. (2020), using a combined sample of 1,027 very metal-poor (VMP) stars with [Fe/H] < -2.5, observed with the Large Sky Area Multi-Object Fibre Spectroscopic Telescope (LAMOST; Cui et al. 2012) and the Pristine survey (Aguado et al., 2019b; Youakim et al., 2017), demonstrating a statistically significant over-density of prograde VMP stars residing in the disk region. Similarly, Cordoni et al. 2020 find ∼11% of their 475 VMP stars from the SkyMapper survey (Wolf et al., 2018a) are within 3 kpc of the plane and have prograde orbits with low eccentricities. Di Matteo et al. 2020 even find an "ultra metal-poor thick disk", extending as far down as [Fe/H] ~ -6, within their sample of 54 VMP stars from the ESO Large Programme "First Stars" (Bonifacio et al., 2009), with interesting implications for

[1] $[A/B] \equiv \log_{10}(N_A/N_B)_* - \log_{10}(N_A/N_B)_\odot$, where N_A and N_B are the number densities of elements A and B, respectively.

the early dynamical history of the Galaxy.

Complementary to these discoveries of metal-poor disk populations, numerous CEMP stars have been identified in the disk system as well. In their analyses of metal-poor stars from the Hamburg/ESO survey, Beers et al. (2017) noted a population of CEMP-s stars in a kinematic and metallicity region usually associated with the MWTD. Yoon et al. (in prep.) find preliminary results indicating significant populations of CEMP stars in regions of energy-momentum space associated with the disk system, including a prograde population and a population with little to no angular momentum. Most notably, their sample includes a subset of UMP CEMP-no stars mainly found within the low-angular momentum population. These differences in kinematic and chemical characteristics suggest that at least two separate formation scenarios (e.g., from two accretion events) may be necessary to explain the presence of the CEMP stars in the disk populations.

In this paper, we continue this study of disk-like CEMP stars using low-resolution ($R \sim 1,300$) spectroscopy obtained by the AAOmega Evolution of Galactic Structure (AEGIS) survey (P.I. Keller), originally commissioned to study the evolutionary history of the thick-disk and halo systems of the Milky Way. As we demonstrate below, this sample includes two relatively nearby populations of CEMP stars, with potential implications for our understanding of the formation histories of the canonical thick disk and MWTD. We introduce the AEGIS data-set in Section 3.2, and describe its chemical abundances (Section 3.2.1) and kinematics (Sections 3.2.2 and 3.2.3). Section 3.3 presents our analyses of this sample with results. We discuss the implication of our results in the context of the Galactic formation history in Section 3.4. A brief summary of this work and our key findings are provided in Section 3.5.

3.2 Data

AEGIS is a spectroscopic survey conducted at the Australian Astronomical Telescope (AAT), using the dual beam (blue and red arms, covering ranges $\lambda = 3,700$ to 5,800 Å and $\lambda = 8,8400$ to 8,800 Å) AAOmega multi-object spectrograph to target populations of interest selected from the SkyMapper photometric survey. The resulting data-set comprises ∼70,000 stars with low-resolution spectroscopy ($R \sim 1,300$ for blue-arm spectra, $R \sim 10,000$ for red-arm spectra) and spans ∼4,900 deg.^{2} of sky in the Southern Hemisphere. A more complete description of the data-set can be found in Yoon et al. (2018), along with a detailed examination of the metallicity ([Fe/H]) and carbonicity ([C/Fe]) of the Galactic halo through the lens of the AEGIS survey.

3.2.1 Chemical Abundances

Stellar atmospheric parameters and a limited set of chemical abundances were derived with the non-SEGUE stellar parameter pipeline (n-SSPP; Beers et al. 2014, 2017). Effective temperature ($T_{\rm eff}$), surface gravity (log g), metallicity ([Fe/H]), and carbon abundances ([C/Fe]) for the AEGIS sample have been corrected to be more consistent with external high-resolution estimates, following the procedure described in Beers et al. (2014). Additionally, we apply the evolutionary carbon corrections developed by Placco et al. (2014) to take into account the surface carbon-abundance depletion expected to occur on the upper red giant branch. For this sample, mean errors on $T_{\rm eff}$, log g, [Fe/H], and [C/Fe] are approximately 75 K, 0.2 dex, 0.1 dex, and 0.1 dex, respectively.

As mentioned in Section 1.2, Yoon et al. (2016) showed that CEMP-no and CEMP-*s* stars can be classified using only absolute carbon abundance, A(C), making larger, medium-resolution samples like the AEGIS data-set available for CEMP sub-class analyses. Because the division between CEMP-no and CEMP-*s* stars can vary based on temperature and luminosity class, here we limit ourselves to the two categories for which the $A(\mathrm{C})$ divisions are most apparent in this sample: 1) giants and sub-giants (G/SG) and 2) main-sequence dwarfs and turn-off stars (D/TO). We use divisions of $A(\mathrm{C}) = 7.1$ and $A(\mathrm{C}) = 7.6$ for the G/SG and D/TO classes, respectively, as suggested by Yoon et al. (2018) in their analysis of the AEGIS data-set. After removing duplicate measurements and measurements with signal-to-noise ratios $<$10, there are 1,061 G/SG CEMP stars and 421 D/TO CEMP stars identified in the AEGIS sample in total. The combined sample of these classes comprises 660 CEMP-no and 822 CEMP-s stars.

We note that stellar temperature can affect our ability to adequately measure a star's carbon abundance. Compared to stars with strong carbon enhancements, those with moderate carbon enhancements can be difficult to detect in warmer ($T_{\mathrm{eff}} \gtrsim 5,750\,\mathrm{K}$, see Figure 3.2) stars, producing a spurious over-abundance of high-$A(\mathrm{C})$, high-T_{eff} stars (in other words, a higher CEMP-s to CEMP-no ratio) in samples that include higher-temperature stars. Application of such a cut on temperature would substantially reduce our CEMP sample size, so we choose to present the sample without temperature restriction in the following analyses, but make note of the effects that a temperature limit might have on our results, where appropriate.

3.2.2 Kinematic Parameters

Radial velocities were derived using the n-SSPP analysis of the high-resolution red arm of the AEGIS spectra. A correction of $-24.6\,\mathrm{km\,s^{-1}}$ was applied to all radial velocity values to account for an offset between the n-SSPP values and radial velocities derived using Ca triplet lines (at λ = 8498, 8542, 8662 Å) from the red-arm spectra (Navin, C. A., private communication). Proper motions from *Gaia* DR2 (Gaia Collaboration et al., 2018) are available for the majority ($\sim$98%) of the sample. For the remaining $\sim$2%, proper motions were averaged from a variety of catalogues (including Hipparcos, Tycho-1, and Tycho-2, as described in Beers et al. 2014). We

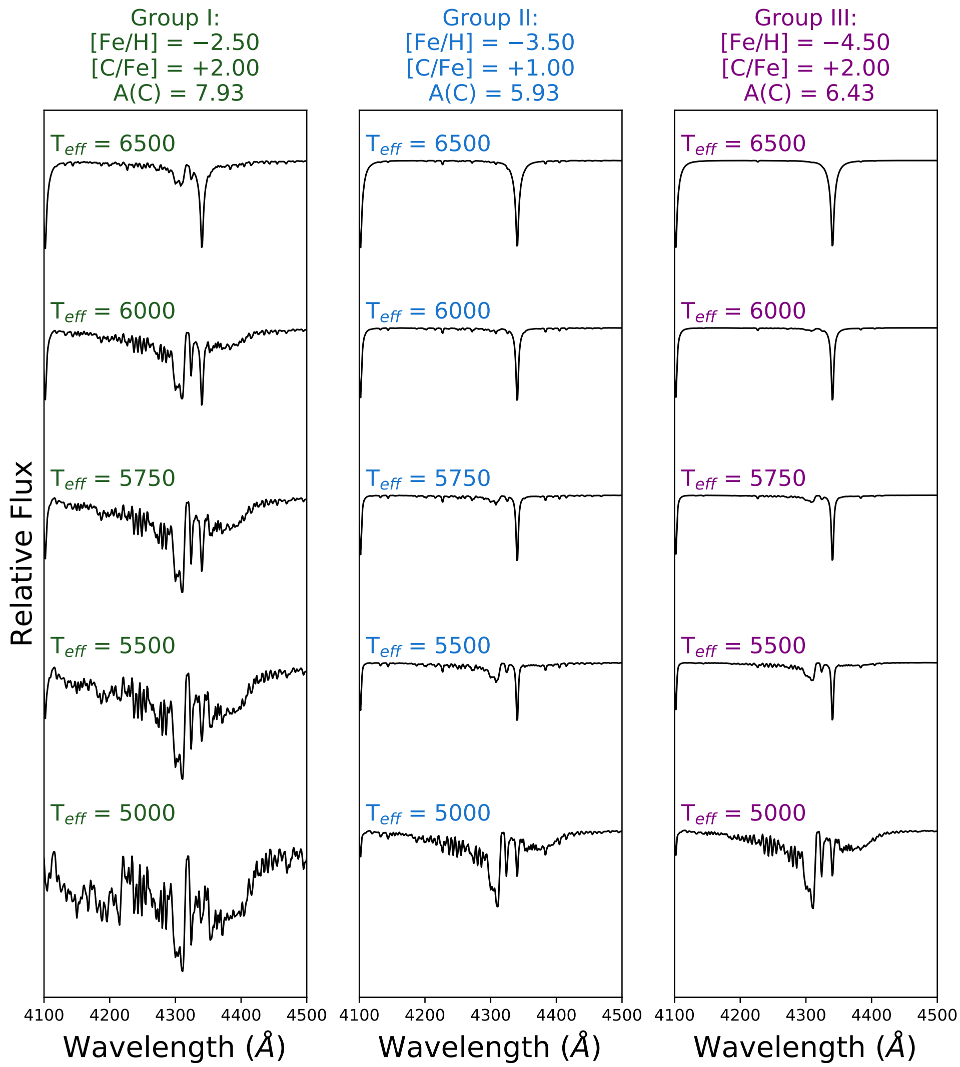

Figure 3.2. A figure illustrating the differences in carbon enhancements (and carbon enhancement detectability) between simulated spectra of different temperatures. The left column shows a Group I (CEMP-s, highest carbon enhancement) star, the middle column shows a Group II star (CEMP-no, moderate carbon enhancement), and the right column shows a Group III star (CEMP-no, moderate carbon enhancement). Each spectrum is simulated at five different temperatures, from $T_{\rm eff} = 6,500\,\mathrm{K}$ (top) to $T_{\rm eff} = 5,000\,\mathrm{K}$ (bottom). The molecular carbon feature at $\sim 4{,}300\,\text{Å}$ (the CH band) is most apparent in low-temperature, high-A(C) stars and least apparent in high-temperature, low-A(C) stars. Credit: K. Rasmussen.

adopt a +0.054 correction to all *Gaia* parallaxes as prescribed by Schönrich et al. (2019), and derive distances from the inverted parallaxes for all stars with <20% relative parallax uncertainty (∼54% of the sample). The remaining ∼46% of the stars in our sample are assigned photometrically derived distances, following the procedure outlined in Beers et al. (2000), as modified by Beers et al. (2012).

3.2.3 Kinematic Derivations

The derivation of kinematic parameters follows the the procedure outlined in Chapter 2, with some minor modifications:[2] in this work, we use $R_{\odot} = 8.2\,\mathrm{kpc}$ for the distance to the center of the Galaxy (Bland-Hawthorn and Gerhard, 2016), $v_{\mathrm{LSR}} = 236\,\mathrm{km\,s^{-1}}$ for the local standard of rest (LSR) velocity (Kawata et al., 2019), and $(U, V, W)_{\odot} = (-11.10, 12.24, 7.25)\,\mathrm{km\,s^{-1}}$ for the motion of the Sun with respect to the LSR (Schönrich et al., 2010).

To estimate uncertainties on the orbital parameters, we follow the Monte Carlo sampling procedure presented in 2. We note here that this sampling process should take into account the correlations between the input parameters in order to derive the most accurate uncertainty. However, correlation coefficients are not available for the kinematic parameters given in the original AEGIS data-set (as noted above, we use the original kinematic parameters given in the AEGIS data-set for 100% of our radial velocities, ∼2% of our proper motions, and ∼46% of our distances). Including correlation coefficients in our calculations for stars with *Gaia* kinematics results in (at most) a median difference of ∼1% and mean difference of ∼6% in derived uncertainties for the orbital parameters used in this work when compared to uncertainties calculated without correlation coefficients. Because this difference is minor, we choose to neglect correlations between input parameters in order to treat the subsets of our data with

[2]The research presented in this chapter is the most recent of all work included in this document, so the kinematics code used here includes some minor updates.

AEGIS and *Gaia* kinematics in the same manner.

To avoid identifying any potentially spurious features, we limit our sample to stars with uncertainties on $Z_{\rm max}$ less than 1 kpc and uncertainties on L_z less than 250 kpc km s^{-1} (that is, no greater than our chosen bin size in Figure 3.3). After applying this restriction, we have a total of 51,946 stars in the $Z_{\rm max} < 5$ kpc region, 427 of which are CEMP-*s* stars and 223 of which are CEMP-no stars.

3.3 Analyses

We begin our analysis by identifying populations of interest close to the Galactic plane. Angular momentum (L_z) distributions for the sample are divided into sections based on maximum orbital extent from the Galactic plane, $Z_{\rm max}$, as shown in Figure 3.3.

From left to right, the columns of Figure 3.3 show the distributions for all stars, the CEMP stars, and the CEMP-*s* (blue) + CEMP-no (red) stars.

In the full sample (left column of panels), the disk clearly dominates at all $Z_{\rm max}$ ranges, producing a strongly prograde peak at $L_z > 1000$ kpc km s^{-1}. This peak includes both thin- and thick-disk stars, but it should be noted that the thin disk is not fully represented here due to the metallicity upper limit within the AEGIS sample ([Fe/H] ≤ 0.3). The inner-halo component ($L_z \sim 0$ kpc km s^{-1}) becomes more visible at $3 \leq Z_{\rm max} < 5$ kpc, although the disk system still retains a robust peak even at these heights.

In the CEMP sub-sample (middle column of panels in Figure 3.3), at least two populations appear to be present for all $Z_{\rm max}$ ranges. We have fitted the L_z distributions with Gaussians using the `scikit-learn` mixture package in order to approximate the general features of these populations (we have also performed similar fits on the total sample so that we can compare the characteristics of the total sample to the CEMP sub-samples). Each range contains a mildly prograde peak and a strongly prograde

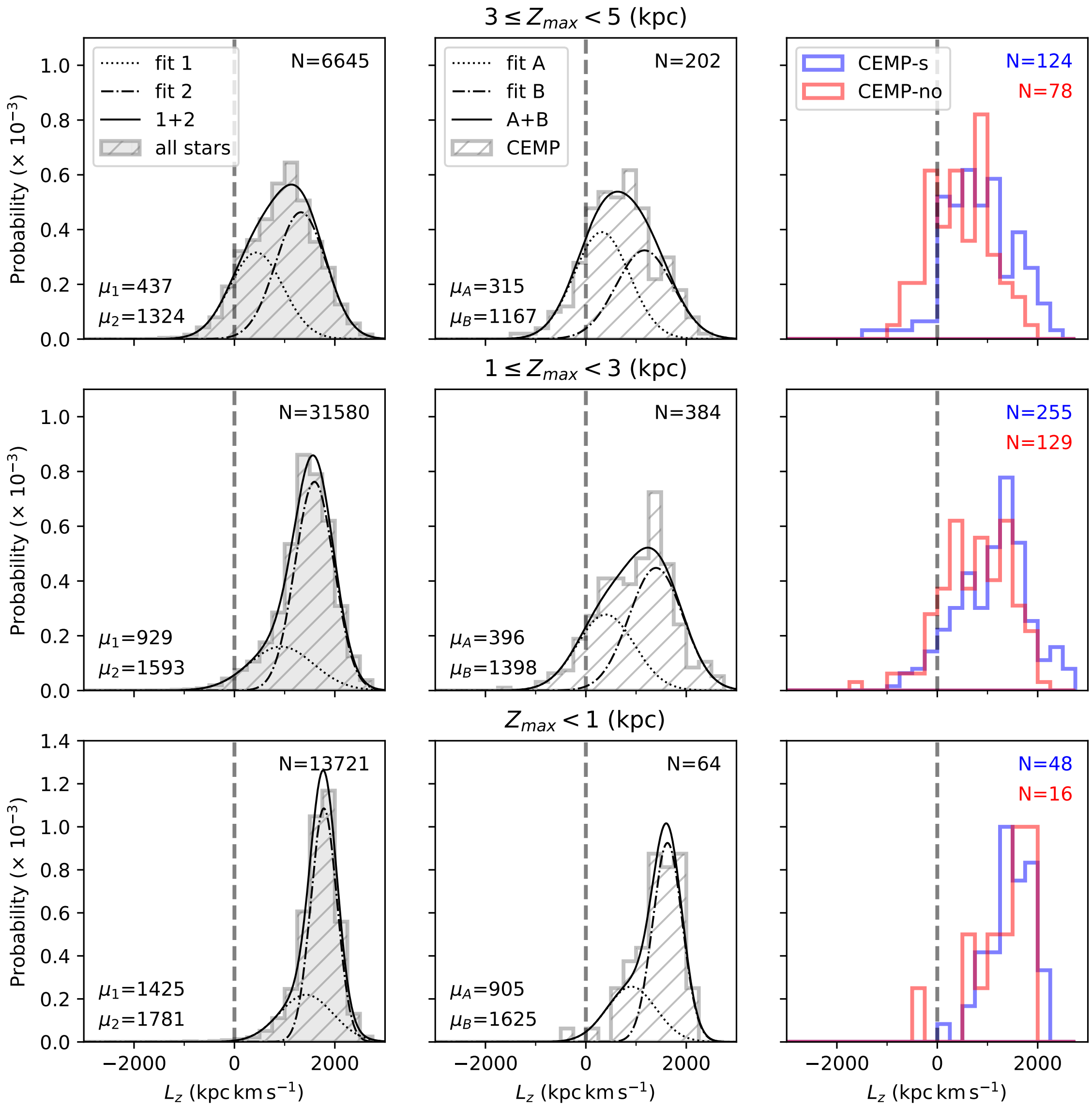

Figure 3.3. Angular momentum distributions for the sample over three different ranges of $Z_{\max}$. The left column of panels shows all stars with valid kinematics, the middle column shows the subset of CEMP stars, and the right column shows the CEMP subset divided into CEMP-s (blue) and CEMP-no (red) distributions. The total population (left) and the CEMP subset (middle) are each fit with two-component Gaussian distributions. The means of these fits are indicated in the bottom left-hand corner of these panels. The number of stars plotted, N, is given in the upper right-hand corner of each panel. For the right column, N is given for the CEMP-s and CEMP-no subsets in blue and red, respectively. A dashed line marks $L_z = 0\,\mathrm{kpc\,km\,s^{-1}}$ for reference in each plot.

peak—we refer to these as populations “A” and “B”, respectively, for the remainder of this work. The low-momentum peak is likely associated with the inner-halo population, a rich source of CEMP stars, which would account for the larger relative proportion of population A at high $Z_{\rm max}$. Population B displays a strong net rotation and decreases in relative significance with increasing $Z_{\rm max}$, which suggests it may be a part of thick-disk/MWTD.

The fits for population A peak at 905, 396, and 315 kpc km s^{-1}, from the low to high $Z_{\rm max}$ ranges. The fits for population B peak at 1625, 1398, and 1167 kpc km s^{-1}, from the low to high $Z_{\rm max}$ ranges. These fits are mainly meant to provide an overview of the characteristics of our CEMP populations, not to create a strict definition for each population, so it is understandable that the location of the peaks varies somewhat with $Z_{\rm max}$ (especially at $Z_{\rm max} < 1$ kpc, where population A is weakly represented). It is interesting to note here that population B lags an average of ~ 170 kpc km s^{-1} behind the dominant, strongly prograde peak of the total sample.

Both populations are dominated by CEMP-*s* stars, which is not surprising, given that we currently understand CEMP-no stars to have predominantly ex-situ origins (e.g., Lee et al., 2017, 2019; Yoon et al., 2018, 2019, 2020), though the relative strength of this ratio appears to vary based on the sub-sample being considered. In the full sample, the ratio of CEMP-*s* to CEMP-no stars is roughly twice as large in population B as it is in population A, which could suggest different origins for the CEMP stars within these populations.

When we consider the sample restricted to $T_{\rm eff} < 5750$ K, CEMP-*s* stars still dominate both populations, but the CEMP-*s* to CEMP-no ratio varies much more unpredictably, making it challenging to make any definitive statement on the chemical origins of population A versus population B. Note that the low-temperature sample contains significantly fewer CEMP stars than the full sample; a larger sample of cool CEMP stars in this region may be needed to more fully explore these populations.

TABLE 3.1

POPULATIONS A & B CEMP RATIOS

	Pop.	$0 < Z_{\max} \leq 1$	$1 < Z_{\max} \leq 3$	$3 < Z_{\max} \leq 5$
All $T_{\rm eff}$	A	**1.8** (17)	**1.3** (143)	**1.1** (110)
	B	**3.7** (47)	**2.7** (241)	**2.5** (92)
$T_{\rm eff} < 5750\,{\rm K}$	A	**3.7** (14)	**1.9** (60)	**1.1** (68)
	B	**2.0** (6)	**2.1** (56)	**1.8** (14)

The CEMP-s to CEMP-no ratios for populations A and B are given in blue for each range shown in Figure 3.3, for the full sample and for a temperature-limited sample. The total number of CEMP stars in each population for the given range is listed in parentheses.

The presence of a large number of CEMP stars in a region of the Galaxy usually associated with disk stars is worthy of further investigation. To aid in interpretation of these data, we present the same samples of stars shown in Figure 3.3 in a set of MDFs in Figure 3.4. Rows are sub-divided into the same $Z_{\max}$ ranges used in Figure 3.3, while columns are separated into L_Z ranges. Population counts and statistics are given in the upper left-hand corner of each sub-plot.

Inspection of Figure 3.4 shows that the strongly prograde stars in our sample are generally more metal rich than the mildly prograde or retrograde stars, as expected for a disk-dominated sample. As in Figure 3.3, the disk is robustly represented (high metallicity, strongly prograde) at both low and high $Z_{\max}$, and here too we observe the growing inner-halo contribution ([Fe/H] ~ -1.6, $L_z \sim 0\,{\rm kpc\,km\,s^{-1}}$) in the highest $Z_{\max}$ range.

Figure 3.4 also includes CEMP, CEMP-s, and CEMP-no counts for the each kinematic range, listed in black, blue, and red, respectively. The relative percentage of CEMP stars compared to all stars is noted in parentheses next to the CEMP

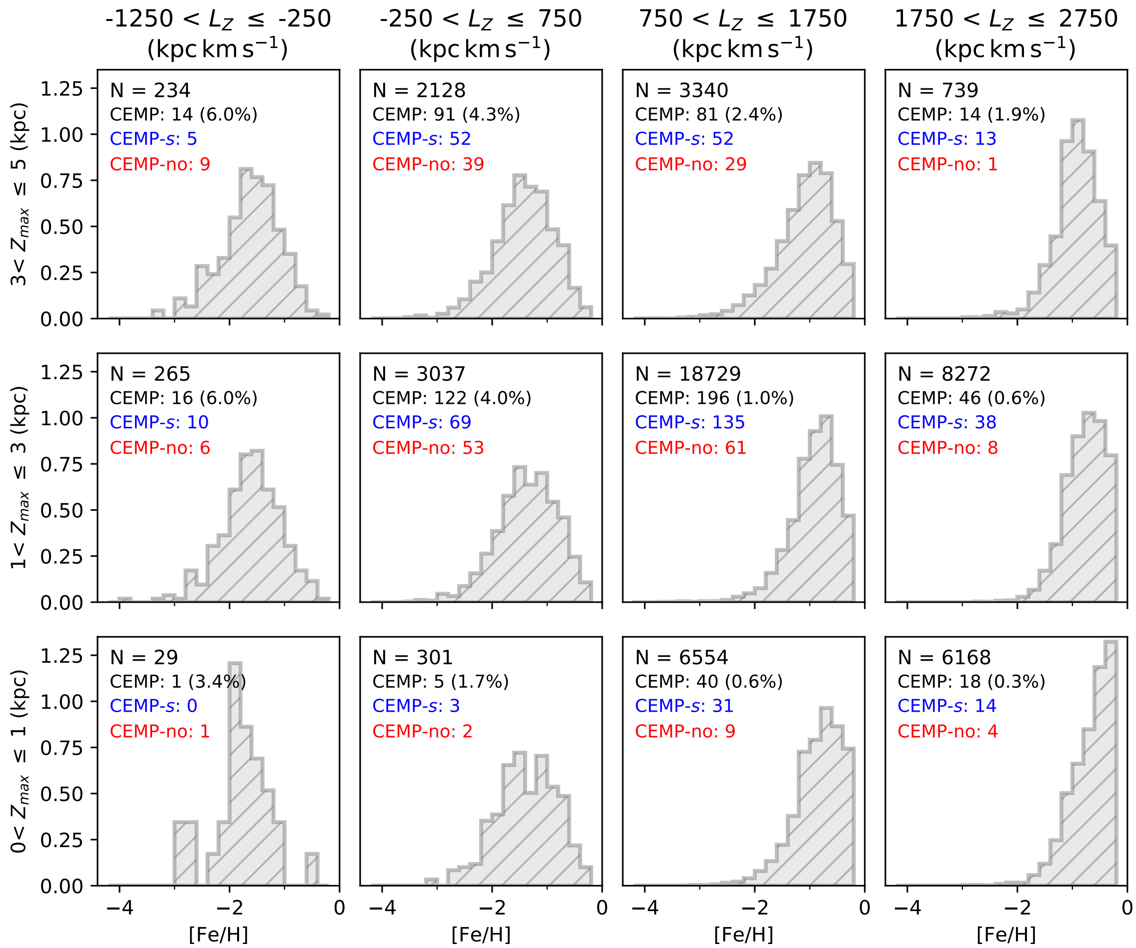

Figure 3.4. Normalized MDFs for the sample over three different ranges of Z_{max} (rows) and four different ranges of L_Z (columns). The total star count (N) is noted in the upper left-hand corner of each plot. The total CEMP count and the percentage of CEMP stars (relative to total count) is listed below N. CEMP-*s* and CEMP-no counts are given in blue and red, respectively.

count. Although the strongly prograde stars (two right-most columns) have the most CEMP stars by number, they possess the smallest relative percentages of CEMP stars compared to the total population. We find a relatively large number of CEMP stars in these regions simply because these regions of the kinematic space were sampled the most in the observations. Nevertheless, the presence of even a small relative percentage of CEMP stars moving in tandem with the disk is interesting, and may provide insight into the disk's formation history. These sub-samples correspond to the CEMP-s-rich population B noted above.

Population A can be seen more clearly in the lower-L_Z ranges (two left-most columns). These regions contain small absolute numbers of CEMP stars, but possess the highest CEMP percentages. A feature of note here is the double metallicity peak seen in both the $Z_{\max} \leq 1\,\mathrm{kpc}$ and $1 < Z_{\max} \leq 3\,\mathrm{kpc}$ plots within the $-250 < L_Z \leq 750\,\mathrm{kpc\,km\,s^{-1}}$ range. Peaks at approximately [Fe/H] $= -1.0$ and [Fe/H] $= -1.7$ are present in the $Z_{\max} \leq 1$ kpc sub-sample, becoming less distinct as we move farther from the plane. It should be noted that the shape of this component varies somewhat with binning, though a feature similar to the [Fe/H] $= -1.0$ peak can also be seen in Figure 4 of An and Beers 2019; the authors suggest the Splashed Disk, presented in Belokurov et al. (2020), as one possible source.

3.4 Discussion

We have identified two CEMP populations of interest in the disk system of the Milky Way: the mildly prograde population A ($L_z < 1000\,\mathrm{kpc\,km\,s^{-1}}$) and the strongly prograde population B ($L_z > 1000\,\mathrm{kpc\,km\,s^{-1}}$), both containing an enhancement of CEMP-s stars relative to CEMP-no stars.

Although many population A stars orbit close to the Galactic plane, this population may be linked to the inner-halo population, particularly since it possesses a similar relative percentage of CEMP-s stars (53-65%, depending on $Z_{\max}$) to that given by Carollo et al. (2014) for this component (57%). An and Beers (2019) found a strong inner-halo population even at slices of $|Z|$ close to the plane, estimating two-thirds of the metal-poor stars in the $1 < |Z| < 2\,\mathrm{kpc}$ region of their data to be *Gaia*-Enceladus stars. Although the mildly prograde motion of population A is at odds with the slightly retrograde motion derived by Helmi et al. (2018) for *Gaia*-Enceladus, a common origin cannot be ruled out. Both population A and *Gaia*-Enceladus span a range of velocities, including both prograde and retrograde rotation, and the latter presumably carries a similar CEMP-s percentage to that quoted in Carollo et al. (2014), as *Gaia*-Enceladus is proposed to make up a large portion of the inner-halo population. It is also possible that population A is instead a part of the *Gaia* Sausage, which possesses a slightly higher mean L_z ($L_z \sim 0\,\mathrm{kpc\,km\,s^{-1}}$) than *Gaia*-Enceladus (bounded by $-1,500\,\mathrm{kpc\,km\,s^{-1}} < L_z < 500\,\mathrm{kpc\,km\,s^{-1}}$ in Helmi et al. 2018). The scientific community has not yet come to a consensus on which scenario better describes the formation of the ex-situ inner-halo population, the *Gaia* Sausage or *Gaia*-Enceladus; it would be interesting to revisit the characteristics of population A in the future, when more is known about the nature of the main inner-halo progenitor(s).

Population B possesses kinematic characteristics more in-line with the thick-disk system ($L_z \sim 1,500\,\mathrm{kpc\,km\,s^{-1}}$, close to the Galactic plane), and the low metallicity of our CEMP stars (by definition) necessarily designate them as members of the MWTD, which spans an approximate range of $-1.8 <$ [Fe/H] < -0.8 (Carollo et al., 2010). Beers et al. (2017) and Yoon et al. (in prep.) also noted significant CEMP-s populations in MWTD-associated regions of their samples. It is unclear whether these stars formed in-situ or were imported into the disk system. CEMP stars are not expected to be common in a well-mixed, gas-rich environment like the disk, but peak B makes up a very small percentage of the total disk-system stars within its kinematic region, so in-situ formation is not out of the question. For instance, Sestito et al. (2020) propose a possible in-situ formation pathway for their population of disk VMP stars, involving pockets of pristine gas in the proto-disk and radial migration. On the other hand, both Carollo et al. (2019) and An and Beers (2019) find evidence in their data clearly indicating a separate MWTD population, which suggests a potential ex-situ origin for population B stars. Lian et al. (2020) propose a two-pronged formation scenario for the thick disk, including a late starburst in the outer disk, potentially caused by the accretion of a gas-rich dwarf galaxy. Although the abundance-space explored in their analyses ([Fe/H] > -1) does not extend to the low-metallicity regimes probed here, it is possible that this ex-situ outer thick disk is linked to population B. In the case of an accreted origin, the high relative fraction of CEMP-s stars in population B could indicate a (relatively) massive, gas-rich progenitor satellite, which would have preferentially formed more CEMP-s stars than CEMP-no stars, the latter being mostly accreted from less-massive progenitors such as UFDs (Yoon et al., 2019).

An investigation into the morphological groups introduced by Yoon et al. (2016) present in our CEMP sub-populations could be of interest, especially an analysis of the two classes dominated by CEMP-no stars, "Group II" and "Group III". These groups are thought to have different progenitors due to their distinct A(C)-[Fe/H] and A(C)-A(Na, Mg) relations, which could provide insight into the origins of population A versus B, but our sample does not possess sufficient numbers of potential Group III stars (which can be difficult to identify, due the overlap between Groups II and III) to make any statistically interesting statements about the Group II/Group III ratio in either population. However, Yoon et al. (in prep.) find a strong Group III population in a region of energy-momentum space potentially associated with population A (low-energy, $L_z < 1000\,\mathrm{kpc\,km\,s^{-1}}$) based on a high-resolution literature sample of Group III CEMP-no stars. Yoon et al. (2019) found Group III stars to be preferentially accreted from UFDs, so further sampling of the population A region may help constrain the assembly history of the nearby halo, as well as potentially contribute to the as-yet sparsely populated Group III region of the A(C)-[Fe/H] space.

3.5 Summary and Conclusions

We present a chemo-dynamical analysis of $Z_{max} < 5\,\mathrm{kpc}$ stars from the AEGIS survey, focusing on CEMP populations within this region. We find two key CEMP populations of interest close to the Galactic plane: a mildly prograde population

($L_z < 1000\,\mathrm{kpc\,km\,s^{-1}}$, population "A") and a strongly prograde population ($L_z > 1000\,\mathrm{kpc\,km\,s^{-1}}$, population "B"). Population A contains a mild over-abundance of CEMP-s compared to CEMP-no stars ($\sim$53-65% CEMP-s), which, in combination with its kinematic characteristics (low L_z, dominant farther from the Galactic plane), lead us to associate this population with the inner-halo component. These stars could belong to either of the proposed ex-situ inner-halo progenitors: the *Gaia* Sausage or *Gaia*-Enceladus.

Population B also contains preferentially more CEMP-s stars than CEMP-no stars (potentially with a higher ratio than population A), but a larger number of low-$T_{\rm eff}$, $Z_{\rm max} < 5\,\mathrm{kpc}$ CEMP stars than our current sample ($\sim$200) is needed to more fully explore this possibility), and can be kinematically and chemically associated with the MWTD. This clump of (mainly) CEMP-s stars within the MWTD has been seen in other samples as well, including in Beers et al. (2017) and Yoon et al. (in prep.). We propose both in-situ and ex-situ origins for this population, such as pockets of pristine gas in the proto-disk (in-situ), as suggested by Sestito et al. (2020), and a relatively massive merger of a gas-rich progenitor satellite (ex-situ).

Although the stellar halo (and the outer-halo component in particular) contains the highest relative ratio of metal-poor and CEMP stars compared to other Galactic components, a surprising number of these ancient tracer populations are emerging in recent surveys of the disk system. We present our own findings within the AEGIS data-set as potentially useful constraints for evolutionary models of the Milky Way, particularly with regards to the creation of the ex-situ inner-halo and the formation of the MWTD. Future surveys of the disk and halo systems will undoubtedly aid in interpretation of the CEMP behaviors noted here, and ongoing efforts to increase the number of known Group III stars could provide further constraints on the origins of these populations.

CHAPTER 4

THE DUAL HALO

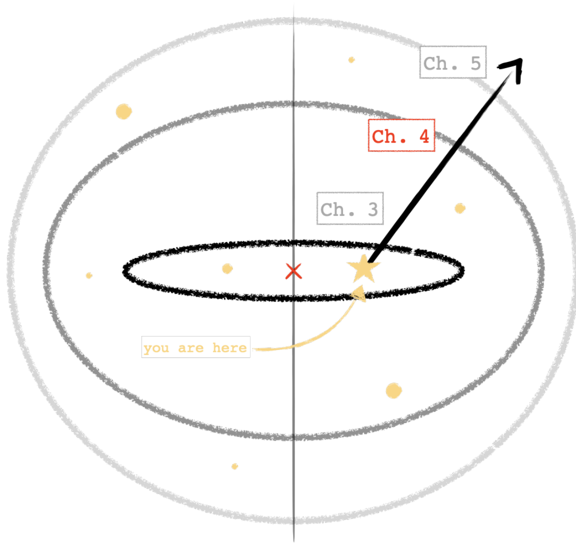

Figure 4.1. Traveling through our Galaxy: the dual halo.

4.1 The History of the History of the Halo

The stellar halo of the Milky Way has experienced a rich and complex evolutionary path over the past few billion years—and so has the scientific community's understanding of the halo itself (albeit on a much smaller timescale). Beginning, as many overviews of the halo do, with the Eggen et al. (1962) monolithic collapse scenario (an entirely "in-situ" halo), further growing in complexity with accreted, sub-galactic fragments donated by Searle and Zinn (1978) (now with "ex-situ" contributions), and continuing over the years with many observations of the different characteristics possessed by the inner and outer portions of the halo (e.g., Caputo and Castellani (1984); Chiba and Beers (2000); Sommer-Larsen et al. (1997)). Some of these authors claim the presence of a kinematic gradient within the halo, while others propose multiple formation pathways to explain the contrasting behavior of the near and far halo.

A more formal "dual halo" was first proposed by Carollo et al. (2007), marking a significant turning point in "the history of the history of the halo". The authors asserted that the stellar Galactic halo is best represented by an inner- and outer-halo, which differ in their chemo-dynamical characteristics and, presumably, their origins. Of the two, the inner-halo is (relatively) more metal rich (with an MDF peak at [Fe/H] ~ -1.6), exhibits little significant net rotation, and dominates the halo at Galactocentric distances up to $r \sim 15 - 20\,\mathrm{kpc}$. The outer-halo is more metal-poor (with an MDF peak at [Fe/H] ~ -2.2), exhibits a net retrograde rotation ($v_\phi \sim -80\,\mathrm{km\,s^{-1}}$), and dominates the halo beyond $r \sim 20\,\mathrm{kpc}$[1] (Carollo et al., 2007, 2010).

Schönrich et al. (2011) rejected the "alleged duality of the Galactic halo", on the grounds that distance estimate biases in Carollo et al. (2010) led to the artificial identification of a two-component halo. They also took issue with what they believed to be the misclassification of some stars. Beers et al. (2012) agreed with the misclassification assertions (and subsequently reclassified the stars in question), but rebuffed the Schönrich et al. (2011) claim of large distance overestimations, showing that a re-analysis of the Carollo et al. (2010) data still resulted in the same (dual

[1]Even >20 years prior we see mention of an "inner edge of the outer-halo" around $r \sim 25\,\mathrm{kpc}$ from Carney (1984).

halo) conclusion.

The duality of the halo was such a contentious topic and so difficult to establish in part because of the overlapping nature of the inner- and outer-halo, making it difficult to fully disentangle their intermingling populations. Here it may be useful to define the difference between the inner-halo region (IHR) and inner-halo population (IHP) (as well as the similarly-named OHR and OHP of the outer-halo). IHP stars might be called "true" inner-halo stars; that is, stars that share a common origin and traits distinct from other Galactic components. These stars usually reside in the IHR ($r <$ 15 - 20 kpc, as mentioned above), but their orbits may carry them into regions of the Galaxy more associated with the disk, or with the outer-halo. The same is true for the outer-halo: an extremely metal-poor, highly retrograde star traversing through the solar neighborhood at $r \sim 10$ kpc could quite possibly be OHP star moving through the IHR.[2]

Disentangling the halo system is of particular interest to Galactic archaeologists due to its high concentration of metal-poor stars (especially in the outer-halo). Although the center of the Galaxy hosts the most metal-poor stars by *number*, the halo hosts a larger relative $fraction$ of metal-poor stars (Starkenburg et al., 2017).

The halo also hosts relatively large populations of CEMP stars, with the inner- and outer-halos possessing different ratios of CEMP-s and CEMP-no stars (see Section 1.2 for refresher on CEMP stars and their sub-classes). As CEMP stars are frequently used as tracers of various (often ancient) stellar populations, further study of halo CEMP populations contributes useful information towards understanding the halo's origin, as discussed in detail in the following sections.

The kinematic and chemical characteristics of the inner- and outer-halo compo-

[2]One way to combat this confusion is to use a star's derived orbital properties, rather than its observed location, to associate it with the appropriate Galactic component (i.e., using r_{apo} instead of r). The obvious drawback, though, is that the results will vary somewhat depending on the researcher's choice of Galactic potential.

nents summarized above have potential implications for the assembly history of the halo system, and further analyses of these components continues to aid researchers in targeting sub-populations of interest (i.e., the most ancient stars, the most metal-poor stars, stars from specific accretion events). This chapter focuses mainly on different methods of separating halo populations (Section 4.2)—using the procedure outlined by Carollo et al. (2014) in Section 4.2.1 and using an alternative statistical approach in Section 4.2.2—but will also provide an overview of key changes in our understanding of the halo system following *Gaia* DR2 (Section 4.3).

4.2 Separating the Dual Halo

In this section I introduce two methods of separating the inner- and outer-halo components based on CEMP populations. In particular, I highlight the effects of high-precision astrometry from the *Gaia* satellite and the new CEMP classification system introduced by Yoon et al. (2016) on the efficacy of these methods, and how this information might aid in analyses of future samples.

4.2.1 Carollo et al. 2014 Method

Carollo et al. (2014) compiled a sample comprised of 42 CEMP-*s* and 46 CEMP-no halo stars to examine CEMP patterns present within the dual halo system. They assigned each star membership to the inner-halo ("I"), outer-halo ("O"), or a transition zone ("T") between the two components. The authors established their assignment system by first observing the kinematic behavior of a sample of $\sim$ 8,000 SDSS/SEGUE calibration stars, pre-selected to be likely halo candidates ($r_{\rm apo} >$ 15 kpc, [Fe/H]≤ -1.3). They used this larger sample to determine the approximate kinematic transitions between each halo component, deriving a set of membership criteria using $r_{\rm apo}$ and E. Stars are assigned "I" if $r_{\rm apo} <$ 15 kpc, or if $r_{\rm apo} >$ 15 kpc and $E < -1.1 \times 10^5\,{\rm km^2 s^{-2}}$. Stars are assigned "O" if $r_{\rm apo} >$ 15 kpc and $E > -0.18 \times 10^5\,\mathrm{km^2s^{-2}}$. Stars with intermediate properties ($r_{\rm apo} > 15\,\mathrm{kpc}$ and $-1.1 \times 10^5 < E < -0.18 \times 10^5\,\mathrm{km^2s^{-2}}$) are assigned "T".

Using this system, the authors found the outer-halo to contain a relative percentage of 70% CEMP-no and 30% CEMP-s stars, while the inner-halo region comprises 43% CEMP-no and 57% CEMP-*s* stars. These results reinforce the argument in favor of a dual, rather than single, halo system, and have potential implications for the chemo-dynamical evolution history of the halo.

A detailed description of the properties of CEMP-*s* versus CEMP-no stars can be found in Section 1.2.1, but a brief summary is given here for convenience. CEMP-*s* stars preferentially occur in binary systems, receiving their excess carbon and *s*-process enhancements via binary mass transfer from a more evolved companion. The CEMP-no progenitor is slightly more uncertain, but, because CEMP-no stars are *not* preferentially associated with binaries and tend to populate the lowest-metallicity tails of Galactic MDFs, it is hypothesized that CEMP-no stars may be true second-generation (Pop. II) stars, receiving their carbon enhancements via natal cloud enrichment from the very first stars (Pop. III) to form in the Universe; this theory has gained support through high-resolution observations of select highly metal-poor CEMP-no stars, e.g., BD+44 493, HE 0020-1741 (Placco et al., 2016; Roederer et al., 2016).

Carollo et al. (2014) also reference several simulations (e.g., Tissera et al. 2014) that find the outer-halo to be made from less-massive sub-galactic fragments than the inner-halo. Combined with the contrasting CEMP ratios observed in the inner- and outer-halo, the following picture emerges: the outer-halo may have been built from smaller satellites with truncated star formation histories, resulting in mainly low-mass, metal-poor Pop. II stars. Larger satellites (or in-situ formation within the proto-Milky Way) would provide sufficient gas for continued star formation (a combination of Pop. II and Pop. I stars), resulting in the more chemically-enriched

CEMP-s stars.

To test the reproducibility of these results and the robustness of this method, I apply the Carollo et al. (2014) classification system to two data-sets with different characteristics, as detailed below.

4.2.1.1 Results: Yoon et al. (2016; High-Resolution Spectroscopy)

Here I use the sample of 305 CEMP stars compiled by Yoon et al. (2016) (hereafter "Y16") for their study of CEMP progenitor populations. Proper motions are compiled from a variety of catalogs, mainly the fourth U.S. Naval Observatory CCD Astrograph Catalog (UCAC4; Zacharias et al. 2013) and the Positions and Proper Motions Star Catalogue-XL (PPMXL; Roeser et al. 2010). Radial velocities are taken from the literature where available and photometric distances estimated using the procedure described in Beers et al. (2000).

After removing stars with uncertain classifications (e.g., upper limit estimations on key chemical abundances), the remaining sample consists of 127 CEMP-no and 134 CEMP-s stars. Of these stars, sufficient kinematic information can be compiled for 179 stars, which are then run through the kinematics pipeline described in Chapter 2. Note that I apply the same Stäckel potential used by Carollo et al. (2014)—this procedure can be replicated with alternative choices of Galactic potential, but the locations of the kinematic transitions between halo components will vary with different potentials and should be recalculated accordingly. After restricting the sample to reduce disk contamination ($Z_{\mathrm{max}} > 3\,\mathrm{kpc}$ and $r_{\mathrm{apo}} > 5\,\mathrm{kpc}$), the final sample consists of 91 bound CEMP stars (29 CEMP-s, 62 CEMP-no).

In the time since the first version of this sample was initially compiled, more precise astrometric data have been made available for public use. In Spring 2018, *Gaia* DR2 made precise parallaxes and proper motions available for $\sim 10^9$ stars to a limiting magnitude of G = 21. To illustrate our changing understanding of the structure of the halo, I present both the pre- and post-*Gaia* results for the Y16 sample to quantify the effect that more accurate kinematics have on studies of the halo (and other Galactic components). The *Gaia*-supplemented sample (*Gaia* distances and proper motions are available for the majority of the sample, original radial velocities are largely retained) results in 110 bound CEMP stars (49 CEMP-s, 61 CEMP-no).

Stars are assigned halo membership based on the Carollo et al. (2014) procedure outlined above (see Appendix A.2.4 for full code). The results are summarized in Table 4.1

TABLE 4.1

Y16 CEMP RATIOS

	Type	I	O	T
Original	CEMP-s	13 (31%)	12 (40%)	4 (21.1%)
	CEMP-no	29 (69.1%)	18 (60%)	15 (79%)
Gaia DR2	CEMP-s	27 (42.9%)	11 (57.9%)	11 (39.3%)
	CEMP-no	36 (57.1%)	8 (42.1%)	17 (60.7%)

Dual halo designations for the Y16 sample, based on the method used in Carollo et al. (2014). CEMP-s and CEMP-no counts and relative percentages are given for each component and two different versions of the sample (using pre- and post-*Gaia* kinematic input parameters).

Because the pre-and post-*Gaia* inner- and outer-halo CEMP ratios differ significantly, it is important to take a closer look at what exactly changed. The 91 stars with original kinematics and the 110 stars with *Gaia*-supplemented kinematics share

55 common stars (the set of stars not shared between the two includes stars that were designated as unbound or possible disk contaminants in one sample but not the other). Of the 55 shared stars, 37 retained the same halo category designation (I, O, or T) in each kinematic sub-sample while 18 stars moved to a new category. Of those 18, 10 stars shifted between a halo component and the transition zone (I $\leftrightarrow$ T or O $\leftrightarrow$ T) while 8 stars swapped inner/outer components completely (I $\leftrightarrow$ O). Because the sample size used is so small, if even a few stars change categories there may be a large effect on the resulting CEMP ratios. If the post-*Gaia* results are given more credence than the original sample's results due to higher-precision kinematics, the ratios presented in Table 4.1 would imply a mild CEMP-no dominance in the inner-halo and a mild CEMP-s dominance in the outer-halo, in contradiction with the findings of Carollo et al. (2014).

As mentioned in the previous chapter, an additional factor that may affect results is stellar temperature. Carbon is more difficult to detect in high-temperature stars ($T_{\rm eff} \gtrsim 5750\,$K, see Section 3.2.1, Figure 3.2), so we may be unintentionally under-counting hot CEMP stars. The hot CEMP stars we *are* able to detect will necessarily posses particularly strong carbon enhancements (CEMP-s), so the CEMP stars most-absent from our samples are likely the ones with more moderate carbon enhancements (CEMP-no). In short, if a sample includes a non-negligible quantity of hotter stars it may present an artificially boosted CEMP-s to CEMP-no ratio.

I re-apply the Carollo et al. (2014) analysis procedure, limiting the sample to stars with $T_{\rm eff} \leq 5,600\,$K. The results are summarized in Table 4.2.

Although the total stars in each kinematic sub-sample decreased by 20 to 30%, the overall results for the cool samples are not significantly different than those for the whole-temperature samples.

It is also possible that these results are being effected by the metallicity-distance

TABLE 4.2

Y16 DUAL HALO DESIGNATIONS

	Type	I	O	T
Original	CEMP-*s*	6 (22.2%)	10 (40%)	2 (16.7%)
	CEMP-no	21 (77.8%)	15 (60%)	10 (83.3%)
Gaia DR2	CEMP-*s*	21 (42%)	6 (54.6%)	8 (36.4%)
	CEMP-no	29 (58%)	5 (45.5%)	14 (63.6%)

Dual halo designations for cool ($T_{\rm eff} \leq 5,600$) stars the Y16 sample, based on the method used in Carollo et al. (2014). CEMP-*s* and CEMP-no counts and relative percentages are given for each component and two different versions of the sample (using pre- and post-*Gaia* kinematic input parameters).

selection bias. For a given luminosity class, metal-poor stars are brighter than their more metal-rich counterparts, meaning that we may unintentionally over-sample lower-metallicity stars relative to higher-metallicity stars when observing distant targets. CEMP-no stars tend to be more metal-poor than CEMP-s stars, so this selection bias may result in an artificially boosted CEMP-no to CEMP-s ratio in the halo. One way to combat this issue is to limit the sample to a local volume (within 4 kpc of the Sun), where metal-poor and metal-rich stars are both bright enough to be more accurately represented. However, the Solar neighborhood contains many more disk stars than halo stars, and applying this restriction cuts the Y16 sample down to an unusable size.

The primary reason for the small sample size used here, and used by Carollo et al. (2014), is the need for high-resolution spectroscopy to provide accurate estimates for the barium and europium abundances needed to sort CEMP stars into the CEMP-no and CEMP-*s* sub-classes. As mentioned in the previous chapters, Yoon et al. (2016) found that this limitation can be overcome, and CEMP-no/CEMP-*s* membership can be determined with A(C) alone (see Figure 1.3). This opens up larger, medium-resolution samples for potential analysis, including the AEGIS data-set introduced in Chapter 3.

4.2.1.2 Results: AEGIS (Medium-Resolution Spectroscopy)

An introduction to the AEGIS data-set can be found in Chapter 3; here I focus mainly on the sample's CEMP populations. AEGIS contains 1,810 total CEMP stars, but since the A(C) division between CEMP-no and CEMP-s stars varies somewhat for different stellar classes, As in Chapter 3, I limit this sample to sub-giants/giants and dwarfs/turnoff stars, for which the A(C) divisions are most readily apparent in this data-set. I use $A(\mathrm{C}) = 7.1$ and 7.6 as the dividing lines for these categories, respectively, as recommended by Yoon et al. (2018) in their analyses of the AEGIS sample. Stars with $Z_{\mathrm{max}} < 3\,\mathrm{kpc}$ and $r_{\mathrm{apo}} < 5\,\mathrm{kpc}$ are removed to reduce disk contamination. After removing unbound stars and stars with insufficient kinematic information from the sample, 982 CEMP stars (556 CEMP-s, 426 CEMP-no) remain. As with the Y16 sample, the original AEGIS kinematics were compiled prior to the release of the *Gaia* astrometric catalog. When supplemented with *Gaia* kinematics, the CEMP sample increases to 1,036 (548 CEMP-s, 488 CEMP-no). I repeat the Carollo et al. (2014) analysis on the AEGIS data-set with pre- and post-*Gaia* kinematics, as well as on a temperature-restricted and a whole-temperature sample, in order to observe the effects that kinematic uncertainties and temperature bias might have on the results for this larger sample. Unfortunately, as with the Y16 sample, there are not sufficient halo CEMP stars in the AEGIS sample to impose a locality restriction. The results of these analyses are summarized in Table 4.3.

The sample without temperature restriction shows CEMP-s stars to dominate mildly in the inner-halo and CEMP-no stars to dominate mildly in the outer-halo.

TABLE 4.3

AEGIS DUAL HALO DESIGNATIONS

		Type	I	O	T
All $T_{\rm eff}$	Original	CEMP-s	371 (60.6%)	85 (46.2%)	100 (53.8%)
		CEMP-no	241 (39.4%)	99 (53.8%)	86 (46.2%)
	Gaia DR2	CEMP-s	427 (56.2%)	53 (40.5%)	68 (46.9%)
		CEMP-no	333 (43.8%)	78 (59.5%)	77 (53.1%)
Low $T_{\rm eff}$	Original	CEMP-s	145 (53.3%)	55 (40.7%)	56 (45.9%)
		CEMP-no	127 (46.7%)	80 (59.3%)	66 (54.1%)
	Gaia DR2	CEMP-s	205 (49.9%)	33 (32.7%)	38 (38%)
		CEMP-no	206 (50.12%)	68 (67.3%)	62 (62%)

Dual halo designations for the AEGIS sample, based on the method used in Carollo et al. (2014). CEMP-s and CEMP-no counts and relative percentages are given for each component and two different versions of the sample (using pre- and post-*Gaia* kinematic input parameters), as well as for the whole-temperature and temperature-restricted ($T_{\rm eff} \leq 5,600\,$K) sub-samples.

The sample with temperature restriction shows a near-even ratio of CEMP stars in the inner-halo, and a strong dominance of CEMP-no stars in the outer-halo (similar to the ratio quoted by Carollo et al. (2014)).

The AEGIS sample's CEMP ratios did not change as drastically as those for the Y16 sample when *Gaia* kinematics were added, only changing an average ± 5.7 (all $T_{\rm eff}$) - 6.4% (cool stars) compared to ± 16 - 18% in the Y16 sample. The temperature restriction, which did not produce a significant change in the Y16 sample, seems to have at least a moderate effect on the AEGIS CEMP ratios, increasing CEMP-no percentages an average 1.5 (*Gaia*) - 6.9% (original) across the board (the AEGIS sample contains a larger fraction of >5,600 K CEMP stars than the Y16 sample, which likely explains the difference seen here). Overall the largest difference appears to have been made by increasing the sample size; although Carollo et al. (2014) performed their original analyses on a sample of similar size to the Y16 sample, this method may not be ideal for small samples. Individual kinematic uncertainties that can result in a star being sorted into the "wrong" category will most strongly affect samples with only a handful of stars per category.

4.2.2 CDF Separation Method

Here I present an alternative approach for establishing the duality of the halo, using a statistical method to compare the orbital behaviors of CEMP-no and CEMP-s populations.

I construct Cumulative Distribution Functions (CDFs) for the AEGIS sample[3] over $r_{\rm apo}$ and E, the same orbital quantities used in the Carollo et al. (2014) method to evaluate halo membership. A two-sample Kolmogorov Smirnoff (KS) test for equality of populations can then be applied to the CDFs, testing the null hypothesis that the CEMP-no and CEMP-s populations are drawn from the same parent distribution. Qualitatively, the KS-test measures the maximum distance between the two CDF curves to evaluate the probability of the null hypothesis for the data in question. Figures 4.2 and 4.3 show the CDFs and KS test results for the sample with and without temperature restriction, respectively. Note that here I show only stars with $r_{\rm apo} < 75\,{\rm kpc}$ to remove the effect of stars assigned spuriously large apocentric radii on my results. Disk contaminants are removed using the same criteria ($Z_{\rm max} > 3\,{\rm kpc}$ and $r_{\rm apo} > 5\,{\rm kpc}$) applied in the previous section.

The resulting two-sided p-values allow me to reject the null hypothesis at a $p < 0.01$ confidence level for all CDFs shown. Additionally, the CDFs visually confirm that the curves for the CEMP-s population saturate at smaller distances and lower energies

[3] This method is better suited to data-sets larger than the Y16 sample, so here I only show results for AEGIS stars.

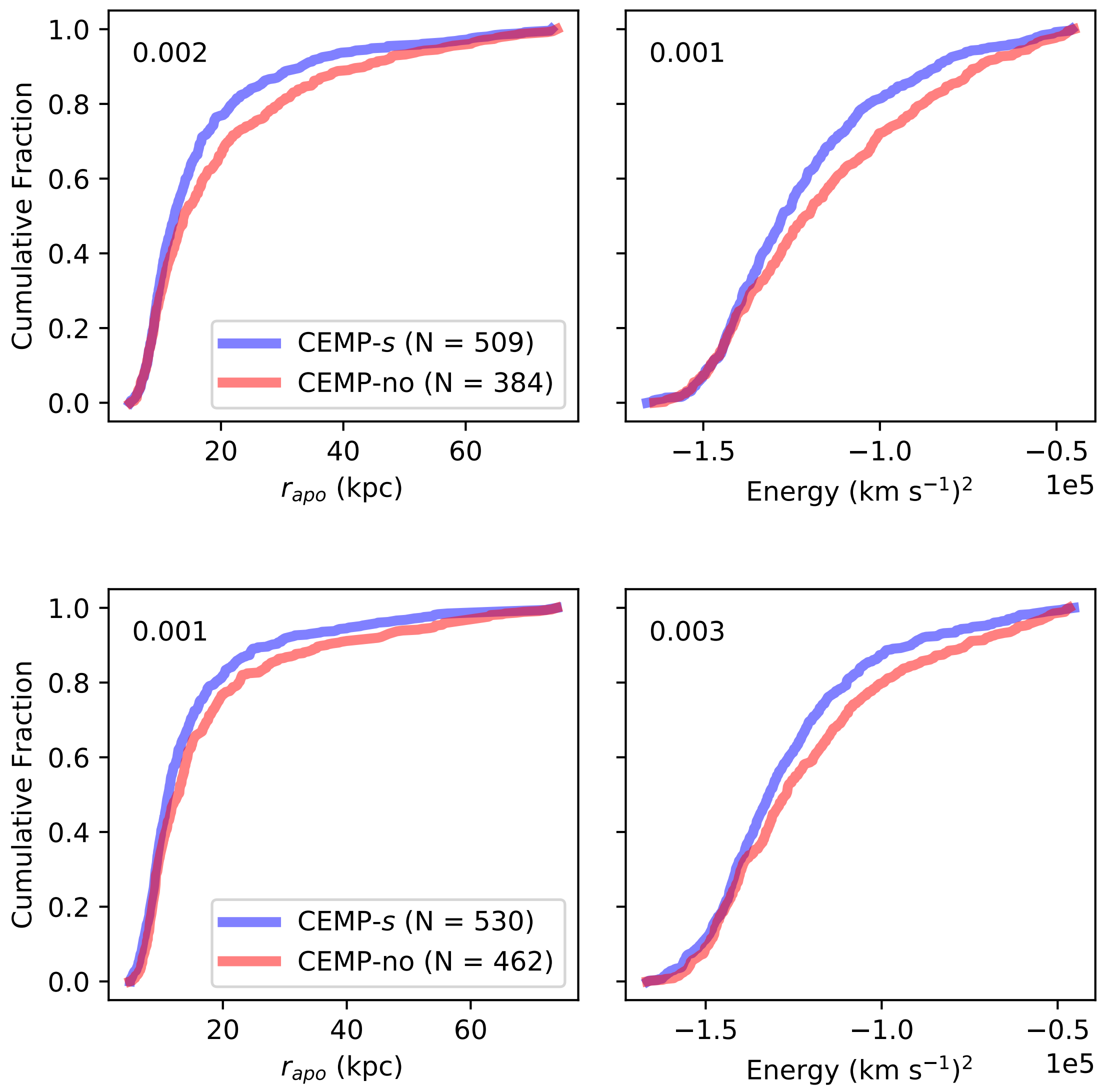

Figure 4.2. CDFs for CEMP-*s* (blue) and CEMP-no (red) stars in the AEGIS sample with original kinematics (upper panels) and *Gaia*-supplemented kinematics (lower panels), constructed over r_{apo} (left) and energy (right). A two-sample KS test for equality of populations is performed for each pair of CDFs, and the resulting (two-tailed) p-value is displayed in the upper left corner of each plot.

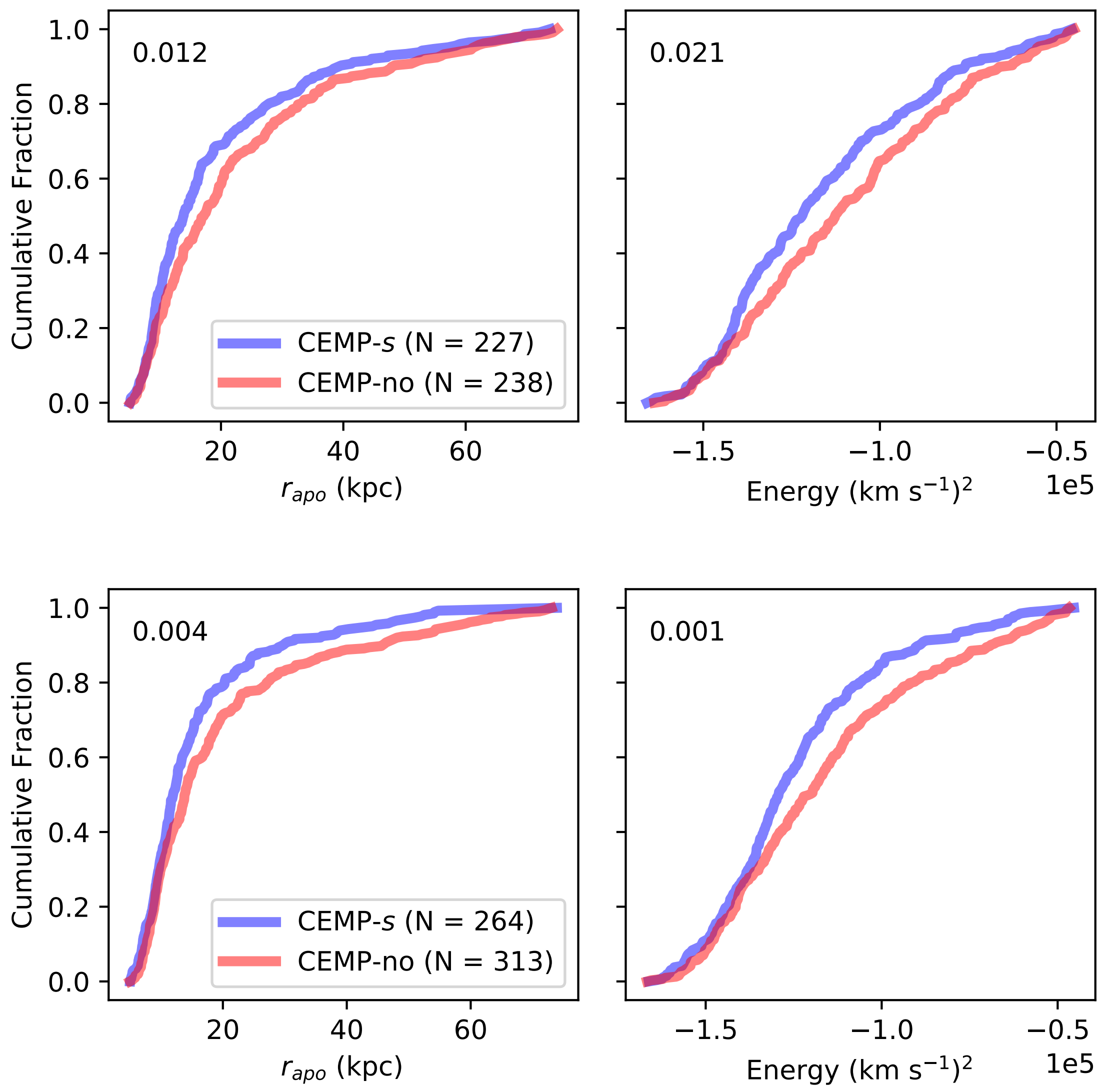

Figure 4.3. CDFs for cool ($T_{\rm eff} \leq 5,600$) CEMP-*s* (blue) and CEMP-no (red) stars in the AEGIS sample with original kinematics (upper panels) and *Gaia*-supplemented kinematics (lower panels), constructed over $r_{\rm apo}$ (left) and energy (right). A two-sample KS test for equality of populations is performed for each pair of CDFs, and the resulting (two-tailed) p-value is displayed in the upper left corner of each plot.

than the CEMP-no population. The two start to noticeably diverge at $r_{\mathrm{apo}} \sim 20\,\mathrm{kpc}$, which has previously been noted as the approximate location at which the inner- and outer-halo shift in dominance (using this particular Galactic potential). The main difference between the pre- and post-*Gaia* CDFs is a slight overall decrease in the KS test p-value, while the main difference between the non-restricted and temperature-restricted CDFs is a more noticeable divergence between the CEMP-no and CEMP-s curves.

If the Carollo et al. (2014) method adequately separates the dual halo in large data-sets like this one, is an alternative method necessary? Each procedure has its own benefits and drawbacks. The Carollo et al. (2014) method provides relative CEMP-no and CEMP-s percentages, which are useful in the reconstruction of potential halo formation scenarios and also as constraints for theoretical models. The main benefit of the CDF method is that it can be more easily applied to a variety of Galactic potentials. Figure 4.4 shows CDFs for the *Gaia*-supplemented AEGIS sample, produced using the `galpy` "Milky Way 2014" potential (Bovy, 2015). It should be noted that, unlike the CDFs in Figures 4.2 and 4.3, these CDFs include stars with positive energy values. The shallower `galpy` potential tends to designate outer-halo stars as unbound, and so may not be the best choice of potential for analyses relating to the dual halo (see Kim et al. 2019 for a comprehensive comparison between this `galpy` potential and the Stäckel potential used in this work), but these results are included here simply to illustrate an application of the this method to an alternative Galactic potential, so I rely on the $r_{\mathrm{apo}} < 75\,\mathrm{kpc}$ restriction used above to remove unbound stars. Although the results of the KS test are not as strong in this case, possibly due to the issues mentioned above, I can still reject the null hypothesis at a $p < 0.05$ confidence level for both the whole-temperature and temperature-restricted sub-samples, and there is a noticeable divergence between populations at $r_{\mathrm{apo}} \sim 20\,\mathrm{kpc}$ in the temperature-restricted sub-sample.

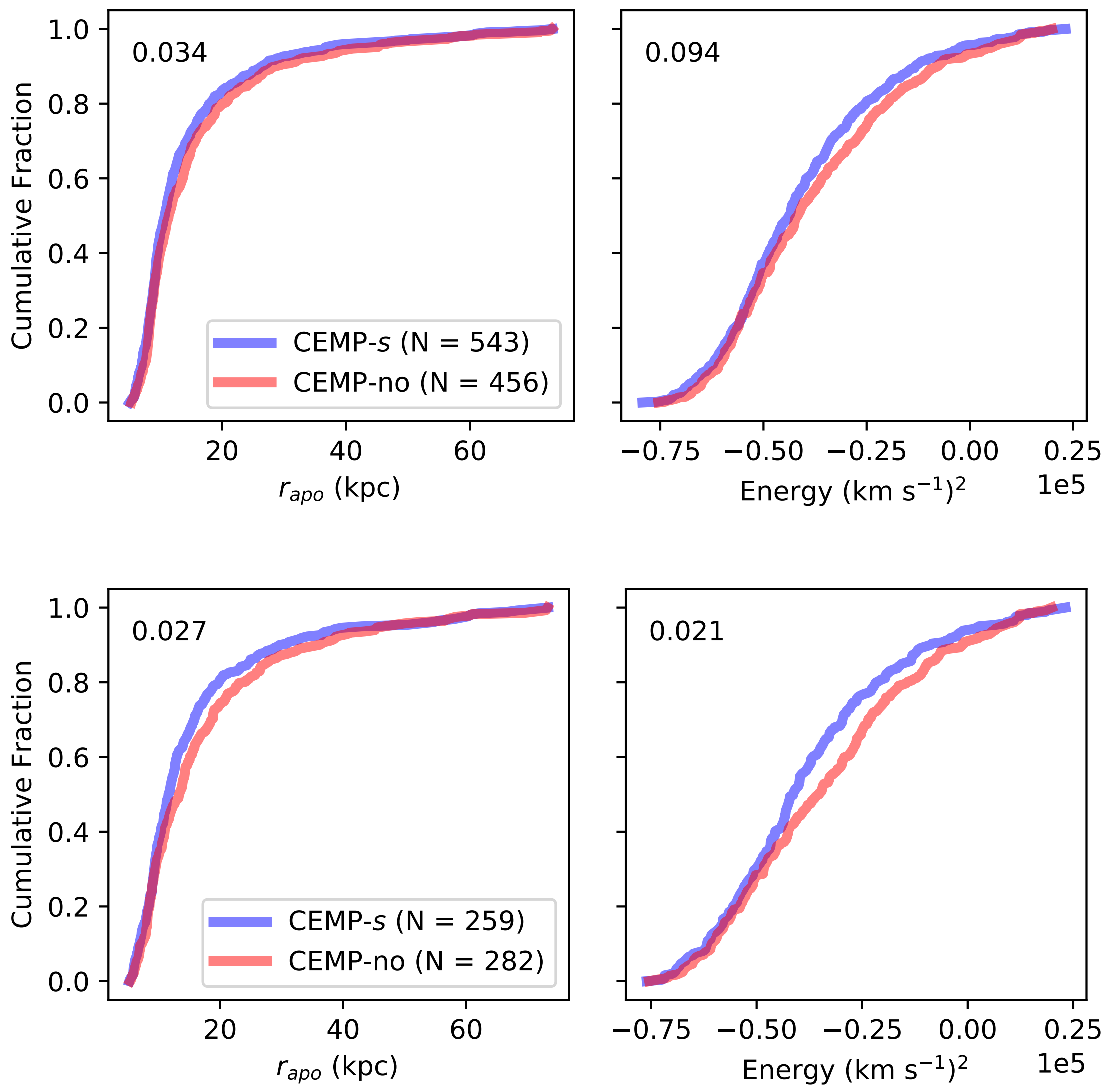

Figure 4.4. CDFs for CEMP-s (blue) and CEMP-no (red) stars in the AEGIS sample using the `galpy` "Milky Way 2014" Galactic potential, constructed over $r_{\rm apo}$ (left) and energy (right). The whole-temperature sample is shown in the upper panels and the temperature-restricted sample ($T_{\rm eff} \leq 5,600$) is shown in the lower panels. A two-sample KS test for equality of populations is performed for each pair of CDFs, and the resulting (two-tailed) p-value is displayed in the upper left corner of each plot.

4.2.3 Summary

Disentangling the overlapping properties of the halo system is not a straightforward task; higher precision data (e.g., *Gaia* DR3) and more extensive forays into the distant halo are likely necessary to more fully elucidate its origins. In particular, a larger sample of OHP CEMP stars observed in the Solar neighborhood is necessary to measure inner- and outer-halo CEMP ratios without potentially including a metallicity-distance bias, as mentioned in Sections 4.2.1.1 and 4.2.1.2. Despite the limitations of the data in hand, the distinct chemo-dynamical characteristics of the inner- and outer-halo populations can be seen in the analyses presented above, in addition to the observational and theoretical studies summarized in the introduction to Section 4.1.

It may seem unnecessary to continue to investigate methods of establishing the duality of the halo, especially using pre-*Gaia* data, considering the recent post-*Gaia* discoveries in favor of a dual halo system (see Section 4.3 below). However, establishing which approaches give consistent or inconsistent results depending on the size, quality, etc. of the data-set used is important for continued analyses of areas of the Galaxy that may not be well-represented within the *Gaia* catalog.

4.3 The Post-*Gaia* Halo

Our post-*Gaia* understanding of the Galaxy has gone through several key changes, including the discovery[4] of the remnants of a massive satellite speculated to have donated the majority of inner-halo stars. Different researchers have presented evidence for this feature using a variety of techniques: Belokurov et al. (2018) combine data for main sequence stars from *Gaia* and SDSS DR9 to identify a structure they call

[4]It should be noted that this is not the first time this feature has been noticed/this theory has been posited; Evans (2020) provides a useful overview of the findings leading up to the discovery of this major merger, including some of the works referenced in Section 4.1, and highlights some of the key differences between the proposed *Gaia*-Enceladus *Gaia* Sausage structures.

the "*Gaia* Sausage", subsequently confirmed by Myeong et al. (2019), who supplement the *Gaia* catalog with Hubble Space Telescope data to track globular clusters associated with the merger. Shortly thereafter, Helmi et al. (2018) use a cross-match between *Gaia* and data from the Apache Point Observatory Galactic Evolution Experiment (APOGEE; Majewski et al., 2017) to identify a massive feature they dub "*Gaia*-Enceladus". Although the exact characteristics of the merger debris (radial velocity, spatial extent, etc.) are not entirely agreed on by the various authors who contributed to the discovery of this progenitor, there is a general consensus that a quite massive ($M_* \sim 10^8$ to $10^9\,M_\odot$) satellite merged with the Milky Way $\sim 10\,$Gyr ago, making it one of the last major mergers experienced by our Galaxy.

The assembly history of the outer-halo has also undergone revision following *Gaia* DR2. Matsuno et al. (2019) and Myeong et al. (2019) both find evidence of a common progenitor for high-energy, retrograde halo stars (outer-halo stars). Myeong et al. (2019) dub this progenitor the "Sequoia" galaxy, assigning it an estimated stellar mass of $\sim 10^7\,M_\odot$ and approximate infall time at 9-11 Gyr.

Just as the establishment of the dual halo system was once hotly contested, there is ongoing disagreement between different camps over the makeup of these proposed progenitors, made more complicated by their intersecting properties (for example, the moderately retrograde *Gaia*-Enceladus may encompass parts of both the mildly prograde *Gaia* Sausage and the strongly retrograde Sequoia).

In the following sections I examine the characteristics of the kinematically-selected *Gaia*-Enceladus population within the AEGIS data-set. The studies listed above make use of metallicity and alpha-element abundances in their analyses, but not carbonicity. An analysis of the CEMP characteristics of the *Gaia*-Enceladus structure could be a novel contribution to our understanding of this merger/these mergers.

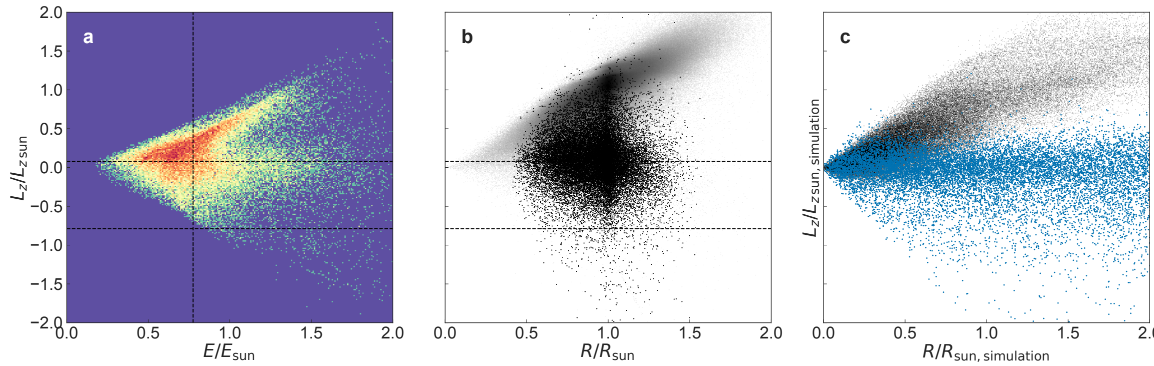

Figure 4.5. Extended Data Figure 1 from Helmi et al. (2018), caption adapted from the original text. A: Lindblad diagram for the data-set (within 5 kpc of the Sun) with $|V - V_{\mathrm{LSR}}| > 210\,\mathrm{km\,s^{-1}}$. Dashed lines indicate the criteria used to select *Gaia*-Enceladus ($-1500 < L_z < 150\,\mathrm{kpc\,km\,s^{-1}}$ and $E > -1.8 \times 10^5\,\mathrm{km^2\,s^{-2}}$). The color scale indicates logarithmic bin counts, with red corresponding to the maximum number of counts, yellow and blue to 1/6th and 1/30th of the maximum, and purple to empty bins. B: L_z versus r for the data-set (within 5 kpc of the Sun), stars from A shown as black dots. C: L_z versus r for simulated stars. Gray points correspond to the host disk, blue points correspond to the the accreted satellite.

4.3.1 *Gaia*-Enceladus

Helmi et al. (2018) select *Gaia*-Enceladus stars from a sample of high-velocity ($|V - V_{\mathrm{LSR}}| > 210\,\mathrm{km\,s^{-1}}$) stars in the Solar neighborhood (within 5 kpc of the Sun) using the criteria $-1500 < L_z < 150\,\mathrm{kpc\,km\,s^{-1}}$ and $E > -1.8 \times 10^5\,\mathrm{km^2\,s^{-2}}$, as shown in Figure 4.5.

Although the AEGIS data-set contains a large fraction of local stars, I refrain from making a <5 kpc cut due to the relatively low number of halo CEMP stars observed in the Solar neighborhood. After limiting the sample to stars satisfying $|V - V_{\mathrm{LSR}}| > 210\,\mathrm{km\,s^{-1}}$, the “plume”-like feature associated with *Gaia*-Enceladus is apparent, as can be seen in the left panel of Figure 4.6. The lower limit on energy is adjusted to $-1.4 \times 10^5\,\mathrm{km^2\,s^{-2}}$ (the difference in Galactic potentials used shifts the overall energy scale) to contain the same approximate structure highlighted in

Figure 4.5a. The MDF for the selected population is shown in the right panel of Figure 4.6. Note that the resulting distribution peaks at [Fe/H] ~ -1.6, which is consistent with the inner-halo peak given in Carollo et al. (2010) but significantly lower than the [Fe/H] ~ -1.3 peak found by Helmi et al. (2018). Confining this sub-sample to a local volume does not significantly affect the shape of the MDF, so this difference in metallicity is not caused by the metallicity-distance bias. It could stem from the sample's selection function, or indicate a systematic offset between AEGIS and APOGEE metallicity estimates.

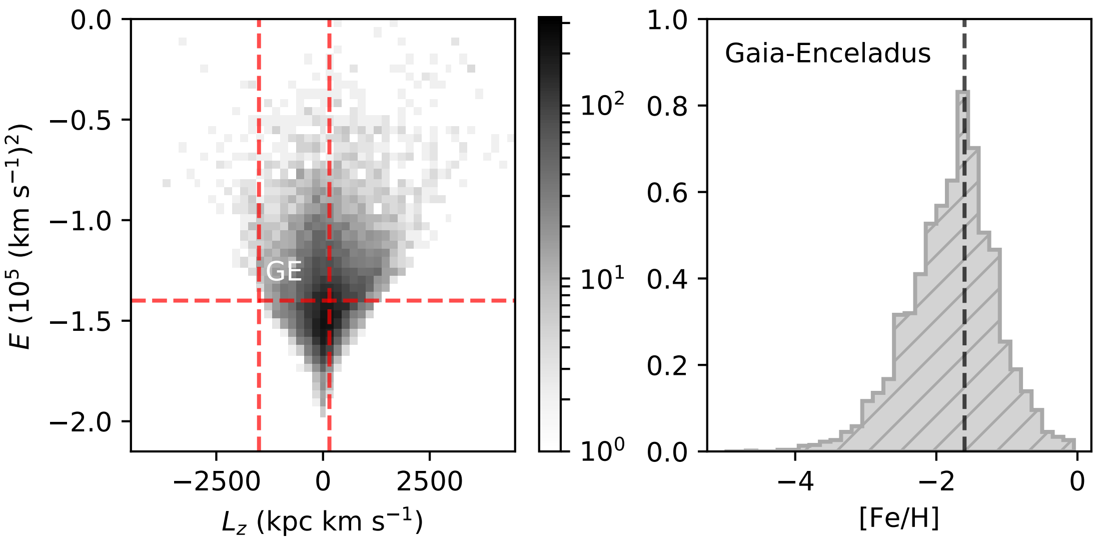

Figure 4.6. Left: A log-density Lindblad diagram for high-velocity stars ($|V - V_{\rm LSR}| > 210\,{\rm km\,s^{-1}}$) AEGIS sample. The red dashed lines indicate approximate boundaries for the *Gaia*-Enceladus feature, based on those chosen in Helmi et al. (2018). Right: The normalized MDF of the *Gaia*-Enceladus region marked in the left panel. The black dashed line indicates an approximate peak at [Fe/H]~ -1.6.

Isolating the (cool) CEMP stars within this feature (see Figure 4.7) results in a

47% CEMP-no and 53% CEMP-s contribution. This is consistent with the results found in Section 4.2, which makes sense, since the *Gaia*-Enceladus satellite is supposed to have donated the majority of inner-halo stars. This can also be visually confirmed in the lower panel of Figure 4.7, where the *Gaia*-Enceladus CEMP stars mainly populate Group I (CEMP-s/rs stars) of the Yoon-Beers (YB) diagram.

Although CEMP-s stars maintain a slight majority in this region, the presence of such a high relative ratio CEMP-no stars is significant in itself. As mentioned in Section 4.1, CEMP-s stars are thought to originate in larger, more chemically enriched mini-halos, while CEMP-no stars are thought to originate in smaller, less chemically enriched (more ancient) mini-halos. A consequence of this difference is that a CEMP-s progenitor cloud should produce significantly more CEMP-s stars by number, due to its larger mass, than a single CEMP-no progenitor cloud. We might expect the *Gaia*-Enceladus satellite, estimated at $M_* \sim 10^8$ to $10^9\ M_\odot$, to host a high ratio of CEMP-s stars. But since the ratio is nearly even, this suggests that other sources of sub-structure may be contributing to the selected area, and/or the *Gaia*-Enceladus progenitor may have a complex formation history, possibly experiencing many minor accretion events prior to merging with the Milky Way.

4.3.2 Sausage or Enceladus?

As mentioned in the introduction to Section 4.3, although *Gaia*-Enceladus and the *Gaia* Sausage share similar properties, the manner in which they are defined introduces key differences to the halo formation scenario.

The retrograde portion of the *Gaia*-Enceladus structure likely encompasses some stars associated with the Sequoia Event; although Matsuno et al. (2019) note a *Gaia*-Enceladus structure in their data, distinct from their newly-discovered Sequoia merger remnant, they appear to apply stricter L_z cuts than those used by Helmi et al. (2018), boxing in the plume feature more tightly. The boundaries and characteristics of the

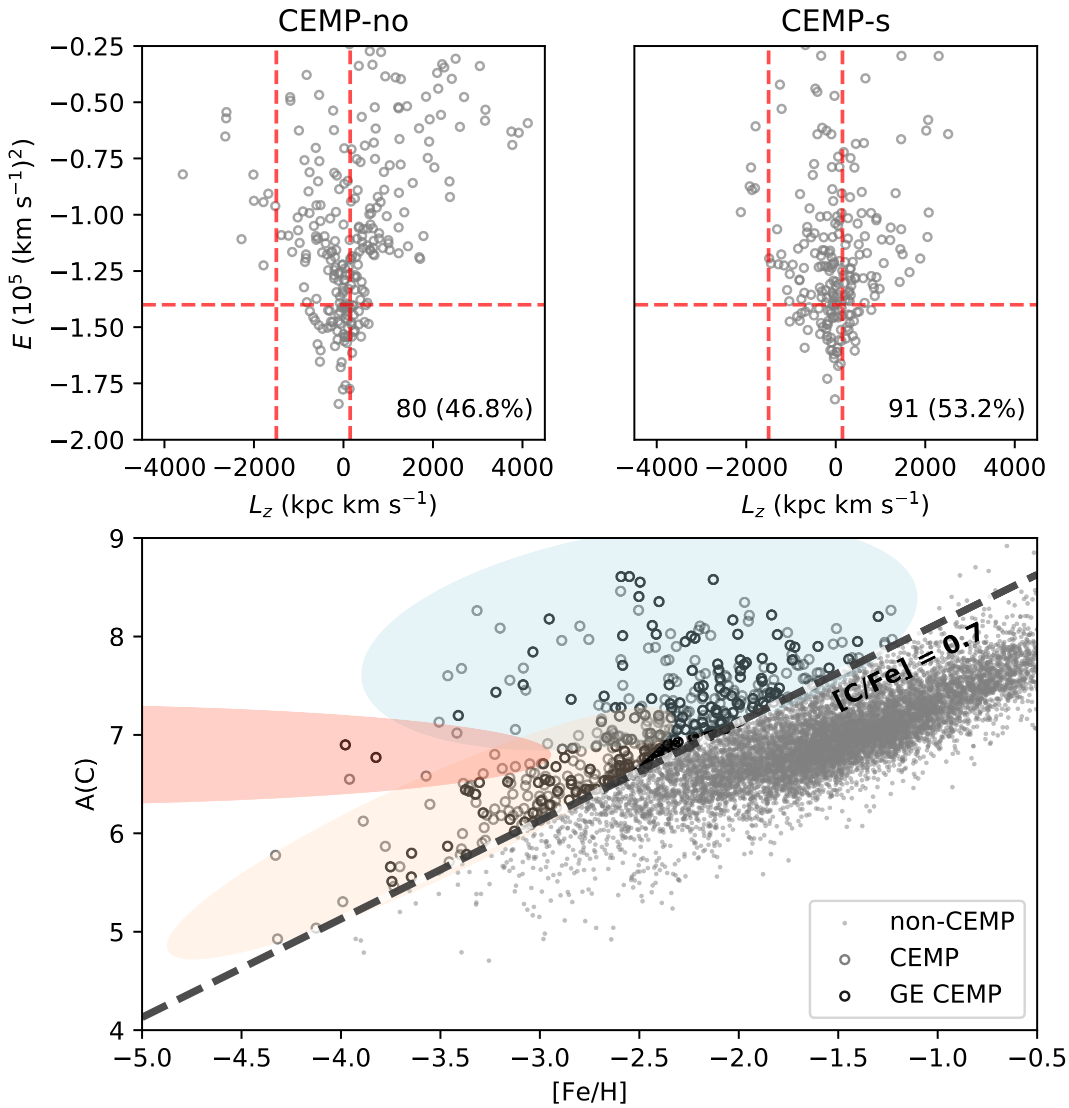

Figure 4.7. Upper panels: Lindblad diagrams for CEMP-no (left) and CEMP-*s* (right) halo stars in the AEGIS sample. Red dashed lines indicate approximate boundaries for the *Gaia*-Enceladus feature, based on those chosen in Helmi et al. (2018). The number and relative percentage of CEMP-no/*s* stars contained within the *Gaia*-Enceladus boundary is indicated in the bottom right corner of each plot. Lower panel: A Yoon-Beers (YB) diagram showing non-CEMP, CEMP, and *Gaia*-Enceladus CEMP halo stars for the AEGIS sample. The dashed line indicates the carbonicity criteria for carbon enhancement, and the blue, yellow, and red circles mark the approximate boundaries of Group I (CEMP-*s*/*rs*), Group II (CEMP-no), and Group III (CEMP-no) CEMP stars.

resulting structure may be more in line with those of the *Gaia* Sausage.

The *Gaia*-Enceladus "origin story" favors a massive merger with a retrograde trailing remnant,[5] while the Sausage plus Sequoia scenario requires two separate, large accretion events. Here I examine whether the stars within the AEGIS *Gaia*-Enceladus region are more consistent with a single population or multiple populations.

Figure 4.8 displays MDFs for this sub-sample over equal slices of L_z. Note that, particularly in the two lower panels, at least two populations with different peak metallicities appear to be present. The characteristics of the *Gaia*-Enceladus CEMP populations also appear to shift with decreasing angular momentum. As shown in Figure 4.9, the CEMP-s population seems to be more smoothly distributed over all L_z values, while the CEMP-no population displays a noted "clumpiness" below $L_z \sim -600\,\mathrm{kpc\,km\,s^{-1}}$.

The population that rises in prominence at low L_z slices in Figure 4.8 peaks around [Fe/H] ~ -2.5, which is significantly lower than the -1.6 value quoted in Matsuno et al. (2019) and Myeong et al. (2019). It should be noted, however, that the main MDF peak of the *Gaia*-Enceladus region within the AEGIS data-set was also significantly lower than that found by Helmi et al. (2018), perhaps due to a systematic offset. The [Fe/H] ~ -2.5 distribution might indicate a portion of the region comprised of small, metal-poor outer-halo "building blocks" (more on this in the chapter directly following), which could simultaneously explain the clumpiness of the CEMP-no stars noted in Figure 4.9. These could have been accreted either directly onto the outer-halo or might have been accreted onto the *Gaia*-Enceladus progenitor galaxy prior to its merger with the Milky Way. It is difficult to claim one of these scenarios as more viable than the other; it may even be that some combination of them produced the features observed in Figures 4.8 and 4.9. An expanded data-set of halo CEMP stars with high-precision kinematics will be needed for further

[5] Helmi (2020) do allow for the possibility of a smaller, "bonsai" Sequoia merger.

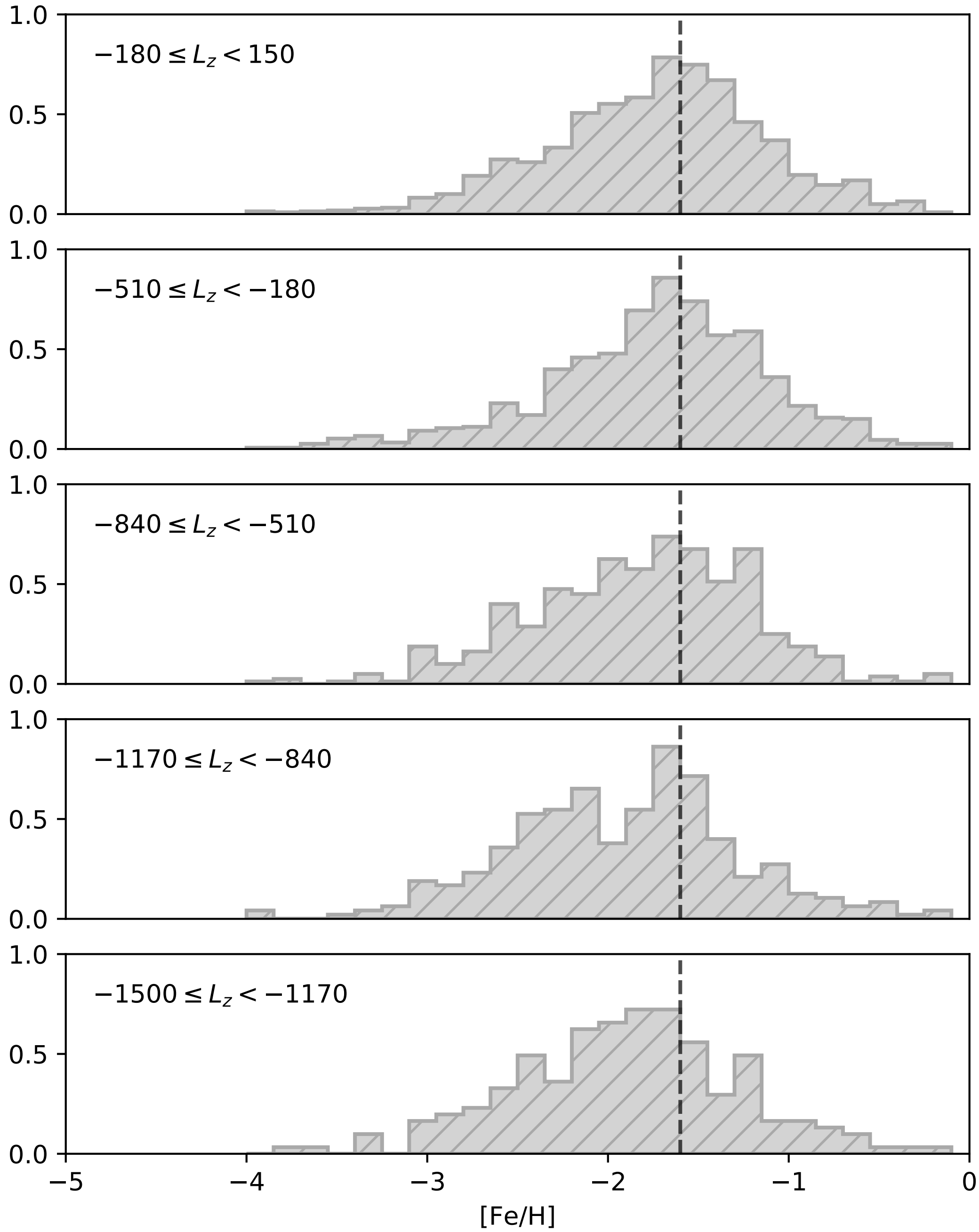

Figure 4.8. Normalized MDFs for *Gaia*-Enceladus stars in the AEGIS data-set, shown over equal slices L_z (within the bounds of the *Gaia*-Enceladus region, $-1500 < L_z < 150\,\mathrm{kpc\,km\,s^{-1}}$). The black dashed line marks the approximate peak of -1.6 noted in Figure 4.6.

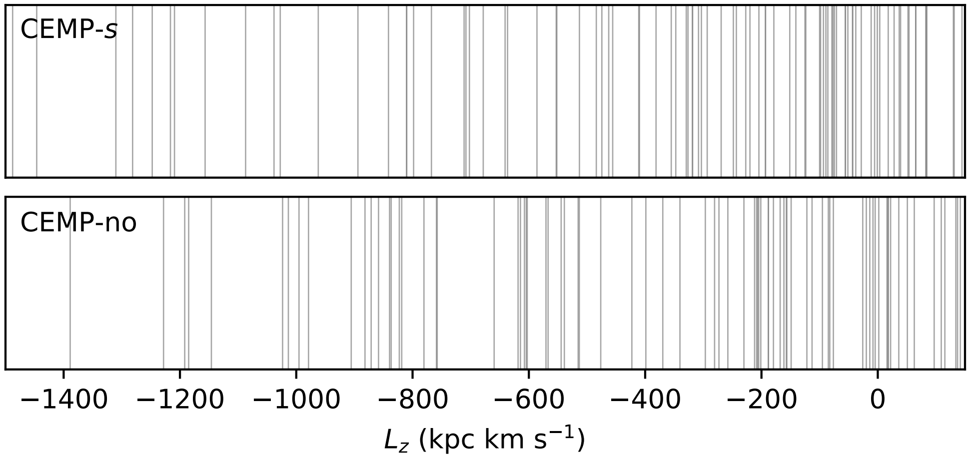

Figure 4.9. Stripe-density plots for AEGIS CEMP-s (top) and CEMP-no (bottom) stars within the *Gaia*-Enceladus structure (within the bounds of the *Gaia*-Enceladus region, $-1500 < L_z < 150\,\mathrm{kpc\,km\,s^{-1}}$).

investigation (e.g., *Gaia* DR3, perhaps).

The gradual assembly of the outer-halo through the accretion of low-mass, metal-poor galaxies requires its own dedicated study, which is presented in Chapter 5, immediately following.

CHAPTER 5

THE OUTERMOST HALO

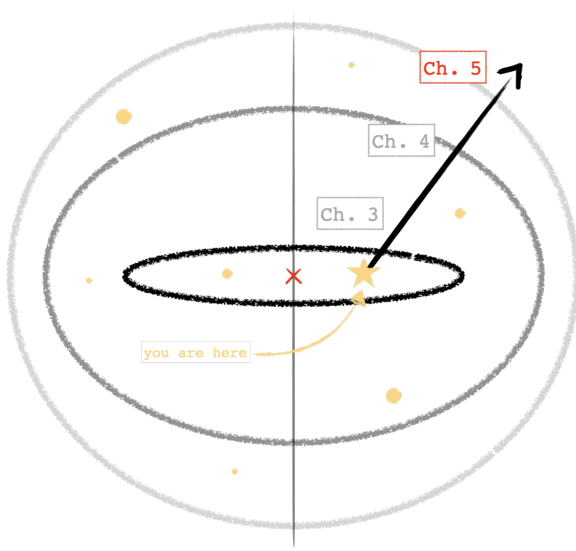

Figure 5.1. Traveling through our Galaxy: the outermost halo.

The following chapter is adapted from Dietz et al. (2020).

5.1 Metallicity Gradient

Many cosmological simulations suggest that galactic formation has a hierarchical assembly component and a complex merger history. Amorisco (2017) used a suite of merger simulations to observe the effect of satellite mass on post-merger kinematics, and found that less-massive satellites are more likely to deposit their stars farther out in their host galaxy than more-massive satellites. It follows that the outer part of the Galactic halo may have been assembled primarily from less-massive satellites that were not able to sink deeply into the Galaxy. The least-massive satellites, which are likely the most metal-poor due to truncated star formation, may remain at the outskirts of the halo, exhibiting a trend of negative metallicity gradient with distance. The existence of such a metallicity gradient is clearly suggested in the results of Starkenburg et al. (2017), who show that the fraction of the most metal-poor stars in galactic halos from the APOSTLE hydro-dynamical simulations increases with distance. There are also several theoretical studies that assert a strong relative population of very metal-poor (VMP; [Fe/H] < -2.0) stars at large distances from the Galactic center, a pattern which could support the potential presence of a metallicity gradient. For instance, Salvadori et al. (2010) used high-resolution N-body simulations of a Milky Way-analogue galaxy and a semi-analytic model to analyze the metallicity distribution function (MDF) of metal-poor halo stars, finding the relative contribution of VMP stars at distances from the Galactic center $r > 20\,\mathrm{kpc}$ to exceed 40%. Similarly, Tissera et al. (2014) used a suite of six high-resolution Milky Way-mass systems from the Aquarius simulation project to examine the transition between the inner- and outer-halo (see Section 5.2 below), and showed a 60% VMP contribution to the outer-halo population, with 60%–90% of VMP stars coming from their simulated low-mass ($< 10^9\,\mathrm{M}_\odot$)satellites.

There has also been some observational evidence presented for the existence of a negative metallicity gradient with distance. Fernández-Alvar et al. (2015) used a sample of SDSS (York et al., 2000) stars, consisting of ∼1,100 stars from the Baryon Oscillations Spectroscopic Survey (BOSS; Dawson et al. 2013) and ∼2,800 stars from the SEGUE (Yanny et al., 2009), to demonstrate a metallicity gradient with a steep slope over Galactocentric distance $r = 20$–$40\,\mathrm{kpc}$ that flattens out at greater distances. Lee et al. (2017) demonstrated a metallicity gradient in R and $|Z|$ (projected distance and height from the Galactic plane, respectively) extending up to 14 kpc with a sample of ∼105,000 main-sequence turnoff (MSTO) stars from SEGUE and BOSS. Yoon et al. (2018) provide confirmation for this trend in the Southern Hemisphere, showing metallicity gradients extending up to 25 kpc from the Galactic center with a sample of ∼70,000 stars from the AEGIS survey. In addition to highlighting structural features in their spatial metallicity maps as evidence of the complex Galactic merger history, the latter two studies also clearly show an overall negative metallicity gradient with distance.

5.2 Galactic Dual Halo Formation History

It is important to consider the effect that the stochastic merger history of the Galaxy may have on any investigations of the halo MDF—the Galactic hierarchical assembly history is complex, as evidenced by the numerous substructures discovered in the Milky Way. An overview of the dual halo formation history was given in the preceding chapter, but an abridged history is given here for convenience.

The presence of various chemo-dynamically distinct stellar populations (e.g., Belokurov et al., 2018; Carollo et al., 2007, 2019; Gilmore and Reid, 1983; Helmi et al., 2018; Matsuno et al., 2019; Myeong et al., 2018, 2019; Yoshii, 1982) and evidence of various substructures (Belokurov et al., 2007a,b; Ibata et al., 1994) have illuminated a rich and complex Galactic formation history. One important and surprising discovery was that the stellar halo comprises at least two distinct Galactic components: an inner, mildly prograde, more metal-rich ([Fe/H] ~ -1.6) component and an outer, strongly retrograde, more metal-poor ([Fe/H] ~ -2.2) component (e.g., An et al., 2013; Beers et al., 2012; Carollo et al., 2007, 2010; Chen et al., 2014; de Jong et al., 2010; Fernández-Alvar et al., 2015; Lee et al., 2017; Yoon et al., 2018).

Recent data releases of high-precision astrometric data from the *Gaia* mission (Gaia Collaboration et al., 2016, 2018) have enabled characterization of these halo populations in great detail. Several studies have asserted that the majority of inner-halo stars were imported from a single, massive $M_* \sim 10^8$–$10^9\,M_\odot$) progenitor that merged with the Milky Way ∼10 Gyr ago, known variously as the *Gaia* Sausage (Belokurov et al., 2018; Myeong et al., 2018) or *Gaia*-Enceladus (Helmi et al., 2018). A somewhat less-massive ($M_* \sim 10^7\,M_\odot$) merger, dubbed the "Sequoia Event", has also been identified as a major contributor of high-energy, retrograde, outer-halo stars (Matsuno et al., 2019; Myeong et al., 2019).

Motivated by these recent advances in our understanding of the complex Galactic assembly history, we seek to further investigate the existence of a metallicity gradient in the "outermost halo" and to consider the complex formation history of this component. While the result by Fernández-Alvar et al. (2015) shows a metallicity gradient over a larger distance range than Lee et al. (2017) and Yoon et al. (2018), the number of stars considered is rather small (∼4,000) compared to the latter studies ($\lesssim$100,000). These results could also be accounted for by the overlapping inner- and outer-halo populations, and the gradual shift in the relative dominance of these components with increasing distance from the Galactic center. More importantly, one shortcoming of the existing observational studies is the possible presence of the metallicity-distance selection bias mentioned in Chapter 4. More metal-poor giants (the dominant class in distant samples) are brighter than their more metal-rich counterparts, so one is more likely to select more metal-poor stars when observing the outer-halo region, which could artificially induce a gradient in subsequent analyses.

In this work, we suggest the presence of a negative metallicity gradient in the outer-halo's MDF over r, using non-local samples ("in-situ"). More importantly, to mitigate the metallicity-distance bias problem, we also perform our analyses with local samples (within 4 kpc of the Sun). These local samples allow us to observe a definitive metallicity gradient over apocentric distance, $r_{\rm apo}$ ("ex-situ"). We introduce our in-situ and ex-situ samples in Section 5.3 and describe our kinematic analyses of these samples in Section 5.4. In Section 5.5, we discuss our two important findings: 1) a metallicity gradient does indeed exist at large distances (>35 kpc) in the halo, particularly in the prograde direction and 2) retrograde stars appear to possess a flat metallicity-distance relation, indicating that the progenitor of the retrograde outer-halo is likely associated with the Sequoia merger event. Finally, we summarize our results and discuss potential future investigations of the outermost halo's MDF in Section 5.6.

5.3 Data

5.3.1 Non-Local "in-situ" Samples

Our in-situ samples consist of two sets of SDSS ($R \sim 2{,}000$) giants compiled by Chen et al. (2014) and Janesh et al. (2016). The Chen et al. (2014, hereafter, C14) sample comprises 15,723 RGB stars from SDSS DR9 (Ahn et al., 2012), compiled to study the thick-disk, inner-halo, and outer-halo of the Galaxy. The Janesh et al. (2016, hereafter, J16) sample is made up of 6,036 K giants from SDSS DR9, selected to study substructure in the stellar halo. Both samples cover distance ranges in excess of 100 kpc, making them good candidate data-sets for studying the outermost halo. The majority of stars in C14 and J16 do not have reliable *Gaia* parallaxes (with <20% uncertainty) available. We use the original distances derived in Chen et al. (2014) for C14, and calculate photometric distances for J16 following the method described in Beers et al. (2000). We also retain the original SDSS radial velocities (mean uncertainty $\sim 2\,\mathrm{km\,s^{-1}}$) and proper motions for both samples. Spatial distributions for these samples are included for reference in Figure 5.2. The C14 sample is highly concentrated within ~20 kpc of the Galactic center while the J16 sample is distributed

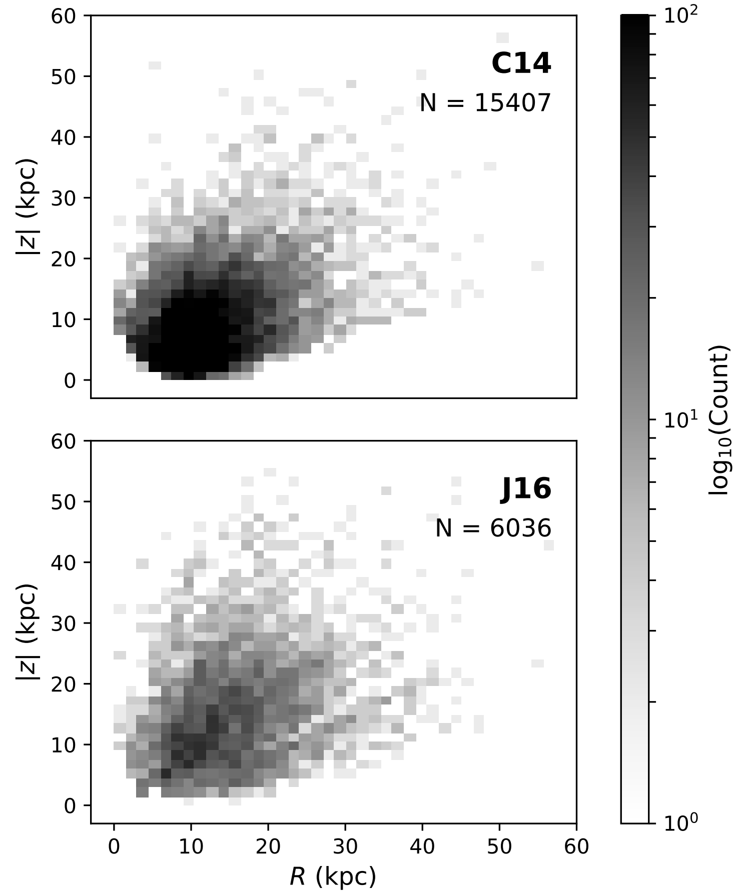

Figure 5.2. Spatial distributions of stars with valid kinematics for our two in-situ samples (C14 and J16), represented in a Galactocentric reference frame. Projected Galactocentric radius onto the Galactic plane, R, is shown on the x-axis. Vertical distance from the Galactic plane, $|z|$, is shown on the y-axis. Counts per bin are represented via a logarithmic scale. Note that some stars (<1.5% per sample) lie outside the spatial axis boundaries used in these plots.

more uniformly. Though the majority of both samples lies within $r \sim 50\,\mathrm{kpc}$, each spans a range of $>100\,\mathrm{kpc}$.

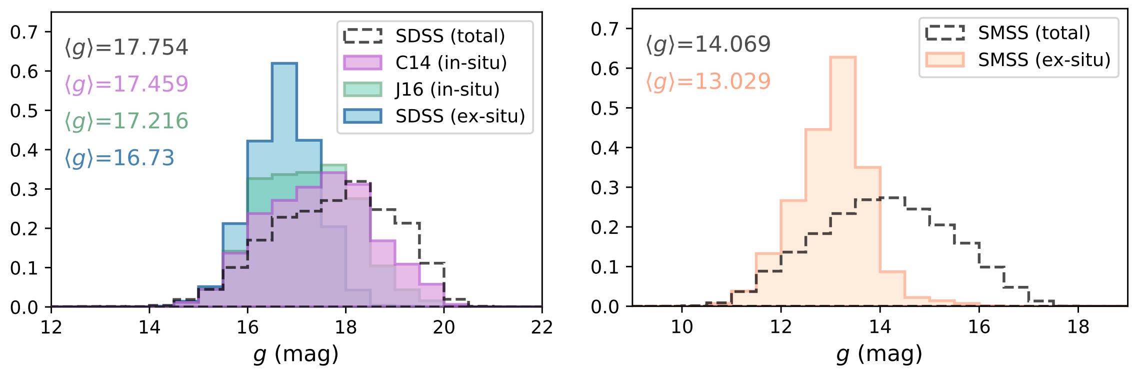

Figure 5.3. Normalized magnitude distributions in the g-band for all samples. The three SDSS data-sets (the in-situ C14 and J16 samples and the ex-situ SDSS sample) are grouped together in the left panel. The ex-situ SMSS sample is shown in the right panel. In each panel, the total sample (without cuts on location or kinematics) is shown with a dashed line for reference. Mean g-band magnitudes ($\langle g \rangle$) are noted in the upper left of each panel.

5.3.2 Local "ex-situ" Samples

The primary ex-situ sample used for our analyses is compiled from SDSS DR15 (Aguado et al., 2019a). The initial query to the SDSS catalog server[1] resulted in 357,816 stars with signal-to-noise ratios (SNR) >10 in the effective temperature range 4,500 K < $T_{\rm eff}$ < 7,000 K, where the SEGUE Stellar Parameter Pipeline (SSPP; Lee et al., 2008) is most reliable. Duplicate stars were removed by choosing the measurement with the highest SNR. Stars with spectra taken on plug-plates which were part of SEGUE cluster- or structure-targeting programs were removed prior to analyses.[2]

Proper motions and radial velocities were taken from *Gaia* DR2 (Gaia Collaboration et al., 2018) where available. When unavailable, we used the original kinematic parameters from the SDSS archive. The resulting sample contains mainly (>99%)

[1] https://skyserver.sdss.org/casjobs/

[2] See "SEGUE Target Selection" on the SDSS DR15 website for details.

Gaia proper motions and SDSS radial velocities. We adopt distances from the Bailer-Jones treatment of the *Gaia* parallaxes, and restrict the sample to stars with <20% distance uncertainty (Bailer-Jones et al., 2018). Stars with uncertainties on their radial velocities exceeding 20 $\mathrm{km\,s^{-1}}$ were removed from the sample. The resulting sample has a mean radial velocity uncertainty of $\sim 1.5\,\mathrm{km\,s^{-1}}$. We limit our sample to a local volume within 4 kpc of the Sun, leaving us with 118,037 stars.

Our complementary ex-situ sample was compiled by Huang et al. (2019) from SMSS DR1 (Wolf et al., 2018b). The authors provide metallicity estimates for 972,994 RGB stars and compile kinematic parameters where available. Proper motions and (Bailer-Jones) distances from *Gaia* DR2 are available for the majority (∼70%) of the sample. Of the 972,994 stars in this sample, 423,995 have available radial-velocity estimates, compiled by Huang et al. (2019) from a variety of catalogs, primarily *Gaia* DR2 and the Galactic Archaeology with HERMES survey (GALAH, $R \sim 28{,}000$; Buder et al. 2018). The resulting sample has a mean radial velocity uncertainty of $\sim 1\ \mathrm{km\,s^{-1}}$. After limiting the sample to a local volume, we are left with a sample of 395,144 stars for which viable kinematics can be obtained.

A comparison of the g-band magnitude distributions for all samples used in our analyses is shown for reference in Figure 5.3. We divide our samples into two plots based on survey source, as the SDSS g-band and the SMSS g-band differ from each other[3] and cover a different magnitude range.

5.4 Kinematical Analysis

Kinematic parameters are calculated following the procedure outlined in Chapter 2.

We note that we use the Stäckel potential and not `galpy's` Milky Way-like potential, `MWPotential2014`, following the recent comparison of Kim et al. (2019) between

[3] http://skymapper.anu.edu.au/filter-transformations/

the Stäckel and `galpy` potential. Kim et al. (2019) suggest that `MWPotential2014` may not be the ideal choice for studies focusing on the outer-halo because many highly energetic, predominantly retrograde (outer-halo) stars are found to be unbound when using the shallower `galpy` potential.

We estimate uncertainties on orbital values produced by the Stäckel potential via the Monte Carlo sampling method described in Section 2.3. Since our in-situ non-local samples do not utilize high-precision *Gaia* data, they have larger uncertainties on average than our ex-situ samples. We choose not to make any cuts on uncertainty for C14 and J16 because such cuts would exclude an overly large number of stars from our analyses. Our two ex-situ samples utilize *Gaia* data, so we are able to trim high-uncertainty stars from our data to minimize potentially spurious features.

The manner in which we prune high-uncertainty stars from our samples depends on the subsequent analyses we intend to perform on them. In Section 5.5.1.2 we bin stars over r_{apo} in steps of size 5 kpc each, so we choose to restrict our sample to stars with uncertainty on $r_{\mathrm{apo}} < \pm 10$ kpc. This allows us to create a low-uncertainty sample without losing too many distant halo stars due to an overly strict cutoff. To minimize contamination from disk-system stars in our local samples, we exclude stars with $r_{\mathrm{apo}} < 10$ kpc and $Z_{\mathrm{max}} < 3$ kpc, leaving us with 10,078 SDSS halo stars and 6,576 SMSS halo stars.

5.5 Results and Discussion

5.5.1 Global Metallicity Gradient

5.5.1.1 In-Situ Results

In Figure 5.4 we construct MDFs for C14 (left panels) and J16 (right panels) over increasing slices of r. The MDF of the C14 sample shifts toward the metal-poor regime and its metal-poor tail noticeably increases in relative proportion as we move

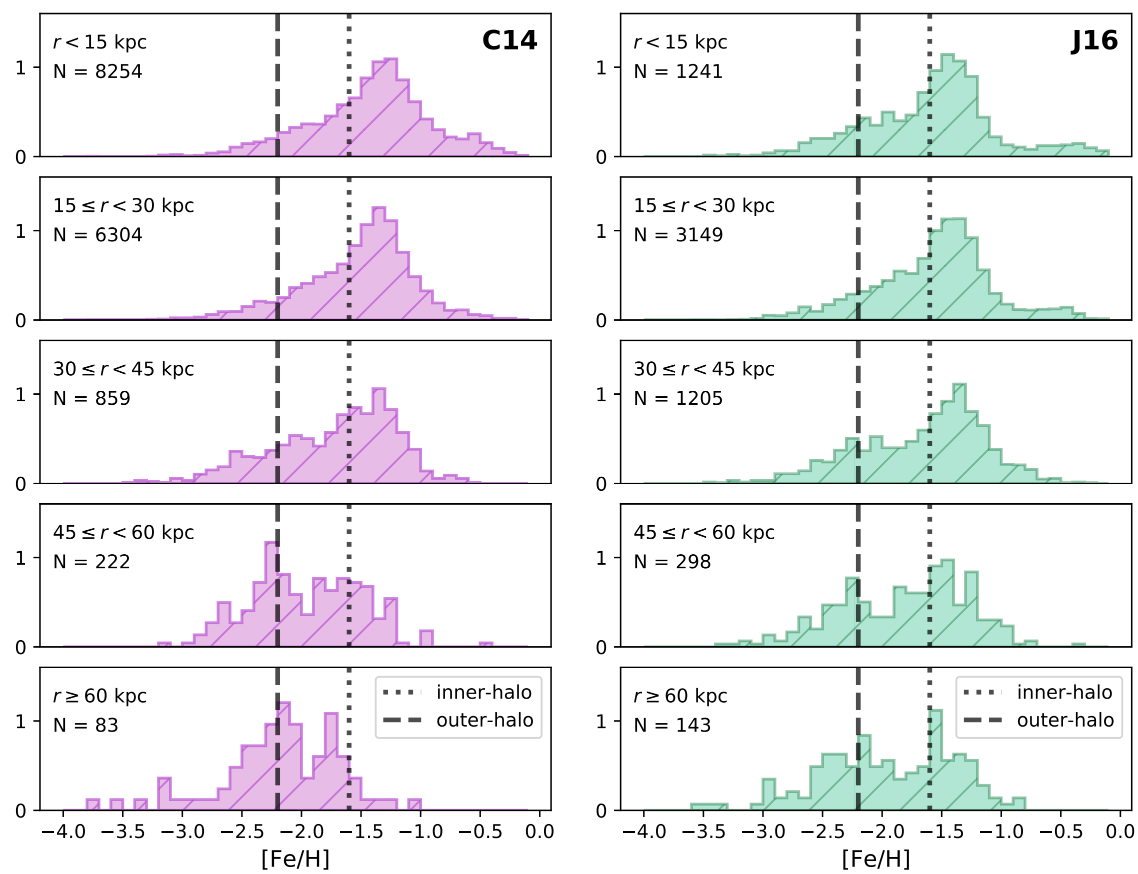

Figure 5.4. Metallicity distributions for the C14 (left column) and J16 (right column) samples over increasing slices of r. The dotted and dashed lines mark the mean metallicities of the inner-halo ([Fe/H] $= -1.6$) and outer-halo ([Fe/H] $= -2.2$), respectively, estimated by Carollo et al. (2010). Note the apparent increase in the tail strength of the MDFs at low metallicity in the lower (more distant) panels, beginning around $r >$ 30 kpc. See text for discussion.

farther from the Galactic center, particularly beyond 45 kpc. Though this effect is not as noticeable in the J16 sample as the C14 sample, likely due to the J16 selection function,[4] both clearly show that the dominant stellar component changes from the metal-richer populations of the metal-weak thick-disk (MWTD; [Fe/H] ~ -0.8 to -1.8) and inner-halo ([Fe/H] ~ -1.6) to the metal-poor outer-halo ([Fe/H] ~ -2.2) over increasing distance. We note that there exists, interestingly, a relatively strong inner-halo like population even beyond 30 kpc in both samples. This may be associated with a major merger event, and is discussed in more detail in Section 5.5.1.2.

Although our in-situ samples are likely to be affected by metallicity selection biases, here we are interested in the nature of their *lowest-metallicity* tails, with [Fe/H] < -2.0. As clearly shown by the empirical comparison of giant-branch luminosity with metallicity for Galactic globular clusters in Figure 5 of Huang et al. (2019), this dependency is minimal at the lowest abundances. Additionally, the increasingly apparent bimodality at larger distances in Figure 5.4 (also seen in Carollo et al. 2007, 2010) cannot be explained by this bias alone.

5.5.1.2 Ex-Situ Results

We conduct a similar analysis using the local ex-situ SDSS and SMSS samples to mitigate the metallicity-distance bias, based on the suggestive evidence of a possible metallicity gradient in the outermost halo from the non-local in-situ samples analyzed above.

We examine how the frequency of VMP stars and the average metallicity of our samples vary as a function of $r_{\rm apo}$, as shown in the upper and lower panels of Figure 5.5, respectively. Stars are binned in steps of size 5 kpc until fewer than 10 stars are available per bin, after which all subsequent bins are combined. We note that, because

[4] In an effort to remove foreground dwarfs from their sample, these authors trimmed stars with spectra having significantly strong MgH features. Unfortunately, this also resulted in the removal of a significant number of CEMP stars, which are among the most likely to be VMP stars.

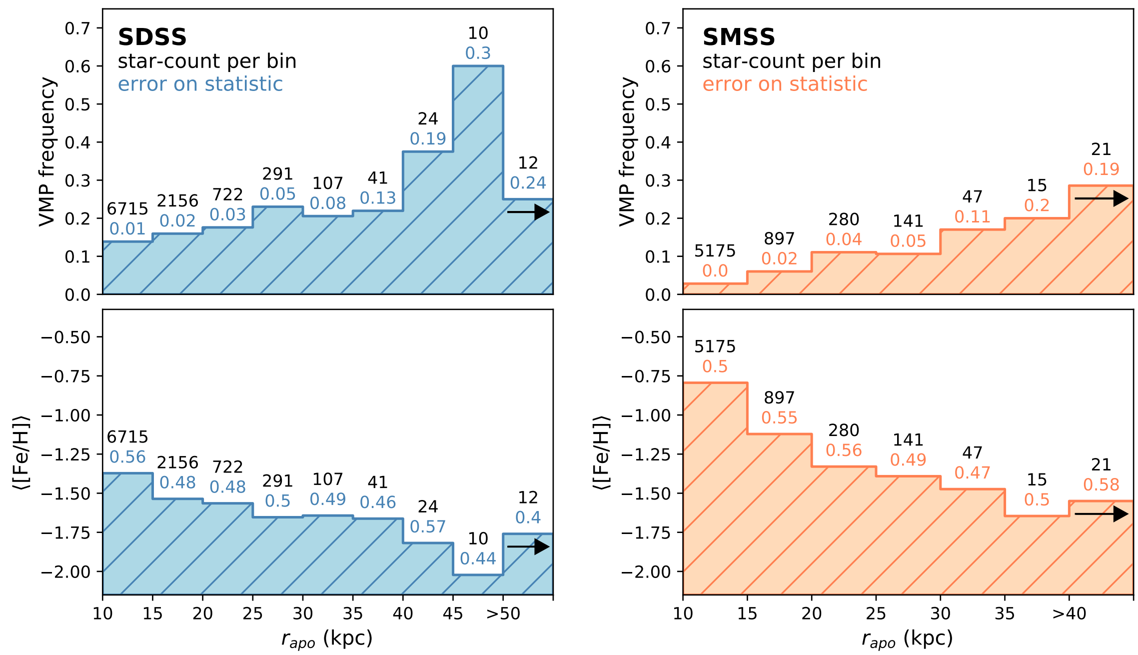

Figure 5.5. VMP frequencies (top) and average metallicities (⟨[Fe/H]⟩, bottom) for the SDSS (left) and SMSS (right) samples. In the upper panels, star counts and frequency error estimates are indicated for each bin. The frequency error is estimated with a one-sigma Wilson proportion confidence interval (Wilson, 1927). In the lower panels, star counts and the dispersion of [Fe/H] for each bin are provided.

of this binning choice, the final bin in each panel may be influenced by low-number statistics and suffer from high uncertainty.

The VMP frequency of the SDSS sample shown in the top left panel of Figure 5.5 climbs very slowly in the range $r_{\rm apo} = 10$–$40\,$kpc, after which it experiences a sharp increase, rising from $\sim$20% to $\sim$60% over the next 10 kpc. The average metallicity slowly decreases from [Fe/H] ~ -1.4 at $r_{\rm apo} = 10\,$kpc, plateauing around [Fe/H] ~ -1.6 at $r_{\rm apo} = 25$–$40\,$kpc, then dropping rapidly to [Fe/H] ~ -2.0. We note that the statistics in the largest distance bins of the left panels appear contrary to the overall trends, but have high uncertainty compared to the majority of the preceding bins.

The VMP frequency for the SMSS photometric sample experiences a steady climb over $r_{\rm apo}$, maxing out at $\sim$30%, as seen in the top-right panel of Figure 5.5. The average metallicity decreases from [Fe/H] ~ -0.8 at 10 kpc to [Fe/H] ~ -1.6 at 40 kpc. Although the changes in VMP frequency and mean metallicity are not as dramatic for the SMSS sample as for the SDSS sample, both samples display a clear metallicity gradient over $r_{\rm apo}$. The differences in the samples are likely due to the fact that the SMSS sample does not reach as far into the halo as the SDSS sample.

The steep change in mean metallicity from [Fe/H] ~ -1.6 to approximately -2.0 at $r_{\rm apo} \gtrsim 40$ kpc in the SDSS panels in Figure 5.5 could indicate a shift between the relative dominance of the inner-halo ([Fe/H] ~ -1.6) and outer-halo ([Fe/H] ~ -2.2), as discussed in Section 5.2. Another possibility is that this region of the metallicity distribution represents the shift between stars donated to the outer-halo by the Sequoia merger event, estimated at [Fe/H] ~ -1.6 (Myeong et al., 2019), and stars donated by smaller mergers of more metal-poor satellites. Accordingly, we investigate the detailed Galactic halo assembly history using these local samples in the next subsection.

5.5.2 Detailed Accretion History

5.5.2.1 Metallicity Distribution

Since the behavior of the SDSS local halo stars changes at approximately 35–40 kpc (e.g., Figure 5.5, left panels), we further investigate the reason for this behavior by constructing MDFs for "near" ($10 \leq r_{\rm apo} < 35$ kpc) and "far" ($r_{\rm apo} \geq 35$ kpc) halo samples, shown in the left panels of Figure 5.6. A similar diagram is shown for the SMSS halo stars in the right panels of Figure 5.6. The SMSS halo stars do not present the same sharp changes at 35–40 kpc (see Figure 5.5, right panels), in part because they do not probe the same distance range as the SDSS sample.

However, since the SMSS sample displayed similar general characteristics to the SDSS sample in our analyses of Figure 5.5, we chose to create additional near/far

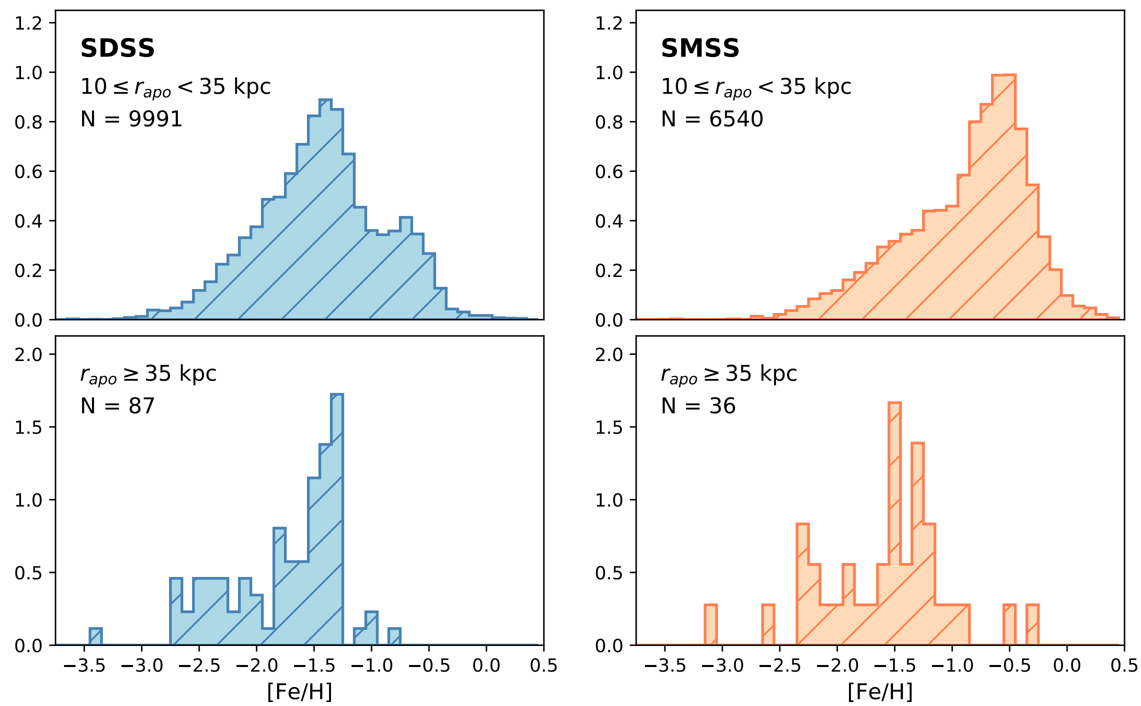

Figure 5.6: Normalized MDFs for the SDSS sample (left) and the SMSS sample (right), divided at $r_{apo} = 35\,kpc$.

MDFs from the combination of both the SDSS and SMSS samples, in order to bolster the number of stars available in the $r_{apo} \geq 35\,kpc$ range (see Figure 5.7). Gaussian distributions are fit to the combined data using the `scikit-learn` Gaussian Mixture Model (GMM) package in Python to identify components with potentially distinct origins. The near-halo combined MDF primarily consists of a distinctive component at [Fe/H] ~ -1.4, with a smaller, more metal-rich peak around -0.6, possibly belonging to a portion of the MWTD that was not completely removed by the cuts made in Section 5.4. The far-halo combined MDF also has a dominant [Fe/H] ~ -1.4 peak, as well as a more metal-poor component at [Fe/H] ~ -2.3. The near halo also possesses a small VMP population, fitted with a peak at [Fe/H] ~ -2.0, but this population rises in relative significance in the far halo.

Figure 5.7 shows that there may be at least two separate populations at $r_{apo} \geq 35\,kpc$. The more metal-rich peak ([Fe/H] ~ -1.4) seen in the far-halo (lower)

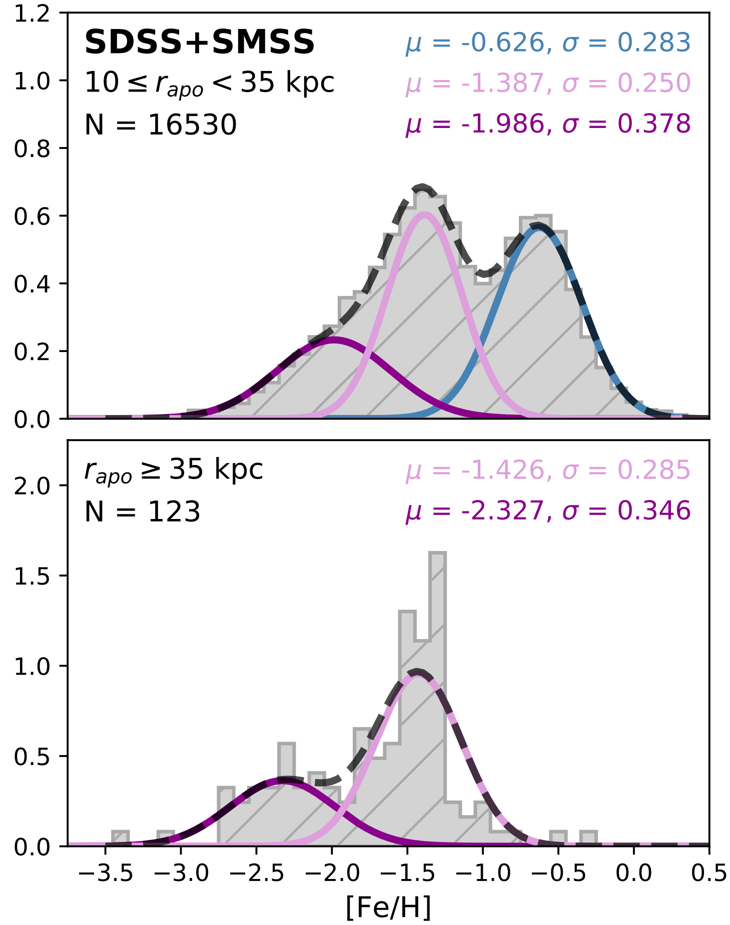

Figure 5.7. Normalized MDFs for the combined (SDSS plus SMSS) sample, divided on $r_{apo} = 35\,\mathrm{kpc}$. The color-coded curves represent Gaussian mixture-model fits of the high-r_{apo} (bottom) and low-r_{apo} (top) distributions. The dashed curves show the sum of these components.

panel of Figure 5.7 could be a selection of inner-halo population stars still present at $r_{apo} \geq 35\,\mathrm{kpc}$. The exact location of the transition zone between the inner- and outer-halo regions is uncertain. Carollo et al. (2007) place it at $\sim$ 15-20 kpc while Kim et al. (2019) give an estimate of ~30 kpc (both use the same Stäckel potential adopted in this work), so it is possible that we could still see evidence of the inner-halo population at $r_{apo} \geq 35\,\mathrm{kpc}$. Another possible interpretation is that this [Fe/H] ~ -1.4 peak comprises stars accreted from the Sequoia and *Gaia*-Sausage mergers—

this could explain the hint of bimodality seen in this component (two sub-peaks at [Fe/H] ~ -1.3 and [Fe/H] ~ -1.5)—while the more metal-poor peak represents stars accreted from a series of more minor mergers.

5.5.2.2 Prograde vs. Retrograde

We can examine these trends in more detail by dividing our local ex-situ samples on rotational velocity (v_ϕ) into prograde and retrograde components, as shown top two rows and bottom two rows of Figure 5.8, respectively. There are 6,941 prograde stars and 3,137 retrograde stars in the SDSS sample, and 5,267 prograde stars and 1,307 retrograde stars in the SMSS sample.

The prograde SDSS sub-sample (Figure 5.8, upper-left panels) experiences a slow climb in VMP frequency up until $r_{\rm apo} \sim 35\,{\rm kpc}$, after which the fraction of VMP stars climbs to ∼50%. Its average metallicity exhibits a steady decrease from 10 kpc to 45 kpc. The retrograde sub-sample (Figure 5.8, lower-left panels) exhibits no discernible relationship between VMP frequency and $r_{\rm apo}$ in the 10–45 kpc range, and its average metallicity hovers around -1.6 in the same range. Once more, the contrary behavior of the final bins of these sub-samples may be due to low-number statistics (high uncertainty).

The prograde and retrograde SMSS sub-samples (Figure 5.8, upper- and lower-right panels, respectively) exhibit largely the same behavior as the SDSS sub-samples. The prograde stars show a strong dependence on $r_{\rm apo}$ for both VMP frequency and mean metallicity, while the same quantities for retrograde stars show no noticeable dependence on distance. The *Gaia* Sausage ([Fe/H] ~ -1.3, $L_z \sim 0\,{\rm kpc\,km\ s^{-1}}$) (Belokurov et al., 2018; Myeong et al., 2018) dominates the retrograde (and prograde) signal in the near halo and the Sequoia progenitor galaxy ([Fe/H] ~ -1.6, $L_z \sim -2000$ to $-3,000\,{\rm kpc\,km\ s^{-1}}$ (Matsuno et al., 2019; Myeong et al., 2019)) likely donated the majority of the retrograde stars in the far halo. The similar peak metallicities and

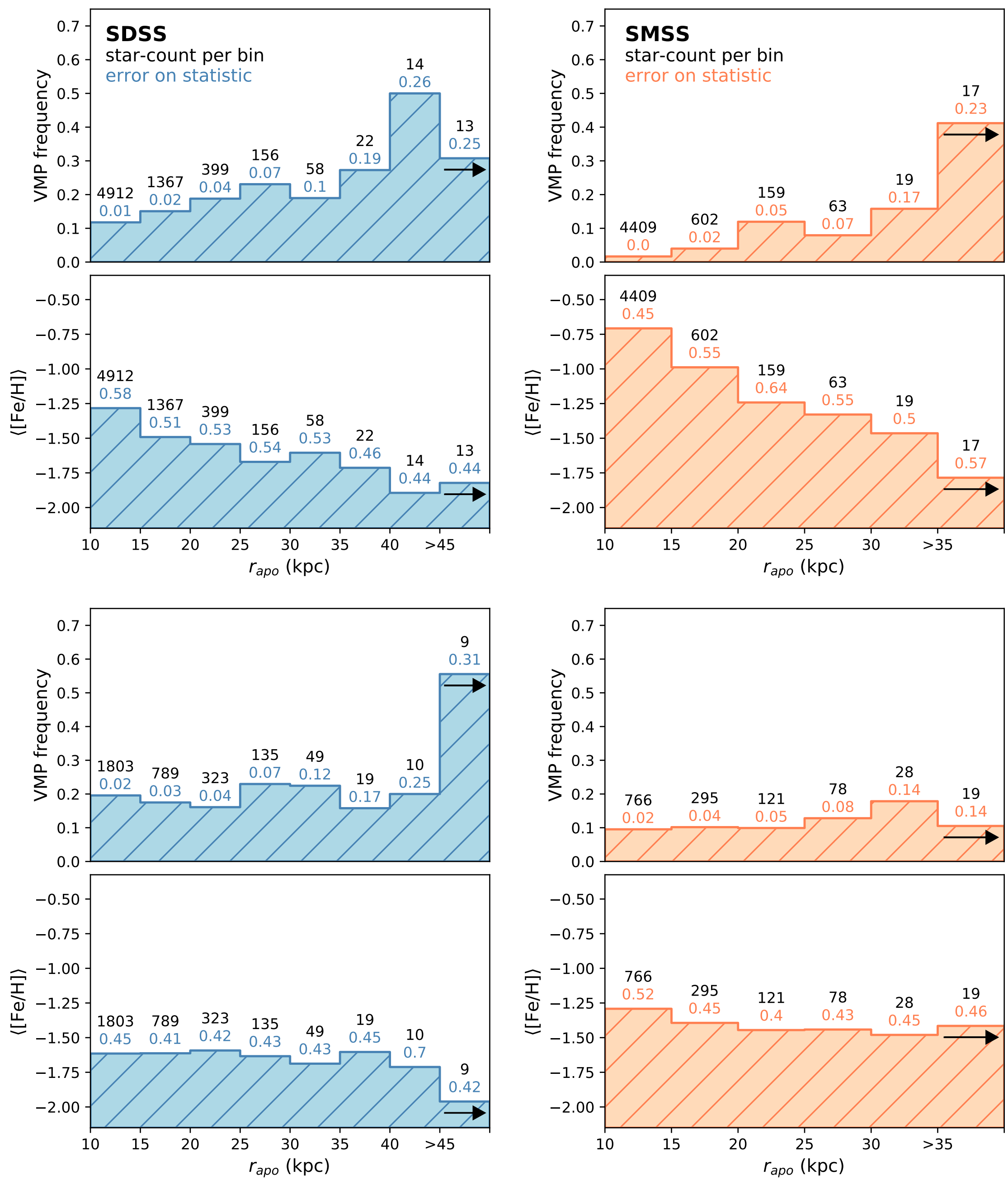

Figure 5.8. VMP frequencies and average metallicities (⟨[Fe/H]⟩) for the SDSS (left) and SMSS (right) samples, divided into (top) prograde and (bottom) retrograde components. In the VMP frequency panels, star counts and frequency error estimates are indicated for each bin. The error is estimated with a one-sigma Wilson proportion confidence interval (Wilson, 1927). In the mean metallicity panels, star counts and the dispersion of [Fe/H] for each bin are provided.

overlapping metallicity ranges (see Figure 2 in Matsuno et al. 2019 and Figure 9 in Myeong et al. 2019) of these imported populations could result in this overall metallicity plateau.

While the Sequoia ($M_* \sim 10^7\,M_\odot$) event may have imprinted a bulk retrograde signal onto the outer-halo, stars donated by numerous small accretion events likely contributed both prograde and retrograde stars to the outer-halo. However, it is likely more difficult to detect (low-metallicity) stars from small mergers in the retrograde outer-halo due to the overwhelming presence of Sequoia stars. In contrast, numerous minor accretions could be the predominant contributors to the prograde outer-halo, based on the metallicity gradient and strongly increasing VMP fraction seen in Figure 5.8. If this behavior accurately reflects the assembly history of the outermost halo, observational efforts to compile catalogs of the most ancient, most metal-poor stars may have more success targeting candidates in the prograde rather than the retrograde outermost halo.

5.6 Summary and Conclusions

We compiled a set of in-situ (∼21,700 stars in total) and ex-situ (∼16,500 stars in total) samples to confirm the presence of a metallicity gradient in the outermost halo of our Galaxy and explore the complex assembly history of the Galactic halo. The results of the in-situ analyses are suggestive regardless of the metallicity-distance selection bias. In our ex-situ analyses, we find clear evidence of both a negative metallicity gradient over $r_{\rm apo}$ and an increasing relative fraction of VMP stars with distance. In particular, the local SDSS sample exhibits a VMP frequency that reaches ∼60% at 50 kpc, commensurate with theoretical studies (i.e., Tissera et al., 2014).

When splitting our samples into prograde and retrograde components, we find that the retrograde appears to exhibit no metallicity-distance correlation while the prograde experiences a steady decline in [Fe/H] and a strong increase in VMP frequency with distance. This may be due to the influence of a more massive merger (metal-richer satellite) in the retrograde direction, versus numerous minor accretions (metal-poorer counterparts) in the prograde direction. As a result, the prograde outermost halo may be the best place to search for the most metal-poor stars.

Since we have placed tight constraints on uncertainty, we may have excluded some stars in the outer-halo that could have given our analysis more significance, but we are also not as likely to detect completely spurious features even at large distances. In addition, our local, ex-situ samples are not susceptible to the metallicity-distance bias that may affect our non-local, in-situ results.

We note here that, recently, Conroy et al. (2019b) published an exploration of the Galactic halo using a sample of some ∼4,200 giants from the H3 Spectroscopic Survey (Conroy et al., 2019a), and claimed that no metallicity gradient is detectable in their sample. However, the results of their analyses are not dissimilar from our own findings. Although they find a flat metallicity relation across the majority of the halo, they admit possible evidence for a decreasing mean metallicity beyond $r \sim 50\,\mathrm{kpc}$, which may coincide with the behavior in the $r_{\mathrm{apo}} \geq 35\,\mathrm{kpc}$ region examined in this work. The VMP component they identify as potentially originating from multiple distinct populations parallels our own hypothesis of a halo component at [Fe/H] < -2.0 consisting of numerous accretions of small mini-halos.

Have we fully explored a volume that could qualify as a comprehensive "outermost" halo, up to the outskirts of the Galaxy? The exact bounds of the outer-halo population are not yet known, and though this work shows the potential for a signature that may extend beyond the volume explored here, further efforts are required to quantify the behavior of the outer-halo MDF beyond 50 kpc. For example, improved kinematics from *Gaia* DR3 will allow us to expand the narrow magnitude ranges probed by our ex-situ samples (see Figure 5.3). Near-future observations with the Large Synoptic Survey Telescope (LSST; Ivezić et al., 2019), combined with spectroscopic follow-up, as well as large spectroscopic surveys undertaken with the Dark Energy Spectroscopic Instrument (DESI; DESI Collaboration et al., 2016), the WHT Enhanced Area Velocity Explorer (WEAVE; Dalton et al., 2014), and the 4-metre Multi-Object Spectroscopic Telescope (4MOST; Helmi et al., 2019), will enable a more thorough exploration of the distant halo and the significance of its metallicity gradient. Further analyses of the VMP catalogs from the LAMOST (Zhao et al., 2012) survey (e.g., the DR3 VMP catalog of Li et al. 2018[5]), should prove illuminating as well.

It would be of particular interest to examine the prograde/retrograde metallicity distributions with a sample of distant CEMP stars, as their nucleosynthetic subclasses can provide even more information about the origins of various stellar populations. As mentioned in the preceding chapters, CEMP-*s* stars are thought to originate in more-massive galaxies, while CEMP-no stars are thought to originate in less-massive galaxies (e.g., Lee et al., 2017; Yoon et al., 2018, 2019). A comparison of the CEMP-*s* to CEMP-no ratios in the prograde and retrograde outermost halo could help clarify the origins of the populations present there.

[5]See the "cleaned" version of this catalog in Yuan et al. (2020), as well as the substantially larger DR5 VMP catalog, in preparation.

CHAPTER 6

IN CONCLUSION

This document contains the highlights of my recent work as a "Galactic archaeologist" to contribute to the characterization of the Milky Way Galaxy through chemical and kinematic analyses of star populations. In the preceding chapters I presented investigations into populations of metal-poor and CEMP stars within the disk and halo systems of our Galaxy, and the implications of my findings with regards to the assembly history of these components. Below, I provide a brief summary of the key findings laid out in each chapter, along with the most impactful figure from each section.

In Chapter 3 I presented a phenomenological study of CEMP populations within the AEGIS data-set. I identified two CEMP populations of interest within the disk region (see Figure 6.1): a mildly prograde population ("A") and a strongly prograde population ("B"). Contrary to our previous expectations for the (relatively) metal-rich disk region, several recent studies, such as those by Beers et al. (2017), Sestito et al. (2019), and Sestito et al. (2020), have identified CEMP, UMP, and VMP populations with disk-like kinematics, with interesting implications for the assembly history of the disk system. I show that populations A and B are moderately to strongly dominated by CEMP-*s* stars, suggesting a more massive and gas-rich progenitor environment. The characteristics of population B indicate it is likely associated with the MWTD, bolstering the argument in favor of a separate (from the canonical thick-disk) MWTD component. Population A could have been formed through in-situ or ex-situ formation pathways; further sampling may be required to more fully elucidate its origins. In particular, expanded samples including 1) more low-temperature

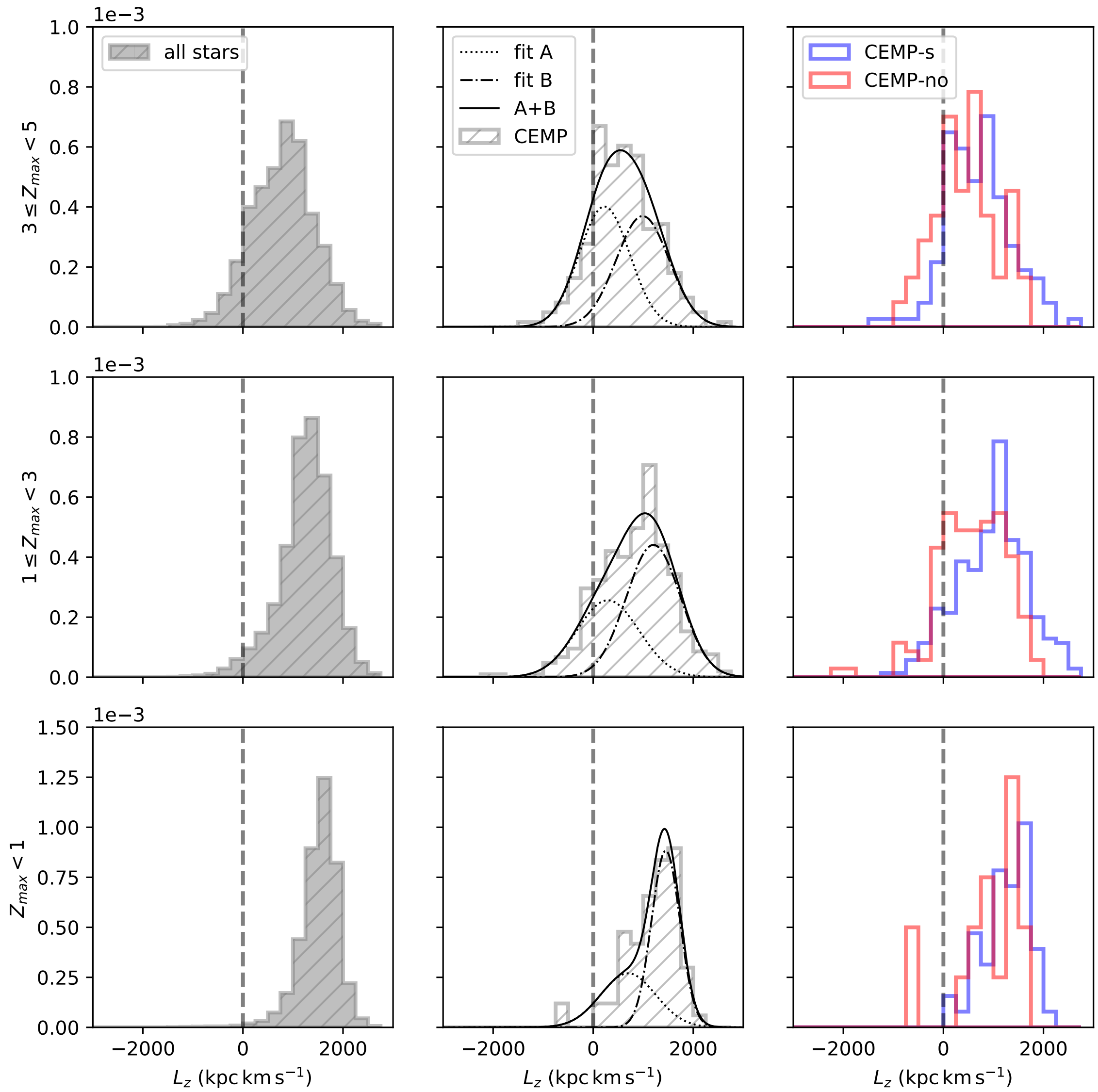

Figure 6.1. Key figure from Chapter 3: angular momentum distributions for the AEGIS sample over three different ranges of $Z_{\max}$. The left column of panels shows all stars with valid kinematics, the middle column shows the subset of CEMP stars, and the right column shows the CEMP subset divided into CEMP-s (blue) and CEMP-no (red) distributions. A dashed line marks $L_z = 0\,\mathrm{kpc\,km\,s^{-1}}$ for reference in each plot.

CEMP stars within the disk region, and 2) more Group III CEMP-no stars, will be useful in constraining the characteristics of these two populations.

Chapter 4 introduced the dual stellar halo, and the complicated task of disentangling the overlapping inner- and outer-halo components. I contrasted two methods, the sorting process employed in Carollo et al. (2014) and a CDF-based method, for verifying the duality of the halo using CEMP-no and CEMP-*s* stars. My analyses included both "pre-*Gaia*" and "post-*Gaia*" kinematics. Although the duality of the halo has become more certain following *Gaia* DR2, which has highlighted the individual accretion events that contributed to the halo system, this inner-/outer-halo dichotomy was still a somewhat contentious topic as little as two or three years ago. It is therefore important to determine which analytical tools produce sound results both with and without *Gaia* data, in order to confidently investigate areas of the Galaxy lacking high-precision kinematic data. Neither method is ideal for small sample sizes; fortunately the results of Yoon et al. (2016) have made it possible to greatly increase the numbers of CEMP-no and CEMP-*s* stars available for analysis. When applied to an expanded sample size, the Carollo et al. (2014) method can provide useful estimates of CEMP-no and CEMP-*s* relative percentages consistent with previous studies of the halo system. The main draw of the CDF-based method is that it is easy to apply to a variety of kinematic parameters, even those calculated using different Galactic potentials, without any kind of recalibration.

A re-analysis of halo stars in the AEGIS data-set in light of key discoveries made in the wake of *Gaia* DR2 shows evidence for multiple possible progenitors within the *Gaia*-Enceladus region highlighted by Helmi et al. (2018). There is still ongoing debate within the scientific community as to which accretion event—or which combination of accretion events—built the Galactic halo (*Gaia*-Enceladus, the *Gaia* Sausage, Sequoia, etc.). We may have to wait as researchers continue to refine their models, perhaps with improved data-sets from *Gaia* DR3, to re-examine the data

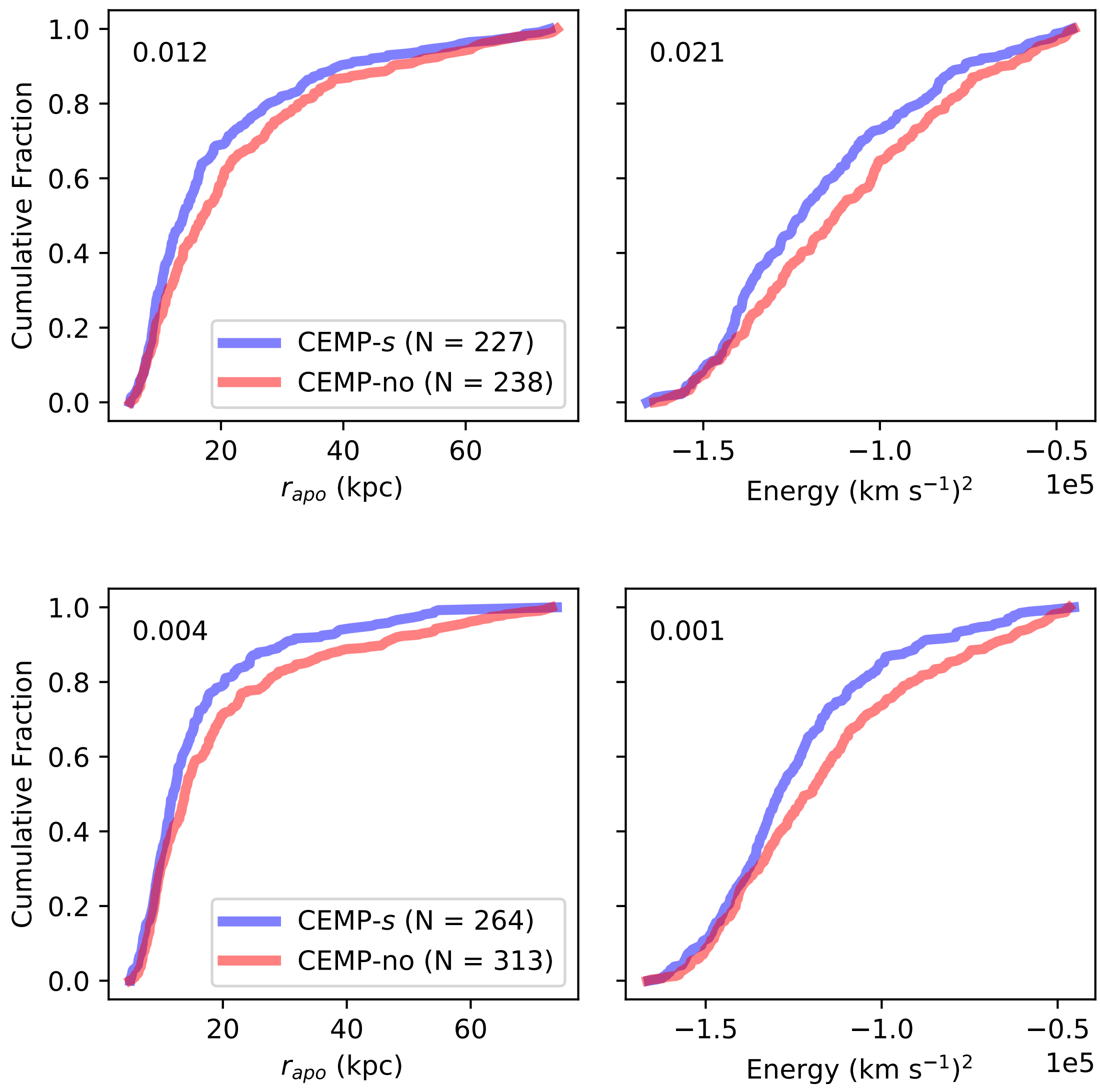

Figure 6.2. Key figure from Chapter 4: CDFs for cool ($T_{\rm eff} \leq 5,600$) CEMP-*s* (blue) and CEMP-no (red) stars in the AEGIS sample with original kinematics (upper panels) and *Gaia*-supplemented kinematics (lower panels), constructed over $r_{\rm apo}$ (left) and energy (right). A two-sample KS test for equality of populations is performed for each pair of CDFs, and the resulting (two-tailed) p-value is displayed in the upper left corner of each plot.

with a clearer understanding of the various structures involved.

The penultimate chapter of this document stops at the outskirts of the Galaxy, the so-called "outermost halo". Chapter 5 uses local (within 4 kpc of the Sun) data-sets from SDSS and SMSS to search for a metallicity gradient within the outer-halo. This search is motivated by the idea that the outer-halo was built through the gradual accretion of low-mass, low-metallicity "building blocks", like the ancient UFDs neighboring our Galaxy. More massive (metal-rich) building blocks would deposit their stars more deeply into the potential well of our Galaxy, while less-massive (metal-poor) building blocks would remain at its outskirts, inducing an observable metallicity gradient. The data-sets do indeed show a negative metallicity gradient with distance, as well as an increasing VMP frequency with distance, but only in the prograde sub-samples (see Figure 6.3). This is not so surprising in light of the recent discovery of the retrograde Sequoia merger (Matsuno et al., 2019; Myeong et al., 2019). The gradual build-up that creates the gradient signature is masked in the retrograde by a single massive accretion event, producing a rather flat metallicity-distance relation. These results suggest we might do well to target the prograde outermost halo in future searches for ancient Pop. II candidates. Additional efforts to survey CEMP stars in the distant halo could supplement our understanding of a prograde, "minorly accreted outer-halo" versus a retrograde, "majorly accreted outer-halo". CEMP-no stars are thought to originate in smaller progenitors (like the aforementioned UFDs) while CEMP-*s* stars are thought to originate in larger progenitors (including the Sequoia galaxy); an examination of their relative ratios in the prograde and retrograde outermost halo could prove enlightening.

The near future may give rise to a variety of new fundamental discoveries in Galactic archaeology via the extensions of existing surveys and the launch of ambitious new projects. To name a few: *Gaia* DR3 promises an improved astrometric catalog

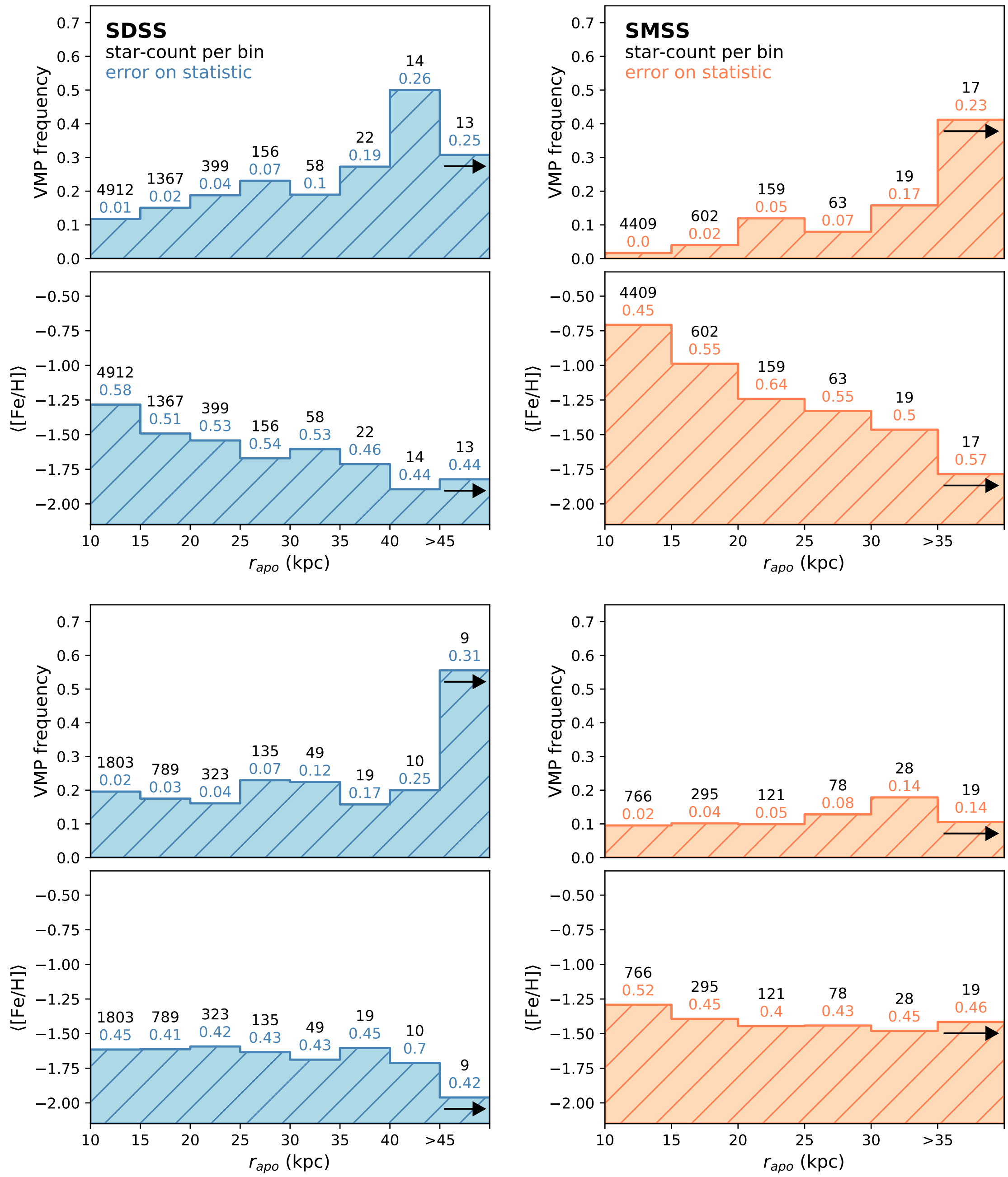

Figure 6.3. Key figure from Chapter 5: VMP frequencies and average metallicities (⟨[Fe/H]⟩) for the SDSS (left) and SMSS (right) samples, divided into (top) prograde and (bottom) retrograde components. In the VMP frequency panels, star counts and frequency error estimates are indicated for each bin. The error is estimated with a one-sigma Wilson proportion confidence interval (Wilson, 1927). In the mean metallicity panels, star counts and the dispersion of [Fe/H] for each bin are provided.

with an expanded array of parameters within the next few years; additional VMP data releases are expected from the LAMOST survey; spectroscopic catalogs from WEAVE and 4MOST will complement the *Gaia* data releases to produce advanced chemo-dynamical maps of the Galaxy. Perhaps most exciting, the upcoming launch of the James Webb Space Telescope may offer the first opportunity to directly observe a first-generation star, if the right conditions are present (i.e., gravitational lensing of a massive Pop. III star).

Some of the unresolved topics, or partially-answered questions, in Galactic archaeology that may be addressed in the coming years through the data releases mentioned above include: the composition of the halo with respect to the *Gaia* DR2 proposed progenitors (*Gaia*-Enceladus, etc.), the physical processes driving the Group II versus Group III CEMP-no morphology, the origins of the recently-identified CEMP, VMP, and UMP populations in the disk system, and the progenitors responsible for producing CEMP stars and their various sub-classes.

I hope that the analyses contained within this document have proved both informative and interesting, and thank the reader for their careful consideration of its contents.

APPENDIX A

CODES AND DERIVATIONS

A.1 Additional Derivations

A.1.1 Metric Coefficients (P, Q, R)

Here I derive the metric coefficients P, Q, and R for the oblate spheroidal coordinate system used to construct the Stäckel potential applied in this work (see Chapter 2, Section 2.3).

The coordinate Φ is the same Φ used in cylindrical coordinate systems, which has a metric coefficient R. By definition, $P = |\frac{\partial \mathbf{r}}{\partial \lambda}|$ and $Q = |\frac{\partial \mathbf{r}}{\partial \nu}|$. It may be simplest to write $\mathbf{r}$ in terms of cylindrical coordinates first, as $\mathbf{r} = R\hat{\mathbf{R}} + z\hat{\mathbf{z}}$, filling in the R and z Dejonghe and de Zeeuw (1988) provide in terms of λ, ν, α, and γ.

$$R^2 = \frac{(\lambda + \alpha)(\nu + \alpha)}{\alpha - \gamma} \tag{A.1}$$

$$z^2 = \frac{(\lambda + \gamma)(\nu + \gamma)}{\gamma - \alpha} \tag{A.2}$$

We can then write:

$$P = \left| \frac{\partial R}{\partial \lambda}\hat{\mathbf{R}} + \frac{\partial z}{\partial \lambda}\hat{\mathbf{z}} \right| \tag{A.3}$$

$$Q = \left| \frac{\partial R}{\partial \nu}\hat{\mathbf{R}} + \frac{\partial z}{\partial \nu}\hat{\mathbf{z}} \right| \tag{A.4}$$

Beginning with P, we can start by calculating the two partial derivatives.

$$
\begin{aligned}
\frac{\partial R}{\partial \lambda} &= \frac{\partial}{\partial \lambda}\left(\sqrt{\frac{(\lambda+\alpha)(\nu+\alpha)}{\alpha-\gamma}}\right) \\
&= \frac{1}{2}\sqrt{\frac{\alpha-\gamma}{(\lambda+\alpha)(\nu+\alpha)}}\frac{\partial}{\partial \lambda}\left(\frac{(\lambda+\alpha)(\nu+\alpha)}{\alpha-\gamma}\right) \\
&= \frac{1}{2}\sqrt{\frac{\alpha-\gamma}{(\lambda+\alpha)(\nu+\alpha)}}\left(\frac{\nu+\alpha}{\alpha-\gamma}\right)
\end{aligned} \tag{A.5}
$$

$$
\begin{aligned}
\frac{\partial z}{\partial \lambda} &= \frac{\partial}{\partial \lambda}\left(\sqrt{\frac{(\lambda+\gamma)(\nu+\gamma)}{\gamma-\alpha}}\right) \\
&= \frac{1}{2}\sqrt{\frac{\gamma-\alpha}{(\lambda+\gamma)(\nu+\gamma)}}\frac{\partial}{\partial \lambda}\left(\frac{(\lambda+\gamma)(\nu+\gamma)}{\gamma-\alpha}\right) \\
&= \frac{1}{2}\sqrt{\frac{\gamma-\alpha}{(\lambda+\gamma)(\nu+\gamma)}}\left(\frac{\nu+\gamma}{\gamma-\alpha}\right)
\end{aligned} \tag{A.6}
$$

Now we can plug Equations A.5 and A.6 back into A.3.

$$
\begin{aligned}
P &= \left|\frac{1}{2}\sqrt{\frac{\alpha-\gamma}{(\lambda+\alpha)(\nu+\alpha)}}\left(\frac{\nu+\alpha}{\alpha-\gamma}\right)\hat{\mathbf{R}} + \frac{1}{2}\sqrt{\frac{\gamma-\alpha}{(\lambda+\gamma)(\nu+\gamma)}}\left(\frac{\nu+\gamma}{\gamma-\alpha}\right)\hat{\mathbf{z}}\right| \\
&= \sqrt{\left(\frac{1}{2}\sqrt{\frac{\alpha-\gamma}{(\lambda+\alpha)(\nu+\alpha)}}\left(\frac{\nu+\alpha}{\alpha-\gamma}\right)\right)^2 + \left(\frac{1}{2}\sqrt{\frac{\gamma-\alpha}{(\lambda+\gamma)(\nu+\gamma)}}\left(\frac{\nu+\gamma}{\gamma-\alpha}\right)\right)^2} \\
&= \frac{1}{2}\sqrt{\frac{\nu+\alpha}{(\lambda+\alpha)(\alpha-\gamma)} + \frac{\nu+\gamma}{(\lambda+\gamma)(\gamma-\alpha)}} \\
&= \frac{1}{2}\sqrt{\frac{1}{\alpha-\gamma}\left(\frac{\nu+\alpha}{\lambda+\alpha} - \frac{\nu+\gamma}{\lambda+\gamma}\right)} \\
&= \frac{1}{2}\sqrt{\frac{1}{\alpha-\gamma}\left(\frac{(\nu+\alpha)(\lambda+\gamma)-(\nu+\gamma)(\lambda+\alpha)}{(\lambda+\alpha)(\lambda+\gamma)}\right)} \\
&= \frac{1}{2}\sqrt{\frac{1}{\alpha-\gamma}\left(\frac{(\lambda-\nu)(\alpha-\gamma)}{(\lambda+\alpha)(\lambda+\gamma)}\right)} \\
&= \frac{1}{2}\sqrt{\frac{\lambda-\nu}{(\lambda+\alpha)(\lambda+\gamma)}}
\end{aligned} \tag{A.7}
$$

Squaring the result of Equation A.7 gives the P^2 value quoted in Dejonghe and de Zeeuw (1988) and Sommer-Larsen and Zhen (1990) (Equation 2.29 in this work).

The metric coefficient Q can be derived in the same manner, as shown below.

$$\begin{aligned}
\frac{\partial R}{\partial \nu} &= \frac{\partial}{\partial \nu}\left(\sqrt{\frac{(\lambda+\alpha)(\nu+\alpha)}{\alpha-\gamma}}\right) \\
&= \frac{1}{2}\sqrt{\frac{\alpha-\gamma}{(\lambda+\alpha)(\nu+\alpha)}}\frac{\partial}{\partial \nu}\left(\frac{(\lambda+\alpha)(\nu+\alpha)}{\alpha-\gamma}\right) \\
&= \frac{1}{2}\sqrt{\frac{\alpha-\gamma}{(\lambda+\alpha)(\nu+\alpha)}}\left(\frac{\lambda+\alpha}{\alpha-\gamma}\right)
\end{aligned} \tag{A.8}$$

$$\begin{aligned}
\frac{\partial z}{\partial \nu} &= \frac{\partial}{\partial \nu}\left(\sqrt{\frac{(\lambda+\gamma)(\nu+\gamma)}{\gamma-\alpha}}\right) \\
&= \frac{1}{2}\sqrt{\frac{\gamma-\alpha}{(\lambda+\gamma)(\nu+\gamma)}}\frac{\partial}{\partial \nu}\left(\frac{(\lambda+\gamma)(\nu+\gamma)}{\gamma-\alpha}\right) \\
&= \frac{1}{2}\sqrt{\frac{\gamma-\alpha}{(\lambda+\gamma)(\nu+\gamma)}}\left(\frac{\lambda+\gamma}{\gamma-\alpha}\right)
\end{aligned} \tag{A.9}$$

Now we can plug Equations A.8 and A.9 back into A.4.

$$
\begin{aligned}
Q &= \left| \frac{1}{2}\sqrt{\frac{\alpha-\gamma}{(\lambda+\alpha)(\nu+\alpha)}}\left(\frac{\lambda+\alpha}{\alpha-\gamma}\right)\hat{\mathbf{R}} + \frac{1}{2}\sqrt{\frac{\gamma-\alpha}{(\lambda+\gamma)(\nu+\gamma)}}\left(\frac{\lambda+\gamma}{\gamma-\alpha}\right)\hat{\mathbf{z}} \right| \\
&= \sqrt{\left(\frac{1}{2}\sqrt{\frac{\alpha-\gamma}{(\lambda+\alpha)(\nu+\alpha)}}\left(\frac{\lambda+\alpha}{\alpha-\gamma}\right)\right)^2 + \left(\frac{1}{2}\sqrt{\frac{\gamma-\alpha}{(\lambda+\gamma)(\nu+\gamma)}}\left(\frac{\lambda+\gamma}{\gamma-\alpha}\right)\right)^2} \\
&= \frac{1}{2}\sqrt{\frac{\lambda+\alpha}{(\nu+\alpha)(\alpha-\gamma)} + \frac{\lambda+\gamma}{(\nu+\gamma)(\gamma-\alpha)}} \\
&= \frac{1}{2}\sqrt{\frac{1}{\alpha-\gamma}\left(\frac{\lambda+\alpha}{\nu+\alpha} - \frac{\lambda+\gamma}{\nu+\gamma}\right)} \\
&= \frac{1}{2}\sqrt{\frac{1}{\alpha-\gamma}\left(\frac{(\lambda+\alpha)(\nu+\gamma)-(\lambda+\gamma)(\nu+\alpha)}{(\nu+\alpha)(\nu+\gamma)}\right)} \\
&= \frac{1}{2}\sqrt{\frac{1}{\alpha-\gamma}\left(\frac{(\nu-\lambda)(\alpha-\gamma)}{(\nu+\alpha)(\nu+\gamma)}\right)} \\
&= \frac{1}{2}\sqrt{\frac{\nu-\lambda}{(\nu+\alpha)(\nu+\gamma)}}
\end{aligned}
\tag{A.10}
$$

Squaring the result of Equation A.10 gives the Q^2 value quoted in Dejonghe and de Zeeuw (1988) and Sommer-Larsen and Zhen (1990) (Equation 2.30 in this work).

A.1.2 Integrals of Motion

Our goal is to solve the Hamilton-Jacobi equation using the time-independent function W where $p_i = \partial W/\partial q_i$ (Hamilton's characteristic function).

Starting with the Hamiltonian introduced in Chapter 2, Section 2.3,

$$
H = \frac{p_\lambda^2}{2P^2} + \frac{p_\phi^2}{2R^2} + \frac{p_\nu^2}{2Q^2} + \Psi, \tag{A.11}
$$

we can fill in W and $E = -H$ to get

$$
0 = \frac{1}{2P^2}\left(\frac{\partial W}{\partial \lambda}\right)^2 + \frac{p_\Phi^2}{2R^2} + \frac{1}{2Q^2}\left(\frac{\partial W}{\partial \nu}\right)^2 + \Psi + E. \tag{A.12}
$$

Now we fill in the potential and the metric coefficients derived in the previous section.

$$
\begin{aligned}
0 = & \frac{2(\lambda+\alpha)(\lambda+\gamma)}{(\lambda-\nu)}\left(\frac{\partial W}{\partial \lambda}\right)^2 - \frac{2(\nu+\alpha)(\nu+\gamma)}{(\lambda-\nu)}\left(\frac{\partial W}{\partial \nu}\right)^2 \\
& + \frac{(\alpha-\gamma)p_\Phi^2}{2(\lambda+\alpha)(\nu+\alpha)} - \frac{(\lambda+\gamma)G(\lambda)-(\nu+\gamma)G(\nu)}{(\lambda-\nu)} + E
\end{aligned} \tag{A.13}
$$

Followed by some re-arranging, below.

$$
\begin{aligned}
0 = & \, 2(\lambda+\alpha)(\lambda+\gamma)\left(\frac{\partial W}{\partial \lambda}\right)^2 - 2(\nu+\alpha)(\nu+\gamma)\left(\frac{\partial W}{\partial \nu}\right)^2 \\
& + \frac{(\lambda-\nu)(\alpha-\gamma)p_\Phi^2}{2(\lambda+\alpha)(\nu+\alpha)} - (\lambda+\gamma)G(\lambda) + (\nu+\gamma)G(\nu) + (\lambda-\nu)E \\
& = 2(\nu+\alpha)(\lambda+\alpha)^2(\lambda+\gamma)\left(\frac{\partial W}{\partial \lambda}\right)^2 - 2(\lambda+\alpha)(\nu+\alpha)^2(\nu+\gamma)\left(\frac{\partial W}{\partial \nu}\right)^2 \\
& + \frac{1}{2}(\lambda-\nu)(\alpha-\gamma)p_\Phi^2 + (\lambda+\alpha)(\nu+\alpha)(-(\lambda+\gamma)G(\lambda) + (\nu+\gamma)G(\nu)) \\
& + (\lambda+\alpha)(\nu+\alpha)(\lambda-\nu)E
\end{aligned} \tag{A.14}
$$

The final term of the equation above can be simplified as follows:

$$
\begin{aligned}
(\lambda+\alpha)(\nu+\alpha)(\lambda-\nu)E &= (\lambda\nu+\lambda\alpha+\alpha\nu+\alpha^2)(\lambda-\nu)E \\
&= (\lambda^2\nu+\lambda^2\alpha+\alpha\nu\lambda+\alpha^2\lambda-\lambda\nu^2-\lambda\alpha\nu-\alpha\nu^2-\alpha^2\nu)E \\
&= (\lambda^2\nu+\lambda^2\alpha+\alpha^2\lambda-\lambda\nu^2-\alpha\nu^2-\alpha^2\nu)E \\
&= (\lambda^2(\nu+\alpha)+\alpha^2(\lambda-\nu)-\nu^2(\lambda+\alpha))E.
\end{aligned} \tag{A.15}
$$

Combining Equations A.14 and A.15, we get an equation that separates more cleanly into λ, Φ, and ν terms.

$$\begin{aligned}
0 &= (\nu+\alpha)\left(2(\lambda+\alpha)^2(\lambda+\gamma)\left(\frac{\partial W}{\partial \lambda}\right)^2 - (\lambda+\alpha)(\lambda+\gamma)G(\lambda) + \lambda^2 E\right) \\
&\quad - (\lambda+\alpha)\left(2(\nu+\alpha)^2(\nu+\gamma)\left(\frac{\partial W}{\partial \nu}\right)^2 - (\nu+\alpha)(\nu+\gamma)G(\nu) + \nu^2 E\right) \\
&\quad + (\lambda-\nu)\left(\frac{1}{2}(\alpha-\gamma)p_\Phi^2 + \alpha^2 E\right) \\
&= (\nu+\alpha)U(\lambda) - (\lambda+\alpha)U(\nu) + (\lambda-\nu)C_\Phi
\end{aligned} \tag{A.16}$$

Where the function $U(\tau)$ is

$$U(\tau) = 2(\tau+\alpha)^2(\tau+\gamma)\left(\frac{\partial W}{\partial \tau}\right)^2 - (\tau+\alpha)(\tau+\gamma)G(\tau) + \tau^2 E \tag{A.17}$$

for $\tau = \lambda, \nu$ and $C_\Phi = \frac{1}{2}(\alpha-\gamma)p_\Phi^2 + \alpha^2 E$ is a constant used for convenience.

We can show (as demonstrated below), by taking the derivatives of Equation A.16 with respect to λ and ν, that $\partial U(\tau)/\partial\tau$ is independent of τ, meaning the function $U(\tau)$ must take the form $j\tau \pm k$.

$$\begin{aligned}
0 &= (\nu+\alpha)\frac{\partial U(\lambda)}{\partial \lambda} - U(\nu) + C_\Phi \\
\frac{\partial U(\lambda)}{\partial \lambda} &= \frac{U(\nu) - C_\Phi}{(\nu+\alpha)}
\end{aligned} \tag{A.18}$$

$$\begin{aligned}
0 &= U(\lambda) - (\lambda+\alpha)\frac{\partial U(\nu)}{\partial \nu} - C_\Phi \\
\frac{\partial U(\nu)}{\partial \nu} &= \frac{U(\lambda) - C_\Phi}{(\lambda+\alpha)}
\end{aligned} \tag{A.19}$$

Filling in $U(\tau) = j\tau - k$ in Equation A.17, we can solve for $p_\tau = \partial W/\partial\tau$ in terms of τ and the new constants j and k.

$$\begin{aligned} j\tau - k &= 2(\tau+\alpha)^2(\tau+\gamma)p_\tau^2 - (\tau+\alpha)(\tau+\gamma)G(\tau) + \tau^2 E \\ -2(\tau+\alpha)^2(\tau+\gamma)p_\tau^2 &= -(\tau+\alpha)(\tau+\gamma)G(\tau) + \tau^2 E - j\tau + k \\ -2(\tau+\alpha)p_\tau^2 &= -G(\tau) + \frac{\tau^2 E - j\tau + k}{(\tau+\alpha)(\tau+\gamma)} \\ p_\tau^2 &= \frac{1}{2}(\tau+\alpha)\left(G(\tau) + \frac{j\tau - k - \tau^2 E}{(\tau+\alpha)(\tau+\gamma)}\right) \end{aligned} \tag{A.20}$$

Constants j and k can then be solved using Equations A.16 and A.17. The integrals of motion are, by convention, usually given in terms of j and k as:

$$I_2 = \frac{\alpha^2 H + \alpha j + k}{\alpha - \gamma} \tag{A.21}$$

$$I_3 = \frac{\gamma^2 H + \gamma j + k}{\gamma - \alpha} \tag{A.22}$$

Solving for I_2 and I_3 in terms of the Cartesian coordinates gives Equations 14 and 15 from Sommer-Larsen and Zhen (1990) (given in Chapter 2, Section 2.3 of this work).

A.2 Codes

A.2.1 Carbon Evolution Batch Submission

The following code creates an executable file which can be run on `nuit`, or any machine with `ccor` installed, to produce an output file containing the evolutionary carbon corrections developed by Placco et al. (2014).

```
import numpy as np
import argparse

parser = argparse.ArgumentParser()
parser.add_argument("input_file", help="csv file of input data",
    action="store")
parser.add_argument("output_file", help="name of file to store
    output data in", action="store")
```

```
parser.add_argument("delta_c_file", help="name of file to store
    carbon corrections in", action="store")
parser.add_argument("--mrc", help="were medium-resolution
    corrections already applied to logg, feh, & cfe?", action="
    store_true", default=False)

args = parser.parse_args()

input_file = args.input_file
output_file = args.output_file
dc_file = args.delta_c_file
med_res_corr = args.mrc

a1=np.genfromtxt(input_file,names=True,case_sensitive='lower',
    delimiter=',',dtype=None)

o=open(output_file,'w')
o.write('#!/bin/bash\n')

for row in range(0,len(a1)):

  if(med_res_corr==True):
    logg=a1[row]['logg_mrc']
    feh=a1[row]['feh_mrc']
    cfe=a1[row]['cfe_mrc']
  else:
    logg=a1[row]['logg']
    feh=a1[row]['feh']
    cfe=a1[row]['cfe']

  if( logg!=-9.999 and feh!=-9.999 and cfe!=-9.999):
    o.write('echo -n {}, >> {}\n'.format(a1[row]['name'],dc_file))
    o.write('ccor {} {} {} >> {}\n'.format(logg, feh, cfe, dc_file))
  if(row%100==0 and row!=0):
    o.write('echo "{}/{} corrections completed"\n'.format(row, len(
    a1)))

o.write('echo "\\rall done"')
o.close()
```

A.2.2 Kinematics Mini-Pipeline

The "mini-pipeline" in Section A.2.2.1 uses `galpy` to derive/transform useful kinematic parameters (see Chapter 2) for an inputted CSV file. Section A.2.2.2 contains the updated, Python version of the Chiba and Beers (2000) Galactic potential code (Note: the code given in Section A.2.2.1 calls the code given in Section A.2.2.2).

A.2.2.1 dietz_mini_pipeline_v1.py

```
import matplotlib
matplotlib.use('Agg')
from matplotlib import pyplot as plt
```

```
from galpy.util import bovy_coords as b_c
import galpy.potential as pot
from astropy import units as u
import numpy as np
from scipy.stats import norm
import math as m
import os
import datetime
import collections
import staeckel_orbit
import sys
from sys import argv, stdout

input_file = argv[1]
main_title = argv[2]
dir_name = argv[3]

final_dir_name = "{}/{}_kin".format(dir_name,main_title)

if not os.path.exists(final_dir_name):
    os.makedirs(final_dir_name)

final_dir_name = final_dir_name + "/"

output_file = "{}{}_kin.csv".format(final_dir_name,main_title)

f = open(input_file)
o = open(output_file, 'w')

#create array from csv file
a1 = np.genfromtxt(f, autostrip=True, delimiter=",", names=True,
   case_sensitive="lower", dtype=None)

#if using pipeline with condor
if(len(sys.argv)==6):
  start = int(argv[4])
  stop = int(argv[5])
else:
  start = 0
  stop = len(a1)

#condor option
if(stop > len(a1)):
  stop = len(a1)

loop_length = stop - start

global Xsun
Xsun = 8.
global Zsun
Zsun = 0.
global vcirc
vcirc = 220.
global vsun
vsun1 = [-9.0, 12.0 + vcirc, 7.0]

global vsun2
vsun2=[-9.,12.,7.]

global N_orbits
N_orbits = 1000
print "\n"

#returns (heliocentric & galactocentric) x,y,z
def xyz(req_dict):

  #get heliocentric position
```

```
  x_hc, y_hc, z_hc = b_c.lbd_to_XYZ(req_dict['l'], req_dict['b'],
   req_dict['dist'], degree=True)

  #get galactocentric position
  x_gc, y_gc, z_gc = b_c.XYZ_to_galcenrect(x_hc, y_hc, z_hc, Xsun,
   Zsun)

  return float(x_gc), y_gc, float(z_gc)

#returns (heliocentric & galactocentric) cartesian velocities
def uvw(req_dict):

  #get vx, vy, vz (heliocentric) in R-handed coord. syst.
  u, v, w = b_c.vrpmllpmbb_to_vxvyvz(req_dict['rv'], req_dict['pml'
   ], req_dict['pmb'], req_dict['l'], req_dict['b'], req_dict['dist'
   ], XYZ=False, degree=True)

  #get vx, vy, vz (galactocentric) in L-handed coord syst (corrected
    for sun & disk motion)
  vx_gc, vy_gc, vz_gc = b_c.vxvyvz_to_galcenrect(u, v, w, vsun1,
   Xsun, Zsun)

  return u, v, w, float(vx_gc), vy_gc, float(vz_gc)

#returns (L-handed) galactocentric cylindrical coords
def cyl_coords(calc_dict):

  R, phi, z = b_c.rect_to_cyl(calc_dict['x_gc'],calc_dict['y_gc'],
   calc_dict['z_gc'])

  return R, phi

#returns (L-handed) galactocentric cylindrical velocities
def cylindrical_vs(calc_dict):

  vRg, vTg, vZg = b_c.rect_to_cyl_vec(calc_dict['vx_gc'],calc_dict['
   vy_gc'],calc_dict['vz_gc'],calc_dict['x_gc'],calc_dict['y_gc'],
   calc_dict['z_gc'])

  return vRg, vTg

#returns uncertainties in u,v,w
def uvw_unc(req_dict, opt_dict):

  cov_radec=np.zeros((2,2))
  cov_radec[0,0]=opt_dict['epmra']**2
  cov_radec[1,1]=opt_dict['epmdec']**2

  covar_pmllbb=b_c.cov_pmrapmdec_to_pmllpmbb(cov_radec, req_dict['ra
   '], req_dict['dec'], degree=True, epoch=2000.0)

  cov_vxvyvz=b_c.cov_dvrpmllbb_to_vxyz(req_dict['dist'], opt_dict['
   edist'], opt_dict['erv'], req_dict['pml'], req_dict['pmb'],
   covar_pmllbb, req_dict['l'], req_dict['b'] , plx=False, degree=
   True)

  du=vx_e=m.sqrt(cov_vxvyvz[0,0])
  dv=vy_e=m.sqrt(cov_vxvyvz[1,1])
  dw=vz_e=m.sqrt(cov_vxvyvz[2,2])

  return du, dv, dw

#returns a dict of orbital parameters from staeckel_orbit.py
def orbit_1_staeckel(req_dict, calc_dict):
```

```
  returned_orb = staeckel_orbit.run(req_dict, calc_dict)

  if(-9.999 in returned_orb):
    returned_orb['bound']=False

  return returned_orb

#returns orbital parameter uncertainties
def orbit_N(method,req_dict, opt_dict, calc_dict):

  count_orbits=0.

  orbit_params={'Energy':[], 'L_z':[], 'L_p':[], 'I_3':[], 'Z_max'
   :[],
  'ecc':[], 'r_apo':[], 'r_peri':[], 'R_apo_P':[], 'R_peri_P':[]}

  orbit_unc={'Energy_unc':-9.999, 'L_z_unc':-9.999, 'L_p_unc'
   :-9.999, 'I_3_unc':-9.999, 'Z_max_unc':-9.999,
  'ecc_unc':-9.999, 'r_apo_unc':-9.999, 'r_peri_unc':-9.999, '
   R_apo_P_unc':-9.999, 'R_peri_P_unc':-9.999, 'N_orbits':-9.999}

  #loop over N orbits
  for i in range(0,N_orbits):

    #generate input parameters by randomly selecting from a normal
   distribution with spread = input uncertainty
    rand_dict = req_params.copy()

    rand_dict['dist'] = np.random.normal(loc=req_dict["dist"], scale
   =opt_dict["edist"])
    rand_dict['rv'] = np.random.normal(loc=req_dict["rv"], scale=
   opt_dict["erv"])

    rand_dict['pmra'] = np.random.normal(loc=req_dict["pmra"], scale
   =opt_dict["epmra"])
    rand_dict['pmdec'] = np.random.normal(loc=req_dict["pmdec"],
   scale=opt_dict["epmdec"])

    rand_dict['pml'], rand_dict['pmb'] = b_c.pmrapmdec_to_pmllpmbb(
   rand_dict['pmra'], rand_dict['pmdec'], req_dict['ra'], req_dict['
   dec'], degree=True, epoch=2000.0)

    #use randomly generated input parameters to calculate positions,
    velocities
    rand_x, rand_y, rand_z = xyz(rand_dict)
    rand_u, rand_v, rand_w, rand_vx_gc, rand_vy_gc, rand_vz_gc = uvw
   (rand_dict)

    rand_calc_dict=collections.OrderedDict([('x_gc',rand_x),('y_gc',
   rand_y),('z_gc',rand_z),
    ('u',rand_u),('v',rand_v),('w',rand_w),
    ('vx_gc',rand_vx_gc),('vy_gc',rand_vy_gc),('vz_gc',rand_vz_gc),
    ('R',-9.999),('phi',-9.999),('vRg',-9.999),('vTg',-9.999)])

    rand_calc_dict['R'], rand_calc_dict['phi'] = cyl_coords(
   rand_calc_dict)
    rand_calc_dict['vRg'], rand_calc_dict['vTg'] = cylindrical_vs(
   rand_calc_dict)

    returned_orb = orbit_1_staeckel(rand_dict,rand_calc_dict)

    for key in returned_orb:
      if(returned_orb['bound']==True and key in orbit_params):
        orbit_params[key].append(returned_orb[key])
```

```
    if(returned_orb['bound']==True):
      count_orbits+=1.

  orbit_unc['N_orbits'] = count_orbits

  fits_dir_name = "{}{}_uncertainty_fits".format(final_dir_name,
   method)

  if not os.path.exists(fits_dir_name):
    os.makedirs(fits_dir_name)

  fits_dir_name = fits_dir_name + "/"

  f, axarr = plt.subplots(5,2, figsize=(12, 10))

  row_num = 0
  col_num = 0

  for key in orbit_params:

    data = orbit_params[key]

    #fit a gaussian to the randomly generated orbital parameters
    mu, std = norm.fit(data)

    #uncertainty on parameter = standard dev of fit
    orbit_unc['{}_unc'.format(key)]=std

    #plot the histogram
    axarr[row_num,col_num].hist(data, bins=25, normed=True,
   facecolor='none', edgecolor="black", histtype="step")

    #plot the fit
    xmin, xmax = axarr[row_num,col_num].get_xlim()
    x = np.linspace(xmin, xmax, 100)
    p = norm.pdf(x, mu, std)
    axarr[row_num,col_num].plot(x, p, 'k', linewidth=2)

    #plot the calculated parameter value
    axarr[row_num,col_num].axvline(x=calc_dict[key], color='b', ls =
   '--', lw=2)

    #plot the mean of the fit
    axarr[row_num,col_num].axvline(x=mu, color='k', lw =2)

    axarr[row_num,col_num].set_title("{} (mu = {}, std = {})".format
   (key, round(mu,2), round(std,2)))

    if(col_num==0):
      col_num+=1
    else:
      col_num=0
      row_num+=1

  plt.tight_layout()
  plt.savefig("{}{}_{}_{}_fits.png".format(fits_dir_name,main_title,
   req_dict['name'],method))
  plt.close()

  return orbit_unc

def calculate():

  global req_params
  global opt_params
```

```
global calc_params

bad_input = False

#check for invalid required params
for key in req_params:
  if(key != "name"):
    if((m.isnan(float(req_params[key]))==True) or (req_params[key
]==-9.999) or (req_params[key]==-9999.9)):
      bad_input = True
    if(isinstance(req_params[key], str)==True):
      bad_input = True

#valid required params, continue to calculations
if(bad_input==False):
  #get heliocentric & galactocentric x,y,z
  calc_params['x_gc'], calc_params['y_gc'], calc_params['z_gc'] =
 xyz(req_params)

  #calculate galactocentric distance
  calc_params['R_gal']=np.sqrt(calc_params['x_gc']**2+calc_params[
 'y_gc']**2+calc_params['z_gc']**2)

  #get heliocentric & galactocentric cartesian velocities
  calc_params['u'], calc_params['v'], calc_params['w'],
 calc_params['vx_gc'], calc_params['vy_gc'], calc_params['vz_gc']
 = uvw(req_params)

  #get cylindrical coordinates
  calc_params['R'], calc_params['phi'] = cyl_coords(calc_params)

  #get cylindrical velocities
  calc_params['vRg'], calc_params['vTg'] = cylindrical_vs(
 calc_params)

  staeckel_orb = orbit_1_staeckel(req_params,calc_params)
  for key in calc_params:
    if(key in staeckel_orb):
      calc_params[key]=staeckel_orb[key]

  uncert_list = [opt_params['epmra'],opt_params['epmdec'],
 opt_params['erv'],opt_params['edist']]

  calc_uncert = True

  #check for invalid uncertainty params
  for err in uncert_list:
    if((m.isnan(float(err))==True) or (err==-9.999) or (err
==-9999.9)):
      calc_uncert = False
    if(isinstance(err, str)==True):
      calc_uncert = False

  #valid uncertainty params, continue to calculations
  if(calc_uncert==True):
    staeckel_orb_unc = orbit_N("staeckel",req_params,opt_params,
 calc_params)
    for key in calc_params:
      if key in staeckel_orb_unc:
        calc_params[key]=staeckel_orb_unc[key]

#invalid required params
if(bad_input==True):
  no_xyz = False
  for key in ['l','b','dist']:
```

```
      if((m.isnan(float(req_params[key]))==True) or (req_params[key
]==-9.999)):
        no_xyz = True
      if(isinstance(req_params[key], str)==True):
        no_xyz = True

    if(no_xyz==False):
      #get galactocentric x,y,z
      calc_params['x_gc'], calc_params['y_gc'], calc_params['z_gc']
 = xyz(req_params)
      #calculate galactocentric distance
      calc_params['R_gal']=np.sqrt(calc_params['x_gc']**2+
calc_params['y_gc']**2+calc_params['z_gc']**2)
      #get cylindrical coordinates
      calc_params['R'], calc_params['phi'] = cyl_coords(calc_params)

  if(-9.999 not in [opt_params['edist'],opt_params['epmra'],
opt_params['epmdec']]):
    #get uncertainties in u,v,w
    calc_params['du'], calc_params['dv'], calc_params['dw'] =
uvw_unc(req_params, opt_params)

  for key in req_params:
    o.write("{},".format(req_params[key]))
  for key in opt_params:
    o.write("{},".format(opt_params[key]))
  for key in calc_params:
    o.write("{},".format(calc_params[key]))

  #get rid of that last comma & add a new line
  o.seek(-1, os.SEEK_END)
  o.truncate()
  o.write("\n")

#function calls all conversion sub-functions
def convert():

  global req_params

  #if position given in ra & dec, convert to l & b
  if(req_params.get('l')==-9.999):
    req_params['l'], req_params['b'] = b_c.radec_to_lb(req_params['
ra'], req_params['dec'], degree=True, epoch=2000.0)

  #if position given in l & b, convert to ra & dec
  if(req_params.get('ra')==-9.999):
    req_params['ra'], req_params['dec'] = b_c.lb_to_radec(req_params
['l'], req_params['b'], degree=True, epoch=2000.0)

  #if proper motion given in pmra & pmdec, convert to pml & pmb
  if(req_params.get('pml')==-9.999):
    req_params['pml'], req_params['pmb'] = b_c.pmrapmdec_to_pmllpmbb
(req_params['pmra'], req_params['pmdec'], req_params['ra'],
req_params['dec'], degree=True, epoch=2000.0)

#cycle through rows of data, perform conversions & calculations
def loop():

  global req_params
  global opt_params
  global calc_params

  #write output file header
  for key in req_params:
    o.write("{},".format(key))
  for key in opt_params:
```

```
    o.write("{},".format(key))
  for key in calc_params:
    o.write("{},".format(key))

  #get rid of that last comma & add a new line
  o.seek(-1, os.SEEK_END)
  o.truncate()
  o.write("\n")

  #function that lets you rename dict keys
  def change_key(dict, old_key, new_key):
    dict[new_key] = dict.pop(old_key)

#---start looping through stars

  #for row in range(0,loop_length):
  for row in range(start,stop):

    #print a progress statement
    stdout.write("\r{}/{}: {}".format(row+1,loop_length,a1[row]['
   name']))
    stdout.flush()

    reset()

#-------start filling param dicts

    for param_key in req_params:
      try:
        #if star has the required param, store it
        req_params[param_key] = a1[row][param_key]
      except:
        #if not, move on
        pass

    for param_key in opt_params:
      try:
        #if star has the optional param, store it
        opt_params[param_key] = a1[row][param_key]
      except:
        #if not, move on
        pass

#-------end filling param dicts

    req_params['pmra'] = float(req_params['pmra'])
    opt_params['epmra'] = float(opt_params['epmra'])
    req_params['pmdec'] = float(req_params['pmdec'])
    opt_params['epmdec'] = float(opt_params['epmdec'])
    req_params['pml'] = float(req_params['pml'])
    req_params['pmb'] = float(req_params['pmb'])

    convert()
    calculate()

#---end looping through stars

print("\noriginal number of stars: {}\n".format(loop_length))

#param dicts
global req_params
global opt_params
global calc_params

#reset param dict vals
def reset():
```

```
  global req_params
  global opt_params
  global calc_params

  #params that must be given
  req_params=collections.OrderedDict([('name','None'),
  ('ra',-9.999), ('dec',-9.999),
  ('pmra',-9.999), ('pmdec',-9.999),
  ('l',-9.999), ('b',-9.999),
  ('pml',-9.999), ('pmb',-9.999),
  ('rv',-9.999), ('dist',-9.999)])

  #extra params
  opt_params=collections.OrderedDict([('epmra',-9.999), ('epmdec'
    ,-9.999),
  ('erv',-9.999), ('edist',-9.999),
  ('kin_in',None)])

  #params that will be calculated
  calc_params=collections.OrderedDict([('x_gc',-9.999),('y_gc'
    ,-9.999),('z_gc',-9.999),('R_gal',-9.999),
  ('u',-9.999),('du',-9.999),('v',-9.999),('dv',-9.999),('w',-9.999)
    ,('dw',-9.999),
  ('vx_gc',-9.999),('vy_gc',-9.999),('vz_gc',-9.999),
  ('R',-9.999),('phi',-9.999),('vRg',-9.999),('vTg',-9.999),
  ('N_orbits',-9.999),('bound',False),
  ('Energy',-9.999),('Energy_unc',-9.999),('L_z',-9.999),('L_z_unc'
    ,-9.999),('L_p',-9.999),('L_p_unc',-9.999),('I_3',-9.999),('
    I_3_unc',-9.999),('Z_max',-9.999),('Z_max_unc',-9.999),
  ('ecc',-9.999),('ecc_unc',-9.999),('r_apo',-9.999),('r_apo_unc'
    ,-9.999),('r_peri',-9.999),('r_peri_unc',-9.999),('R_apo_P'
    ,-9.999),('R_apo_P_unc',-9.999),('R_peri_P',-9.999),('
    R_peri_P_unc',-9.999)])

reset()
loop()

f.close()
o.close()
```

A.2.2.2 staeckel_orbit.py

```
import numpy as np
import math as m
import collections

#input file:
#x, y, z, R, dist, u, v, w, v_r, v_phi, v_x, v_y

# output file:
#e, r_max, r_min, R_max, R_min, Z_max, E, L_z, (L_x^2+L_y^2)^1/2,
   I_3, Z_max
#e : signed e (>0 for prograde, <0 for retrograde)
#r_max, r_min : maximum and minimum galactocentric radii (kpc)
#R_max, R_min : maximum and minimum distances along the galactic
   plane (kpc)
#Z_max : maximum distance away from the galactic plane (kpc)

#For unbound stars, the value '-9.999' is assigned.

#E : total energy ((km/s)^2) (<0 for bound stars)
#L_i : i-component of angular momentum (kpc km/s)
#I_3 : 3rd integral of motion ((kpc km/s)^2)
```

```python
def run(req_dict, calc_dict):
  #nmdat = 200000

  global neg_alpha_sqrt,gamma_dummy,neg_alpha,neg_gamma,q,del2,
   disk_mass #disk
  global sah,c,sah2,c2,qh,rho_0,rt #halo
  global x,y,vx,vy,r,z,vr,vz,vp,lambda_,nu,vlam,vnu #phas
  global energy,I_2,I_3 #inte
  global eccentricity,elsecc,cradecc,abun #feoh
  global rmin,rmax,crmin,crmax,zeta,zmax #apoc

  global gmb, b, vesc #els

  #set basic parameters
  set_params()

  #set up tau array
  mesh()

  #set file names
  #read file

  #read data, derive eccentricities and write results

  unbound_count = 0

  #data = np.genfromtxt(input_file,delimiter=',',names=True,
   case_sensitive="lower",dtype=None)

  #nmdat = len(data)
  nmdat = 1


  x = calc_dict['x_gc']
  y = calc_dict['y_gc']
  z = calc_dict['z_gc']
  r = calc_dict['R']
  dist = req_dict['dist']
  vx = calc_dict['vx_gc']
  vy = calc_dict['vy_gc']
  vz = calc_dict['vz_gc']
  vr = calc_dict['vRg']
  vp = calc_dict['vTg']

  global is_bound
  is_bound = 1
  #if distance is negative, kick out
  if(dist <= 0.):
    is_bound = -1
    getecc()
    #all values will be "-9.999"

  #get orbital parameters from Staeckel potential

  #determine (lambda,nu) from (R,z)
  position()

  #determine (v_lambda,v_nu) from (vr,vz,lambda_,nu,z)
  transform_velocities()

  #determine (E,I_2,I_3)
  get_EI2I3()

  #get boundaries of orbits
  gbound()

  vtot=0.
```

```
  if(is_bound == 0):
    unbound_count = unbound_count + 1
    vtot = m.sqrt( vr**2 + vp**2 + vz**2 )
    #o6.write("unbound: {}\nvtot = {}\n".format(unbound_count,vtot))
    #print "unbound: {}\nvtot = {}\n".format(unbound_count,vtot)

  #get eccentricities & write 'ecc.out'
  getecc()

  if(vp >= 0.):
    rsignecc = eccentricity
  if(vp < 0.):
    rsignecc = eccentricity
  if(eccentricity < -9.):
    rsignecc = -9.999

  #o20.write("{},{},{},{},{},{}\n".format(rsignecc,rmax,rmin,crmax,
   crmin,zmax))

  #angular momentum
  rlz = r * vp
  rlx = y * vz - z * vy
  rly = z * vx - x * vz
  rlt = m.sqrt( rlx**2 + rly**2 )

  true_energy = -energy

  #o40.write("{},{},{},{},{}\n".format(true_energy,rlz,rlt,I_3,zmax)
   )

  #o6.write("the number of stars employed={}\n".format(i-1))
  #o6.write("the number of unbound stars={}\n".format(unbound_count)
   )

  bound = False
  if(is_bound==1):
    bound = True

  return_dict = collections.OrderedDict([('Energy',true_energy),('
   L_z',rlz),('L_p',rlt),('I_3',I_3),('Z_max',zmax),
  ('ecc',rsignecc),('r_apo',rmax),('r_peri',rmin),('R_apo_P',crmax)
   ,('R_peri_P',crmin),('bound',bound)])
  return return_dict

#set the ELS potential
#see Chiba & Yoshii 1998 appendix
def set_params():

  global gmb, b, vesc #els
  global neg_alpha_sqrt,gamma_dummy,neg_alpha,neg_gamma,q,del2,
   disk_mass #disk
  global sah,c,sah2,c2,qh,rho_0,rt #halo

  #ELS potential at solar dist. = -GM/(b + bq)
  #where q = m.sqrt( (rsun/b)**2 + 1. )
  #M is disk mass
  #b is scale length

  #can evaluate b & q using definitions of vesc and vsun

  vesc = 500.

  rsun = 8.
  vsun = 220.

  q = 1. / ( 1. - (m.sqrt(2.)*vsun/vesc)**2 )
```

```
    #c = m.sqrt( q**2 - 1.)
    b = rsun / m.sqrt( q**2 - 1.)

    #now can evaluate for gm/b
    gmb = (vsun**2) * q / (q - 1.)

    #gmb = vsun * (1. + q) * m.sqrt(q)/m.sqrt( q**2 - 1.)
    #gmb = gmb**2

  #set Staeckel potential
    rt = 200.

    #disk parameters (perfect oblate disk)

    gamma_dummy  = 0.125
    del2 = 4.0**2
    neg_gamma = gamma_dummy**2
    neg_alpha = del2 + neg_gamma
    neg_alpha_sqrt  = m.sqrt( neg_alpha )
    q   = gamma_dummy / neg_alpha_sqrt

      #halo parameters (s=2 model)

    disk_mass = 9.0 * (10**10)
    rho_0   = 2.45 * (10**7)
    c   = 6.0
    c2 = c**2
    sah2 = del2 + c**2
    sah   = m.sqrt( sah2 )
    qh    = c / sah

  #COMMENT
  def mesh():

    nm = 10001

    global tau_array #arry
    tau_array = [None] * nm
    global neg_alpha_sqrt,gamma_dummy,neg_alpha,neg_gamma,q,del2,
     disk_mass #disk

    tmax = m.log10(40000.)
    tmin = m.log10(neg_gamma + (1. * m.pow(10.,-4.)) * neg_gamma )
    dt = (tmax - tmin) / float(nm)

    #CHECK ALL nm RANGES BEFORE FINAL VER
    for i in range (0,nm):
      dum = tmin + dt * (i)
      tau_array[i] = 10.**dum

  #get e_ELS, R_max, and R_min from ELS potential
  # def gels(elsecc,elsrmax,elsrmin):
  #
  #   global x,y,vx,vy,r,z,vr,vz,vp,lambda_,nu,vlam,vnu #phas
  #   global gmb, b, vesc #els
  #
  #   #(1) energy and angular momentum
  #
  #   elsene = felsene(vr,vp,r)
  #   elsang = felsang(vp,r)
  #
  #   if(elsene >= 0.):
  #     #unbounded
  #     elsecc = -9.999
  #     elsrmax = -9.999
  #     return
  #
```

```
#   #(2) R_min, R_max, and e_ELS
#
#   #neg_alpha, beta, and gamma
#   ralp2 = 1. + 4.*gmb * (b/elsang)**2
#   rgam  = (gmb - 2.*elsene) * (b/elsang)**2 / ralp2
#   rbet2 = rgam**2 + 2.*elsene * (b/elsang)**2 / ralp2
#   ralp = m.sqrt(ralp2)
#   rbet = m.sqrt(rbet2)
#
#   #R_min, R_max, and e_ELS
#   r1 = m.sqrt( 1. - 2.*(rgam-rbet) ) * b / (rgam - rbet)
#
#   if(( rgam+rbet ) > 0.5):
#     r2 = 0.
#   else:
#     r2 = m.sqrt( 1. - 2.*(rgam+rbet) ) * b / (rgam + rbet)
#
#   elsecc  = ( r1 - r2 ) / ( r1 + r2 )
#   elsrmax = r1
#   elsrmin = r2
#
# def felsene(vr,vp,r):
#
#   global gmb, b, vesc #els
#   felsene = 0.5 * ( vr**2 + vp**2 ) - gmb / ( 1. + m.sqrt( r**2 /
    b**2 + 1. ) )
#
# def felsang(vp,r):
#
#   felsang = r * vp

#G(tau) for disk
def G_disk(t):

  global neg_alpha_sqrt,gamma_dummy,neg_alpha,neg_gamma,q,del2,
   disk_mass #disk
  global sah,c,sah2,c2,qh,rho_0,rt #halo

  G_grav = 4.3013 * (10**(-6))
  eps = 1. * (10**(-11))

  #perfect oblate disk

  dum = t - neg_gamma

  if(dum > eps):
    #from equ. (7) in Sommer-Larsen & Zhen
    G_disk = ((2.*G_grav*disk_mass) / (m.pi*m.sqrt(t-neg_gamma))) *
   m.atan(m.sqrt((t-neg_gamma)/neg_gamma))
  elif(dum <= eps):
    #small angle approx
    #arctan(theta)~theta, so can simplify equation
    G_disk = 2.*G_grav*disk_mass/m.pi/m.sqrt(neg_gamma)

  return G_disk

#G(tau) for halo (0 at origin)
def fgh(t):

  global neg_alpha_sqrt,gamma_dummy,neg_alpha,neg_gamma,q,del2,
   disk_mass #disk
  global sah,c,sah2,c2,qh,rho_0,rt #halo

  G_grav = 4.3013 * (10**(-6))
  eps = 1. * (10**(-11))
```

```
  #s=2 model halo of de Zeeuw et al. (1986)

  dum = t - neg_gamma

  #possible sign error below, check later

  if(dum > eps):

    b = del2 + c2 - neg_alpha

    #from second line of equ. (9) from Sommer-Larsen & Zhen
    dum1 = m.log( (del2+neg_gamma+b)/(neg_gamma+b) ) - (t-neg_gamma+
   del2)/2./(t-neg_gamma) * m.log( (t+b)/(neg_gamma+b) )

    #from third & fourth lines of equ. (9) from Sommer-Larsen & Zhen
    dum2 = 1./m.sqrt(t-neg_gamma) * m.atan( m.sqrt( (t-neg_gamma)/(
   neg_gamma+b) ) ) - 1./m.sqrt(del2) * m.atan( m.sqrt(del2)/m.sqrt(
   neg_gamma+b) )

    #combine the above two parts...
    fgh = dum1 + (del2-neg_gamma-b)/m.sqrt(neg_gamma+b) * dum2

    #...and multiply by the terms in the first line of equ. (9) from
    Sommer-Larsen & Zhen
    fgh = - 4.*m.pi*G_grav*rho_0 * (-neg_gamma-b) * fgh

  elif(dum <= eps):
    #use small angle approx & Taylor expansion of ln to simplify fgh
    b = del2 + c2 - neg_alpha
    dum1 = m.log( (del2+neg_gamma+b)/(neg_gamma+b) ) - del2/2./(
   neg_gamma+b)
    dum2 = 1./m.sqrt(neg_gamma+b) - 1./m.sqrt(del2) * m.atan( m.sqrt
   (del2)/m.sqrt(neg_gamma+b) )
    fgh = dum1 + (del2-neg_gamma-b)/m.sqrt(neg_gamma+b) * dum2
    fgh = - 4.*m.pi*G_grav*rho_0 * (-neg_gamma-b) * fgh

  return fgh

#G(tau) for halo (0 at the cutoff radius)
def G_halo(t):

  global neg_alpha_sqrt,gamma_dummy,neg_alpha,neg_gamma,q,del2,
   disk_mass #disk
  global sah,c,sah2,c2,qh,rho_0,rt #halo

  lambda_d = rt**2 + neg_alpha

  cons = fgh(lambda_d) + G_disk(lambda_d)

  G_halo = fgh(t) - cons

  return G_halo

#G(tau) for disk + halo
#from equ. (6) in Sommer-Larsen & Zhen
def G(t):

  G = G_disk(t) + G_halo(t)

  return G

#dG(tau)/dtau for potential
def dG_dt(t):

  global neg_alpha_sqrt,gamma_dummy,neg_alpha,neg_gamma,q,del2,
   disk_mass #disk
```

```
  global sah,c,sah2,c2,qh,rho_0,rt #halo
  #perfect oblate disk + s=2 model halo of de Zeeuw et al. (1986)

  G_grav = 4.3013 * m.pow(10.,-6.)

  #this is probably a mistake
  #dG_disk_dt = m.sqrt( t - neg_gamma ) / gamma_dummy * ( 1./(1.+
   dG_disk_dt**2) - atan(dG_disk_dt) / dG_disk_dt )


  #debugging
  #print "t = {}".format(t)
  #print "gamma_dummy = {}".format(gamma_dummy)

  dG_disk_dt = m.sqrt(t-neg_gamma)/gamma_dummy
  dG_disk_dt = (G_grav*disk_mass/(m.pi*(gamma_dummy**3)*(dG_disk_dt
   **2))) * ( (1./(1.+(dG_disk_dt**2))) - (m.atan(dG_disk_dt)/
   dG_disk_dt) )

  b = sah2 - neg_alpha
  p = m.sqrt( (t-neg_gamma) / (neg_gamma+b) )
  dum1 = del2/(t-neg_gamma) * m.log( (t+b)/(neg_gamma+b) ) - (t-
   neg_gamma+del2)/(t+b)
  dum2 = (del2-neg_gamma-b)/(neg_gamma+b) * ( 1./(1.+p**2) - m.atan(
   p) / p )
  dG_halo_dt = 2.*m.pi*G_grav*rho_0 * (neg_gamma+b)/(t-neg_gamma) *
   ( dum1 + dum2 )


  dG_dt = dG_disk_dt + dG_halo_dt

  return dG_dt

#Phi(tau) for potential
#from equ. (5) in Sommer-Larsen & Zhen
def phi(lambda_,nu):

  global neg_alpha_sqrt,gamma_dummy,neg_alpha,neg_gamma,q,del2,
   disk_mass #disk

  phi = -((lambda_-neg_gamma) * G(lambda_) - (nu-neg_gamma) * G(nu))
     / (lambda_ - nu)

  return phi

#for B(tau)
#from equ. (13) in Sommer-Larsen & Zhen?
def B(t):

  global neg_alpha_sqrt,gamma_dummy,neg_alpha,neg_gamma,q,del2,
   disk_mass #disk
  global energy,I_2,I_3 #inte

  #debugging
#    print "t={}".format(t)
#    print "neg_alpha={}".format(neg_alpha)
#    print "E={}".format(energy)
#    print "neg_gamma={}".format(neg_gamma)
#    print "I2={}".format(I_2)
#    print "I3={}".format(I_3)
#    print "G(t)={}".format(G(t))

  B = - (t-neg_alpha)*(t-neg_gamma) * energy - (t-neg_gamma) * I_2 -
    (t-neg_alpha) * I_3 + (t-neg_alpha)*(t-neg_gamma) * G(t)
```

```
  return B

#for dB(tau)/dtau
def dB_dt(t):

  global neg_alpha_sqrt,gamma_dummy,neg_alpha,neg_gamma,q,del2,
   disk_mass #disk
  global energy,I_2,I_3 #inte

  dB_dt = - (2.*t-neg_alpha-neg_gamma) * energy - I_2 - I_3 + (2.*t-
   neg_alpha-neg_gamma) * G(t) + (t-neg_alpha)*(t-neg_gamma) * dG_dt
   (t)

  return dB_dt

#determine (lambda_,nu) from (R,z) (*cylindrical* coords)
#start w/ 1 = R**2/(tau+alpha) + z**2(tau+gamma)
#lambda and nu are the roots of this equation
#rearrange as A*tau**2 + B*tau + C = 0
#solve quadratic equation to get lambda and nu
def position():

  global neg_alpha_sqrt,gamma_dummy,neg_alpha,neg_gamma,q,del2,
   disk_mass #disk
  global x,y,vx,vy,r,z,vr,vz,vp,lambda_,nu,vlam,vnu #phas

  #A = 1, unneeded
  neg_B = neg_alpha + neg_gamma + r**2 + z**2
  C = neg_alpha*neg_gamma + neg_gamma*r**2 + neg_alpha*z**2
  lambda_ = 0.5 * ( neg_B + m.sqrt( neg_B**2 - 4.*C ) )
  nu  = 0.5 * ( neg_B - m.sqrt( neg_B**2 - 4.*C ) )

#determine (v_lam,v_nu) for given (vr,vz,lambda_,nu,z)
#literal black magic
def transform_velocities():

  global neg_alpha_sqrt,gamma_dummy,neg_alpha,neg_gamma,q,del2,
   disk_mass #disk
  global x,y,vx,vy,r,z,vr,vz,vp,lambda_,nu,vlam,vnu #phas

  cos_theta = (lambda_-neg_gamma)*(nu-neg_alpha)/(neg_gamma-
   neg_alpha)/(lambda_-nu)
  cos_theta = m.sqrt( cos_theta )
  sin_theta = (lambda_-neg_alpha)*(nu-neg_gamma)/(neg_alpha-
   neg_gamma)/(lambda_-nu)
  sin_theta = m.sqrt( sin_theta )

  #this is how sign funct. works in fortran
  def sign(a,b):
    c=None
    if(b>=0.):
      c = abs(a)
    elif(b<0.):
      c = -abs(a)
    return c

  vlam =   cos_theta * vr + sin_theta * sign(1.0,z) * vz
  vnu  = - sin_theta * vr + cos_theta * sign(1.0,z) * vz

#determine (E,I_2,I_3) from (v_lam,v_p,v_nu,lambda_,nu) and (v_x,v_y
   ,v_z,x,y,z,R)
def get_EI2I3():

  global neg_alpha_sqrt,gamma_dummy,neg_alpha,neg_gamma,q,del2,
   disk_mass #disk
  global x,y,vx,vy,r,z,vr,vz,vp,lambda_,nu,vlam,vnu #phas
```

```
  global energy,I_2,I_3 #inte

  #negative of the Hamiltonian, from equ. (10) & equ. (12) in Sommer
   -Larsen & Zhen
  energy = 0.5 * (vlam**2 + vp**2 + vnu**2) + phi(lambda_,nu)
  energy = - energy

  #from equ. (14) and equ. (12) in Sommer-Larsen & Zhen
  I_2  = 0.5 * ( r * vp )**2

  L_x = y * vz - z * vy
  L_y = z * vx - x * vz

  #from equ. (15) in Sommer-Larsen & Zhen
  I_3  = 0.5 * (L_x**2 + L_y**2) + del2 * ( 0.5 * vz**2 - z**2 * ( G
   (lambda_) - G(nu) )/(lambda_ - nu) )

def wrfb():

  nm = 10001

  global tau_array

  for i in range(0,nm):
    tau = tau_array[i]

    bt  = B(tau)
    bt  = bt / (10**6)
    o20.write("{},{}".format(tau,bt))


#get boundaries of orbits
def gbound():

  nm = 10001

  global tau_array
  global x,y,vx,vy,r,z,vr,vz,vp,lambda_,nu,vlam,vnu #phas
  global neg_alpha_sqrt,gamma_dummy,neg_alpha,neg_gamma,q,del2,
   disk_mass #disk
  global energy,I_2,I_3 #inte
  global atsol #boun

  global is_bound

  #at_solution?
  atsol = [None] * 3

  B_array = [None] * nm
  t_initial_array = [None] * 3

  #small numbers?
  epsilon_array = [10**(-5),10**(-3),10**(-3)]

  #(0) skip for unbounded orbits

  if(energy < 0.):
    is_bound = 0
    return
  else:
    is_bound = 1

  #(1) search three nearest solutions: t_initial_array(3)

  for i in range(0,nm):
    tau = tau_array[i]
    B_array[i] = B(tau)
```

```
    j_initial = 0

    #CHECK THIS RANGE
    for i in range(0,nm-1):

      #debugging
      #print "loop {}/{}".format(i,nm)

      dum = B_array[i] * B_array[i+1]

      #if B transitioning from + to - or from - to +
      if(dum <= 0.):
        j_initial = j_initial + 1
        if((j_initial-1)==0):
          t_initial_array[j_initial-1] = tau_array[i]
        elif((j_initial-1)==1):
          t_initial_array[j_initial-1] = tau_array[i+1]
        else:
          t_initial_array[j_initial-1] = tau_array[i+1]
        #only look for 3 transitions/"zero points"
        if((j_initial-1)==2):
          break

    #if B doesn't transition 3 times, star is unbound
    if(j_initial < 3):
      #print("failed for 3 nearest solutions\n")
      #print("  R = {}, z = {}".format(r,z))
      is_bound = 0
      return

    #(2) search 3 exact solutions by Newton method

    for j in [0,1,2]:

      t_initial = t_initial_array[j]

      #CHECK THIS RANGE
      for k in range(1,200):
        t_next = t_initial - B(t_initial) / dB_dt(t_initial)
        dum = abs(t_next - t_initial) / t_next
        if(dum < epsilon_array[j]):
          atsol[j] = t_next
          break
        else:
          if(k < 200):
            t_initial = t_next
          else:
            o6.write("failed for exact solutions, for j=".format(j))
            is_bound = 0

  #get eccentricities in the Staeckel potential
  def getecc():

    global neg_alpha_sqrt,gamma_dummy,neg_alpha,neg_gamma,q,del2,
     disk_mass #disk
    global eccentricity,elsecc,cradecc,abun #feoh
    global rmin,rmax,crmin,crmax,zeta,zmax #apoc
    global atsol #boun

    global is_bound

    #unbound
    if( is_bound <= 0. ):
      eccentricity  = -9.999
      elsecc  = -9.999
      cradecc = -9.999
```

```
    rmax = -9.999
    crmax = -9.999
    rmin = -9.999
    crmin = -9.999
    zeta = -9.999
    zmax = -9.999
    return

  nu0 = atsol[0]
  lambda_1 = atsol[1]
  lambda_2 = atsol[2]

  if(nu0 <= neg_gamma):
    #print("nu0 <= neg_gamma")
    pass

  if(nu0 >= lambda_1):
    #print("nu0 >= lambda_1")
    eccentricity  = -9.999
    elsecc  = -9.999
    cradecc = -9.999
    rmax = -9.999
    crmax = -9.999
    rmin = -9.999
    crmin = -9.999
    zeta = -9.999
    zmax = -9.999
    return

  #(1) eccentricity in r
  rmax = m.sqrt(( lambda_2 - neg_alpha ) + ( nu0 - neg_gamma ))

  try:
    rmin = m.sqrt(lambda_1 - neg_alpha)
  except:
    rmin = -9.999

  eccentricity = ( rmax - rmin ) / ( rmax + rmin )

  #(2) eccentricity in R
  crmax = m.sqrt(lambda_2 - neg_alpha)

  try:
    crmin = m.sqrt(lambda_1 - neg_alpha)
  except:
    crmin = -9.999

  cradecc = ( crmax - crmin ) / ( crmax + crmin )

  #(3) width in the nu direction
  zeta = m.sqrt( nu0 - neg_gamma )

  #this is probably a mistake
  #zmax = m.sqrt(( lambda_2 - neg_gamma ) * ( nu0 - neg_gamma ))

  zmax = m.sqrt((( lambda_2 - neg_gamma ) * ( nu0 - neg_gamma )) / (
   neg_alpha - neg_gamma))
```

A.2.3 Condor Kinematics Batch Submission

This section includes example codes for the HTCondor submission process. In this example, kinematic parameters are being derived for the Chen et al. (2014) (C14) of Chapter 5.

Three programs are required: 1) an executable that runs the kinematic pipeline program given in Section A.2.2 for small chunks of the input file (Section A.2.3.1), 2) an HTCondor submission script that, essentially, runs the executable for *all* small chunks of the input file, distributing these small jobs to multiple idle workstations across the network (Section A.2.3.2), and 3) a Python program that combines the many small output files, which must be manually run by the user once all HTCondor jobs have completed (Section A.2.3.3).

A.2.3.1 executable_chen14.sh

```
#!/bin/bash

job_num=$1 #job number currently being processed
input_file="chen14_kin_input_v2.csv" #input file to process
main_dir="chen14" #name of dir to store files in
main_name="chen14_unc" #name-tag to assign to output files
num_per=2 #stars to process per job
base_add=0 #num jobs prev submitted (if multiple submit files needed
    )

start=$(echo "$num_per*($job_num+$base_add)" | bc) #first star to
    run this job
stop=$(echo "$start+$num_per" | bc) #last star to run this job

condor_base=/afs/crc.nd.edu/user/s/sdietz/condor_stuff/

#make new dir for every 1000 files
dir_num=$(echo "($job_num+$base_add)/1000./1" | bc)
dir_name="${main_dir}/runs_$dir_num/"

file_num=$(echo "$job_num+$base_add" | bc)
file_name="${main_name}_run_$file_num" #where to store kin output

#save stuff in a temporary dir (transfer at end)
tmp_dir=$(/usr/bin/mktemp -d)
tmp_save_dir="$tmp_dir/$dir_name"
mkdir -p $tmp_save_dir

module load python/2.7.14

# Copy necessary files over for local processing (/tmp)
cp ${condor_base}/dietz_mini_pipeline_v1.py ${tmp_dir}
cp ${condor_base}/${input_file} ${tmp_dir}
cp ${condor_base}/staeckel_orbit.py ${tmp_dir}

# Begin local processing
cd ${tmp_dir}

python dietz_mini_pipeline_v1.py $input_file $file_name
    $tmp_save_dir $start \
     $stop

# Copy over tmp_dir results into AFS
cp -r ${tmp_save_dir}/ ${condor_base}/${main_dir}/
```

```
# cleanup tmp_dir
cd -
rm -rf $tmp_dir
```

A.2.3.2 chen14.submit

```
universe                 = vanilla
executable               = /afs/crc.nd.edu/user/s/sdietz/condor_stuff
   /executable_chen14.sh
arguments                = $(PROCESS)
getenv                   = True
error                    = /afs/crc.nd.edu/user/s/sdietz/condor_stuff
   /chen14/err_files/run_$(PROCESS).error
should_transfer_files    = yes
when_to_transfer_output = on_exit
request_memory           = 4 GB
queue 7862
```

A.2.3.3 combine_chen14.py

```
import math as m
import numpy as np
import os.path

main_dir="chen14"
main_name="chen14_unc"

#how many total files (num jobs ran)
last_file=7862

dir_lim=int(m.ceil(last_file/1000.))

#final file to write to
o=open("{}/{}_kin.csv".format(main_dir,main_name),"a")

first_file=True

start=0
stop=0

for run_dir in range(0,dir_lim):
#each directory as 1000 sub-directories...
  start=stop
  stop=start+1000

  if(run_dir==dir_lim-1):
    stop=last_file

  for run in range(start,stop):
    file_exists=True
    file_empty=False
    kin_dir="{}/runs_{}/{}_run_{}_kin".format(main_dir,run_dir,
   main_name,run)
    kin_file="{}/{}_run_{}_kin.csv".format(kin_dir,main_name,run)

    if(first_file==True):
      for line in open(kin_file):
        o.write(line)
        first_file=False
    #don't want to copy the header for each subsequent file
    else:
      try:
        f=open(kin_file)
      except:
```

```
        file_exists=False
      if(file_exists==True):
        try:
          f.next() #skip header
        except:
          file_empty=True
        if(file_empty==False):
          for line in f:
            o.write(line)
          f.close()
        else:
          print "file empty: {}".format(kin_file)
      else:
        print "file doesn't exist: {}".format(kin_file)

o.close()
```

A.2.4 “IOT” Designation

```
#initialize dicts
CEMP_s={"I":0,"O":0,"T":0,"U":0}
CEMP_no={"I":0,"O":0,"T":0,"U":0}

#CEMP criteria
cemp_s_case=np.where(a1['SUBCLASS']=='CEMP-s')[0]
cemp_no_case=np.where(a1['SUBCLASS']=='CEMP-no')[0]

#include relevant kinematic criteria
cemp_s_case=reduce(np.intersect1d,(no_disk,rv_crit,orb_case,
   cemp_s_case))
cemp_no_case=reduce(np.intersect1d,(no_disk,rv_crit,orb_case,
   cemp_no_case))

print '{} CEMP-s'.format(len(cemp_s_case))
print '{} CEMP-no\n'.format(len(cemp_no_case))

for row in range(0,len(a1)):
  r_apo=a1[row]['R_APO']
  E=a1[row]['ENERGY']/(10.**5.) #scale energy for convenience
  if((row in cemp_s_case) or (row in cemp_no_case)):
    if((r_apo < 15) or ((r_apo > 15) & (E < -1.1))): #designation: I
      if(row in cemp_s_case):
        CEMP_s["I"]+=1
      elif(row in cemp_no_case):
        CEMP_no["I"]+=1
    elif((r_apo > 15) & (E > -0.8)): #designation: O
      if(row in cemp_s_case):
        CEMP_s["O"]+=1
      elif(row in cemp_no_case):
        CEMP_no["O"]+=1
    elif((r_apo > 15) & (E < -0.8) & (E > -1.1)): #designation: T
      if(row in cemp_s_case):
        CEMP_s["T"]+=1
      elif(row in cemp_no_case):
        CEMP_no["T"]+=1
    else: #designation: U (undefined/unbound)
      if(row in cemp_s_case):
        CEMP_s["U"]+=1
      elif(row in cemp_no_case):
        CEMP_no["T"]+=1

  else:
    pass
```

```
#calculate percentages, print results

I=CEMP_s['I']
tot=CEMP_s['I']+CEMP_no['I']
I_perc=100.*I/float(tot)
I_perc_s=round(I_perc,2)

O=CEMP_s['O']
tot=CEMP_s['O']+CEMP_no['O']
O_perc=100.*O/float(tot)
O_perc_s=round(O_perc,2)

T=CEMP_s['T']
tot=CEMP_s['T']+CEMP_no['T']
T_perc=100.*T/float(tot)
T_perc_s=round(T_perc,2)

print 'CEMP-s: I {} ({}%), O {} ({}%), T {} ({}%)'.format(I,I_perc_s
    ,O,O_perc_s,T,T_perc_s)

I=CEMP_no['I']
tot=CEMP_s['I']+CEMP_no['I']
I_perc=100.*I/float(tot)
I_perc_no=round(I_perc,2)

O=CEMP_no['O']
tot=CEMP_s['O']+CEMP_no['O']
O_perc=100.*O/float(tot)
O_perc_no=round(O_perc,2)

T=CEMP_no['T']
tot=CEMP_s['T']+CEMP_no['T']
T_perc=100.*T/float(tot)
T_perc_no=round(T_perc,2)

print 'CEMP-no: I {} ({}%), O {} ({}%), T {} ({}%)'.format(I,
    I_perc_no,O,O_perc_no,T,T_perc_no)
```

BIBLIOGRAPHY

D. S. Aguado, R. Ahumada, A. Almeida, S. F. Anderson, B. H. Andrews, B. Anguiano, E. Aquino Ortíz, A. Aragón-Salamanca, M. Argudo-Fernández, and M. Aubert. The Fifteenth Data Release of the Sloan Digital Sky Surveys: First Release of MaNGA-derived Quantities, Data Visualization Tools, and Stellar Library. *ApJS*, 240(2):23, Feb 2019a. doi: 10.3847/1538-4365/aaf651.

D. S. Aguado, K. Youakim, J. I. González Hernández, C. Allende Prieto, E. Starkenburg, N. Martin, P. Bonifacio, A. Arentsen, E. Caffau, L. Peralta de Arriba, F. Sestito, R. Garcia-Dias, N. Fantin, V. Hill, P. Jablonca, F. Jahandar, C. Kielty, N. Longeard, R. Lucchesi, R. Sánchez-Janssen, Y. Osorio, P. A. Palicio, E. Tolstoy, T. G. Wilson, P. Côté, G. Kordopatis, C. Lardo, J. F. Navarro, G. F. Thomas, and K. Venn. The Pristine survey - VI. The first three years of medium-resolution follow-up spectroscopy of Pristine EMP star candidates. *MNRAS*, 490(2):2241–2253, Dec. 2019b. doi: 10.1093/mnras/stz2643.

C. P. Ahn, R. Alexandroff, C. Allende Prieto, S. F. Anderson, T. Anderton, B. H. Andrews, É. Aubourg, S. Bailey, E. Balbinot, R. Barnes, J. Bautista, T. C. Beers, A. Beifiori, A. A. Berlind, V. Bhardwaj, D. Bizyaev, C. H. Blake, M. R. Blanton, M. Blomqvist, J. J. Bochanski, A. S. Bolton, A. Borde, J. Bovy, W. N. Brandt, J. Brinkmann, P. J. Brown, J. R. Brownstein, K. Bundy, N. G. Busca, W. Carithers, A. R. Carnero, M. A. Carr, D. I. Casetti-Dinescu, Y. Chen, C. Chiappini, J. Comparat, N. Connolly, J. R. Crepp, S. Cristiani, R. A. C. Croft, A. J. Cuesta, L. N. da Costa, J. R. A. Davenport, K. S. Dawson, R. de Putter, N. De Lee, T. Delubac, S. Dhital, A. Ealet, G. L. Ebelke, E. M. Edmondson, D. J. Eisenstein, S. Escoffier, M. Esposito, M. L. Evans, X. Fan, B. Femenía Castellá, E. Fernández Alvar, L. D. Ferreira, N. Filiz Ak, H. Finley, S. W. Fleming, A. Font-Ribera, P. M. Frinchaboy, D. A. García-Hernández, A. E. García Pérez, J. Ge, R. Génova-Santos, B. A. Gillespie, L. Girardi, J. I. González Hernández, E. K. Grebel, J. E. Gunn, H. Guo, D. Haggard, J.-C. Hamilton, D. W. Harris, S. L. Hawley, F. R. Hearty, S. Ho, D. W. Hogg, J. A. Holtzman, K. Honscheid, J. Huehnerhoff, I. I. Ivans, Ž. Ivezić, H. R. Jacobson, L. Jiang, J. Johansson, J. A. Johnson, G. Kauffmann, D. Kirkby, J. A. Kirkpatrick, M. A. Klaene, G. R. Knapp, J.-P. Kneib, J.-M. Le Goff, A. Leauthaud, K.-G. Lee, Y. S. Lee, D. C. Long, C. P. Loomis, S. Lucatello, B. Lundgren, R. H. Lupton, B. Ma, Z. Ma, N. MacDonald, C. E. Mack, S. Mahadevan, M. A. G. Maia, S. R. Majewski, M. Makler, E. Malanushenko, V. Malanushenko, A. Manchado, R. Mandelbaum, M. Manera, C. Maraston, D. Margala, S. L. Martell, C. K.

McBride, I. D. McGreer, R. G. McMahon, B. Ménard, S. Meszaros, J. Miralda-Escudé, A. D. Montero-Dorta, F. Montesano, H. L. Morrison, D. Muna, J. A. Munn, H. Murayama, A. D. Myers, A. F. Neto, D. C. Nguyen, R. C. Nichol, D. L. Nidever, P. Noterdaeme, S. E. Nuza, R. L. C. Ogand o, M. D. Olmstead, D. J. Oravetz, R. Owen, N. Padmanabhan, N. Palanque-Delabrouille, K. Pan, J. K. Parejko, P. Parihar, I. Pâris, P. Pattarakijwanich, J. Pepper, W. J. Percival, I. Pérez-Fournon, I. Pérez-Ràfols, P. Petitjean, J. Pforr, M. M. Pieri, M. H. Pinsonneault, G. F. Porto de Mello, F. Prada, A. M. Price-Whelan, M. J. Raddick, R. Rebolo, J. Rich, G. T. Richards, A. C. Robin, H. J. Rocha-Pinto, C. M. Rockosi, N. A. Roe, A. J. Ross, N. P. Ross, G. Rossi, J. A. Rubiño-Martin, L. Samushia, J Sanchez Almeida, A. G. Sánchez, B. Santiago, C. Sayres, D. J. Schlegel, K. J. Schlesinger, S. J. Schmidt, D. P. Schneider, M. Schultheis, A. D. Schwope, C. G. Scóccola, U. Seljak, E. Sheldon, Y. Shen, Y. Shu, J. Simmerer, A. E. Simmons, R. A. Skibba, M. F. Skrutskie, A. Slosar, F. Sobreira, J. S. Sobeck, K. G. Stassun, O. Steele, M. Steinmetz, M. A. Strauss, A. Streblyanska, N. Suzuki, M. E. C. Swanson, T. Tal, A. R. Thakar, D. Thomas, B. A. Thompson, J. L. Tinker, R. Tojeiro, C. A. Tremonti, M. Vargas Magaña, L. Verde, M. Viel, S. K. Vikas, N. P. Vogt, D. A. Wake, J. Wang, B. A. Weaver, D. H. Weinberg, B. J. Weiner, A. A. West, M. White, J. C. Wilson, J. P. Wisniewski, W. M. Wood-Vasey, B. Yanny, C. Yèche, D. G. York, O. Zamora, G. Zasowski, I. Zehavi, G.-B. Zhao, Z. Zheng, G. Zhu, and J. C. Zinn. The Ninth Data Release of the Sloan Digital Sky Survey: First Spectroscopic Data from the SDSS-III Baryon Oscillation Spectroscopic Survey. *ApJS*, 203(2):21, Dec 2012. doi: 10.1088/0067-0049/203/2/21.

N. C. Amorisco. Contributions to the accreted stellar halo: an atlas of stellar deposition. *MNRAS*, 464(3):2882–2895, Jan 2017. doi: 10.1093/mnras/stw2229.

D. An and T. C. Beers. A Blueprint for the Milky Way's Stellar Populations: The Power of Large Photometric and Astrometric Surveys. *arXiv e-prints*, art. arXiv:1912.06847, Dec. 2019.

D. An, T. C. Beers, J. A. Johnson, M. H. Pinsonneault, Y. S. Lee, J. Bovy, Ž. Ivezić, D. Carollo, and M. Newby. The Stellar Metallicity Distribution Function of the Galactic Halo from SDSS Photometry. *ApJ*, 763(1):65, Jan 2013. doi: 10.1088/0004-637X/763/1/65.

C. A. L. Bailer-Jones, J. Rybizki, M. Fouesneau, G. Mantelet, and R. Andrae. Estimating Distance from Parallaxes. IV. Distances to 1.33 Billion Stars in Gaia Data Release 2. *AJ*, 156(2):58, Aug 2018. doi: 10.3847/1538-3881/aacb21.

T. C. Beers and N. Christlieb. The Discovery and Analysis of Very Metal-Poor Stars in the Galaxy. *ARA&A*, 43(1):531–580, Sep 2005. doi: 10.1146/annurev.astro.42.053102.134057.

T. C. Beers, M. Chiba, Y. Yoshii, I. Platais, R. B. Hanson, B. Fuchs, and S. Rossi. Kinematics of Metal-poor Stars in the Galaxy. II. Proper Motions for a Large

Nonkinematically Selected Sample. *AJ*, 119(6):2866–2881, Jun 2000. doi: 10.1086/301410.

T. C. Beers, D. Carollo, Ž. Ivezić, D. An, M. Chiba, J. E. Norris, K. C. Freeman, Y. S. Lee, J. A. Munn, and P. Re Fiorentin. The Case for the Dual Halo of the Milky Way. *ApJ*, 746(1):34, Feb 2012. doi: 10.1088/0004-637X/746/1/34.

T. C. Beers, J. E. Norris, V. M. Placco, Y. S. Lee, S. Rossi, D. Carollo, and T. Masseron. Population Studies. XIII. A New Analysis of the Bidelman-MacConnell "Weak-metal" Stars—Confirmation of Metal-poor Stars in the Thick Disk of the Galaxy. *ApJ*, 794(1):58, Oct 2014. doi: 10.1088/0004-637X/794/1/58.

T. C. Beers, V. M. Placco, D. Carollo, S. Rossi, Y. S. Lee, A. Frebel, J. E. Norris, S. Dietz, and T. Masseron. Bright Metal-Poor Stars from the Hamburg/ESO Survey. II. A Chemodynamical Analysis. *ApJ*, 835(1):81, Jan. 2017. doi: 10.3847/1538-4357/835/1/81.

V. Belokurov, N. W. Evans, E. F. Bell, M. J. Irwin, P. C. Hewett, S. Koposov, C. M. Rockosi, G. Gilmore, D. B. Zucker, M. Fellhauer, M. I. Wilkinson, D. M. Bramich, S. Vidrih, H. W. Rix, T. C. Beers, D. P. Schneider, J. C. Barentine, H. Brewington, J. Brinkmann, M. Harvanek, J. Krzesinski, D. Long, K. Pan, S. A. Snedden, O. Malanushenko, and V. Malanushenko. The Hercules-Aquila Cloud. *ApJL*, 657(2):L89–L92, Mar 2007a. doi: 10.1086/513144.

V. Belokurov, N. W. Evans, M. J. Irwin, D. Lynden-Bell, B. Yanny, S. Vidrih, G. Gilmore, G. Seabroke, D. B. Zucker, M. I. Wilkinson, P. C. Hewett, D. M. Bramich, M. Fellhauer, H. J. Newberg, R. F. G. Wyse, T. C. Beers, E. F. Bell, J. C. Barentine, J. Brinkmann, N. Cole, K. Pan, and D. G. York. An Orphan in the "Field of Streams". *ApJ*, 658(1):337–344, Mar 2007b. doi: 10.1086/511302.

V. Belokurov, D. Erkal, N. W. Evans, S. E. Koposov, and A. J. Deason. Co-formation of the disc and the stellar halo. *MNRAS*, 478(1):611–619, Jul 2018. doi: 10.1093/mnras/sty982.

V. Belokurov, J. L. Sanders, A. Fattahi, M. C. Smith, A. J. Deason, N. W. Evans, and R. J. J. Grand . The biggest Splash. *MNRAS*, Apr. 2020. doi: 10.1093/mnras/staa876.

J. Bland-Hawthorn and O. Gerhard. The Galaxy in Context: Structural, Kinematic, and Integrated Properties. *ARA&A*, 54:529–596, Sept. 2016. doi: 10.1146/annurev-astro-081915-023441.

P. Bonifacio, J. Andersen, S. M. Andrievsky, B. Barbuy, T. C. Beers, E. Caffau, R. Cayrel, E. Depagne, P. François, J. I. González Hernández, and et al. The eso large programme "first stars". *Science with the VLT in the ELT Era*, page 31–35, 2009. ISSN 1570-6605. doi: 10.1007/978-1-4020-9190-2_6. URL `http://dx.doi.org/10.1007/978-1-4020-9190-2_6`.

J. Bovy. galpy: A python Library for Galactic Dynamics. *ApJS*, 216:29, Feb. 2015. doi: 10.1088/0067-0049/216/2/29.

S. Buder, M. Asplund, L. Duong, J. Kos, K. Lind, M. K. Ness, S. Sharma, J. Bland -Hawthorn, A. R. Casey, G. M. de Silva, V. D'Orazi, K. C. Freeman, G. F. Lewis, J. Lin, S. L. Martell, K. J. Schlesinger, J. D. Simpson, D. B. Zucker, T. Zwitter, A. M. Amarsi, B. Anguiano, D. Carollo, L. Casagrande, K. Čotar, P. L. Cottrell, G. da Costa, X. D. Gao, M. R. Hayden, J. Horner, M. J. Ireland, P. R. Kafle, U. Munari, D. M. Nataf, T. Nordlander, D. Stello, Y.-S. Ting, G. Traven, F. Watson, R. A. Wittenmyer, R. F. G. Wyse, D. Yong, J. C. Zinn, M. Žerjal, and Galah Collaboration. The GALAH Survey: second data release. *MNRAS*, 478(4):4513–4552, Aug 2018. doi: 10.1093/mnras/sty1281.

F. Caputo and V. Castellani. The survival of galactic globular clusters. *MNRAS*, 207:185–191, Mar. 1984. doi: 10.1093/mnras/207.2.185.

B. W. Carney. Probing the outer galactic halo. *PASP*, 96:841–855, Nov. 1984. doi: 10.1086/131443.

D. Carollo, T. C. Beers, Y. S. Lee, M. Chiba, J. E. Norris, R. Wilhelm, T. Sivarani, B. Marsteller, J. A. Munn, C. A. L. Bailer-Jones, P. R. Fiorentin, and D. G. York. Two stellar components in the halo of the Milky Way. *Nature*, 450(7172):1020–1025, Dec 2007. doi: 10.1038/nature06460.

D. Carollo, T. C. Beers, M. Chiba, J. E. Norris, K. C. Freeman, Y. S. Lee, Ž. Ivezić, C. M. Rockosi, and B. Yanny. Structure and Kinematics of the Stellar Halos and Thick Disks of the Milky Way Based on Calibration Stars from Sloan Digital Sky Survey DR7. *ApJ*, 712(1):692–727, Mar. 2010. doi: 10.1088/0004-637X/712/1/692.

D. Carollo, K. Freeman, T. C. Beers, V. M. Placco, J. Tumlinson, and S. L. Martell. Carbon-enhanced Metal-poor Stars: CEMP-s and CEMP-no Subclasses in the Halo System of the Milky Way. *ApJ*, 788(2):180, Jun 2014. doi: 10.1088/0004-637X/788/2/180.

D. Carollo, M. Chiba, M. Ishigaki, K. Freeman, T. C. Beers, Y. S. Lee, P. Tissera, C. Battistini, and F. Primas. Evidence for the Third Stellar Population in the Milky Way's Disk. *ApJ*, 887(1):22, Dec. 2019. doi: 10.3847/1538-4357/ab517c.

J. W. Chamberlain and L. H. Aller. The Atmospheres of A-Type Subdwarfs and 95 Leonis. *ApJ*, 114:52, July 1951. doi: 10.1086/145451.

Y. Q. Chen, G. Zhao, K. Carrell, J. K. Zhao, K. F. Tan, P. E. Nissen, and P. Wei. Red Giant Stars from Sloan Digital Sky Survey. I. The General Field. *ApJ*, 795(1): 52, Nov 2014. doi: 10.1088/0004-637X/795/1/52.

G. Chiaki, N. Tominaga, and T. Nozawa. Classification of extremely metal-poor stars: absent region in A(C)-[Fe/H] plane and the role of dust cooling. *MNRAS*, 472(1): L115–L119, Nov. 2017. doi: 10.1093/mnrasl/slx163.

C. Chiappini. The Formation and Evolution of the Milky Way. *American Scientist*, 89(6):506, Dec. 2001. doi: 10.1511/2001.6.506.

M. Chiba and T. C. Beers. Kinematics of Metal-poor Stars in the Galaxy. III. Formation of the Stellar Halo and Thick Disk as Revealed from a Large Sample of Nonkinematically Selected Stars. *AJ*, 119(6):2843–2865, Jun 2000. doi: 10.1086/301409.

C. Conroy, A. Bonaca, P. Cargile, B. D. Johnson, N. Caldwell, R. P. Naidu, D. Zaritsky, D. Fabricant, S. Moran, J. Rhee, A. Szentgyorgyi, P. Berlind, M. L. Calkins, S. Kattner, and C. Ly. Mapping the Stellar Halo with the H3 Spectroscopic Survey. *ApJ*, 883(1):107, Sep 2019a. doi: 10.3847/1538-4357/ab38b8.

C. Conroy, R. P. Naidu, D. Zaritsky, A. Bonaca, P. Cargile, B. D. Johnson, and N. Caldwell. Resolving the Metallicity Distribution of the Stellar Halo with the H3 Survey. *arXiv e-prints*, art. arXiv:1909.02007, Sep 2019b.

G. Cordoni, G. S. Da Costa, D. Yong, A. D. Mackey, A. F. Marino, S. Monty, T. Nordlander, J. E. Norris, M. Asplund, M. S. Bessell, A. R. Casey, A. Frebel, K. Lind, S. J. Murphy, B. P. Schmidt, X. D. Gao, T. Xylakis-Dornbusch, A. M. Amarsi, and A. P. Milone. Exploring the Galaxy's halo and very metal-weak thick disk with SkyMapper and Gaia DR2. *MNRAS*, Nov. 2020. doi: 10.1093/mnras/staa3417.

X.-Q. Cui, Y.-H. Zhao, Y.-Q. Chu, G.-P. Li, Q. Li, L.-P. Zhang, H.-J. Su, Z.-Q. Yao, Y.-N. Wang, X.-Z. Xing, X.-N. Li, Y.-T. Zhu, G. Wang, B.-Z. Gu, A. L. Luo, X.-Q. Xu, Z.-C. Zhang, G.-R. Liu, H.-T. Zhang, D.-H. Yang, S.-Y. Cao, H.-Y. Chen, J.-J. Chen, K.-X. Chen, Y. Chen, J.-R. Chu, L. Feng, X.-F. Gong, Y.-H. Hou, H.-Z. Hu, N.-S. Hu, Z.-W. Hu, L. Jia, F.-H. Jiang, X. Jiang, Z.-B. Jiang, G. Jin, A.-H. Li, Y. Li, Y.-P. Li, G.-Q. Liu, Z.-G. Liu, W.-Z. Lu, Y.-D. Mao, L. Men, Y.-J. Qi, Z.-X. Qi, H.-M. Shi, Z.-H. Tang, Q.-S. Tao, D.-Q. Wang, D. Wang, G.-M. Wang, H. Wang, J.-N. Wang, J. Wang, J.-L. Wang, J.-P. Wang, L. Wang, S.-Q. Wang, Y. Wang, Y.-F. Wang, L.-Z. Xu, Y. Xu, S.-H. Yang, Y. Yu, H. Yuan, X.-Y. Yuan, C. Zhai, J. Zhang, Y.-X. Zhang, Y. Zhang, M. Zhao, F. Zhou, G.-H. Zhou, J. Zhu, and S.-C. Zou. The Large Sky Area Multi-Object Fiber Spectroscopic Telescope (LAMOST). *Research in Astronomy and Astrophysics*, 12(9):1197–1242, Sep 2012. doi: 10.1088/1674-4527/12/9/003.

G. Dalton, S. Trager, D. C. Abrams, P. Bonifacio, J. A. López Aguerri, K. Middleton, C. Benn, K. Dee, F. Sayède, I. Lewis, J. Pragt, S. Pico, N. Walton, J. Rey, C. Allende Prieto, J. Peñate, E. Lhome, T. Agócs, J. Alonso, D. Terrett, M. Brock, J. Gilbert, A. Ridings, I. Guinouard, M. Verheijen, I. Tosh, K. Rogers, I. Steele, R. Stuik, N. Tromp, A. Jasko, J. Kragt, D. Lesman, C. Mottram, S. Bates, F. Gribbin, L. Fernand o Rodriguez, J. M. Delgado, C. Martin, D. Cano, R. Navarro, M. Irwin, J. Lewis, E. Gonzalez Solares, N. O'Mahony, A. Bianco, C. Zurita, R. ter Horst, E. Molinari, M. Lodi, J. Guerra, A. Vallenari, and A. Baruffolo. *Project overview and update on WEAVE: the next generation wide-field spectroscopy facility for the William Herschel Telescope*, volume 9147 of *Society of Photo-Optical*

Instrumentation Engineers (SPIE) Conference Series, page 91470L. SPIE, 2014. doi: 10.1117/12.2055132.

K. S. Dawson, D. J. Schlegel, C. P. Ahn, S. F. Anderson, É. Aubourg, S. Bailey, R. H. Barkhouser, J. E. Bautista, A. r. Beifiori, A. A. Berlind, V. Bhardwaj, D. Bizyaev, C. H. Blake, M. R. Blanton, M. Blomqvist, A. S. Bolton, A. Borde, J. Bovy, W. N. Brandt, H. Brewington, J. Brinkmann, P. J. Brown, J. R. Brownstein, K. Bundy, N. G. Busca, W. Carithers, A. R. Carnero, M. A. Carr, Y. Chen, J. Comparat, N. Connolly, F. Cope, R. A. C. Croft, A. J. Cuesta, L. N. da Costa, J. R. A. Davenport, T. Delubac, R. de Putter, S. Dhital, A. Ealet, G. L. Ebelke, D. J. Eisenstein, S. Escoffier, X. Fan, N. Filiz Ak, H. Finley, A. Font-Ribera, R. Génova-Santos, J. E. Gunn, H. Guo, D. Haggard, P. B. Hall, J.-C. Hamilton, B. Harris, D. W. Harris, S. Ho, D. W. Hogg, D. Holder, K. Honscheid, J. Huehnerhoff, B. Jordan, W. P. Jordan, G. Kauffmann, E. A. Kazin, D. Kirkby, M. A. Klaene, J.-P. Kneib, J.-M. Le Goff, K.-G. Lee, D. C. Long, C. P. Loomis, B. Lundgren, R. H. Lupton, M. A. G. Maia, M. Makler, E. Malanushenko, V. Malanushenko, R. Mandelbaum, M. Manera, C. Maraston, D. Margala, K. L. Masters, C. K. McBride, P. McDonald, I. D. McGreer, R. G. McMahon, O. Mena, J. Miralda-Escudé, A. D. Montero-Dorta, F. Montesano, D. Muna, A. D. Myers, T. Naugle, R. C. Nichol, P. Noterdaeme, S. E. Nuza, M. D. Olmstead, A. Oravetz, D. J. Oravetz, R. Owen, N. Padmanabhan, N. Palanque-Delabrouille, K. Pan, J. K. Parejko, I. Pâris, W. J. Percival, I. Pérez-Fournon, I. Pérez-Ràfols, P. Petitjean, R. Pfaffenberger, J. Pforr, M. M. Pieri, F. Prada, A. M. Price-Whelan, M. J. Raddick, R. Rebolo, J. Rich, G. T. Richards, C. M. Rockosi, N. A. Roe, A. J. Ross, N. P. Ross, G. Rossi, J. A. Rubiño-Martin, L. Samushia, A. G. Sánchez, C. Sayres, S. J. Schmidt, D. P. Schneider, C. G. Scóccola, H.-J. Seo, A. Shelden, E. Sheldon, Y. Shen, Y. Shu, A. Slosar, S. A. Smee, S. A. Snedden, F. Stauffer, O. Steele, M. A. Strauss, A. Streblyanska, N. Suzuki, M. E. C. Swanson, T. Tal, M. Tanaka, D. Thomas, J. L. Tinker, R. Tojeiro, C. A. Tremonti, M. Vargas Magaña, L. Verde, M. Viel, D. A. Wake, M. Watson, B. A. Weaver, D. H. Weinberg, B. J. Weiner, A. A. West, M. White, W. M. Wood-Vasey, C. Yeche, I. Zehavi, G.-B. Zhao, and Z. Zheng. The Baryon Oscillation Spectroscopic Survey of SDSS-III. *AJ*, 145(1): 10, Jan 2013. doi: 10.1088/0004-6256/145/1/10.

J. T. A. de Jong, B. Yanny, H.-W. Rix, A. E. Dolphin, N. F. Martin, and T. C. Beers. Mapping the Stellar Structure of the Milky Way Thick Disk and Halo Using SEGUE Photometry. *ApJ*, 714(1):663–674, May 2010. doi: 10.1088/0004-637X/714/1/663.

P. T. de Zeeuw and D. Lynden-Bell. Best approximate quadratic integrals in stellar dynamics. *MNRAS*, 215:713–730, Aug. 1985. doi: 10.1093/mnras/215.4.713.

H. Dejonghe and T. de Zeeuw. Analytic Axisymmetric Galaxy Models with Three Integrals of Motion. *ApJ*, 333:90, Oct. 1988. doi: 10.1086/166727.

DESI Collaboration, A. Aghamousa, J. Aguilar, S. Ahlen, S. Alam, L. E. Allen, C. Allende Prieto, J. Annis, S. Bailey, C. Balland, O. Ballester, C. Baltay, L. Beaufore, C. Bebek, T. C. Beers, E. F. Bell, J. L. Bernal, R. Besuner, F. Beutler,

C. Blake, H. Bleuler, M. Blomqvist, R. Blum, A. S. Bolton, C. Briceno, D. Brooks, J. R. Brownstein, E. Buckley-Geer, A. Burden, E. Burtin, N. G. Busca, R. N. Cahn, Y.-C. Cai, L. Cardiel-Sas, R. G. Carlberg, P.-H. Carton, R. Casas, F. J. Castand er, J. L. Cervantes-Cota, T. M. Claybaugh, M. Close, C. T. Coker, S. Cole, J. Comparat, A. P. Cooper, M. C. Cousinou, M. Crocce, J.-G. Cuby, D. P. Cunningham, T. M. Davis, K. S. Dawson, A. de la Macorra, J. De Vicente, T. Delubac, M. Derwent, A. Dey, G. Dhungana, Z. Ding, P. Doel, Y. T. Duan, A. Ealet, J. Edelstein, S. Eftekharzadeh, D. J. Eisenstein, A. Elliott, S. Escoffier, M. Evatt, P. Fagrelius, X. Fan, K. Fanning, A. Farahi, J. Farihi, G. Favole, Y. Feng, E. Fernandez, J. R. Findlay, D. P. Finkbeiner, M. J. Fitzpatrick, B. Flaugher, S. Flender, A. Font-Ribera, J. E. Forero-Romero, P. Fosalba, C. S. Frenk, M. Fumagalli, B. T. Gaensicke, G. Gallo, J. Garcia-Bellido, E. Gaztanaga, N. Pietro Gentile Fusillo, T. Gerard, I. Gershkovich, T. Giannantonio, D. Gillet, G. Gonzalez-de-Rivera, V. Gonzalez-Perez, S. Gott, O. Graur, G. Gutierrez, J. Guy, S. Habib, H. Heetderks, I. Heetderks, K. Heitmann, W. A. Hellwing, D. A. Herrera, S. Ho, S. Holland, K. Honscheid, E. Huff, T. A. Hutchinson, D. Huterer, H. S. Hwang, J. M. Illa Laguna, Y. Ishikawa, D. Jacobs, N. Jeffrey, P. Jelinsky, E. Jennings, L. Jiang, J. Jimenez, J. Johnson, R. Joyce, E. Jullo, S. Juneau, S. Kama, A. Karcher, S. Karkar, R. Kehoe, N. Kennamer, S. Kent, M. Kilbinger, A. G. Kim, D. Kirkby, T. Kisner, E. Kitanidis, J.-P. Kneib, S. Koposov, E. Kovacs, K. Koyama, A. Kremin, R. Kron, L. Kronig, A. Kueter-Young, C. G. Lacey, R. Lafever, O. Lahav, A. Lambert, M. Lampton, M. Land riau, D. Lang, T. R. Lauer, J.-M. Le Goff, L. Le Guillou, A. Le Van Suu, J. H. Lee, S.-J. Lee, D. Leitner, M. Lesser, M. E. Levi, B. L'Huillier, B. Li, M. Liang, H. Lin, E. Linder, S. R. Loebman, Z. Lukić, J. Ma, N. MacCrann, C. Magneville, L. Makarem, M. Manera, C. J. Manser, R. Marshall, P. Martini, R. Massey, T. Matheson, J. McCauley, P. McDonald, I. D. McGreer, A. Meisner, N. Metcalfe, T. N. Miller, R. Miquel, J. Moustakas, A. Myers, M. Naik, J. A. Newman, R. C. Nichol, A. Nicola, L. Nicolati da Costa, J. Nie, G. Niz, P. Norberg, B. Nord, D. Norman, P. Nugent, T. O'Brien, M. Oh, K. A. G. Olsen, C. Padilla, H. Padmanabhan, N. Padmanabhan, N. Palanque-Delabrouille, A. Palmese, D. Pappalardo, I. Pâris, C. Park, A. Patej, J. A. Peacock, H. V. Peiris, X. Peng, W. J. Percival, S. Perruchot, M. M. Pieri, R. Pogge, J. E. Pollack, C. Poppett, F. Prada, A. Prakash, R. G. Probst, D. Rabinowitz, A. Raichoor, C. H. Ree, A. Refregier, X. Regal, B. Reid, K. Reil, M. Rezaie, C. M. Rockosi, N. Roe, S. Ronayette, A. Roodman, A. J. Ross, N. P. Ross, G. Rossi, E. Rozo, V. Ruhlmann-Kleider, E. S. Rykoff, C. Sabiu, L. Samushia, E. Sanchez, J. Sanchez, D. J. Schlegel, M. Schneider, M. Schubnell, A. Secroun, U. Seljak, H.-J. Seo, S. Serrano, A. Shafieloo, H. Shan, R. Sharples, M. J. Sholl, W. V. Shourt, J. H. Silber, D. R. Silva, M. M. Sirk, A. Slosar, A. Smith, G. F. Smoot, D. Som, Y.-S. Song, D. Sprayberry, R. Staten, A. Stefanik, G. Tarle, S. Sien Tie, J. L. Tinker, R. Tojeiro, F. Valdes, O. Valenzuela, M. Valluri, M. Vargas-Magana, L. Verde, A. R. Walker, J. Wang, Y. Wang, B. A. Weaver, C. Weaverdyck, R. H. Wechsler, D. H. Weinberg, M. White, Q. Yang, C. Yeche, T. Zhang, G.-B. Zhao, Y. Zheng, X. Zhou, Z. Zhou, Y. Zhu, H. Zou, and Y. Zu. The DESI Experiment Part I: Science,Targeting, and Survey Design. *arXiv e-prints*, art. arXiv:1611.00036, Oct

2016.

P. Di Matteo, M. Spite, M. Haywood, P. Bonifacio, A. Gómez, F. Spite, and E. Caffau. Reviving old controversies: is the early Galaxy flat or round?. Investigations into the early phases of the Milky Way's formation through stellar kinematics and chemical abundances. *A&A*, 636:A115, Apr. 2020. doi: 10.1051/0004-6361/201937016.

S. E. Dietz, J. Yoon, T. C. Beers, and V. M. Placco. The Metallicity Gradient and Complex Formation History of the Outermost Halo of the Milky Way. *ApJ*, 894 (1):34, May 2020. doi: 10.3847/1538-4357/ab7fa4.

O. J. Eggen, D. Lynden-Bell, and A. R. Sandage. Evidence from the motions of old stars that the Galaxy collapsed. *ApJ*, 136:748, Nov 1962. doi: 10.1086/147433.

N. W. Evans. The Early Merger that Made the Galaxy's Stellar Halo. *arXiv e-prints*, art. arXiv:2002.05740, Feb. 2020.

E. Fernández-Alvar, C. Allende Prieto, K. J. Schlesinger, T. C. Beers, A. C. Robin, D. P. Schneider, Y. S. Lee, D. Bizyaev, G. Ebelke, E. Malanushenko, V. Malanushenko, D. Oravetz, K. Pan, and A. Simmons. Deep SDSS optical spectroscopy of distant halo stars. II. Iron, calcium, and magnesium abundances. *A&A*, 577:A81, May 2015. doi: 10.1051/0004-6361/201425455.

A. Frebel. From Nuclei to the Cosmos: Tracing Heavy-Element Production with the Oldest Stars. *Annual Review of Nuclear and Particle Science*, 68(1):237–269, Oct. 2018. doi: 10.1146/annurev-nucl-101917-021141.

A. Frebel and J. E. Norris. Near-Field Cosmology with Extremely Metal-Poor Stars. *ARA&A*, 53:631–688, Aug 2015. doi: 10.1146/annurev-astro-082214-122423.

Gaia Collaboration, T. Prusti, J. H. J. de Bruijne, A. G. A. Brown, A. Vallenari, C. Babusiaux, C. A. L. Bailer-Jones, U. Bastian, M. Biermann, D. W. Evans, and et al. The Gaia mission. *A&A*, 595:A1, Nov. 2016. doi: 10.1051/0004-6361/201629272.

Gaia Collaboration, A. G. A. Brown, A. Vallenari, T. Prusti, J. H. J. de Bruijne, C. Babusiaux, C. A. L. Bailer-Jones, M. Biermann, D. W. Evans, L. Eyer, and et al. Gaia Data Release 2. Summary of the contents and survey properties. *A&A*, 616:A1, Aug. 2018. doi: 10.1051/0004-6361/201833051.

G. Gilmore and N. Reid. New light on faint stars - III. Galactic structure towards the South Pole and the Galactic thick disc. *MNRAS*, 202:1025–1047, Mar 1983. doi: 10.1093/mnras/202.4.1025.

J. Gu, C. Du, Y. Jia, X. Peng, Z. Wu, Y. Jing, J. Ma, X. Zhou, X. Fan, Z. Fan, Y. Jing, Z. Jiang, M. Lesser, J. Nie, S. Shen, J. Wang, H. Zou, T. Zhang, and Z. Zhou. Photometric metallicity calibration with SDSS and SCUSS and its application to distant stars in the south Galactic cap. *MNRAS*, 452(3):3092–3099, Sept. 2015. doi: 10.1093/mnras/stv1529.

M. Hampel, R. J. Stancliffe, M. Lugaro, and B. S. Meyer. The Intermediate Neutron-capture Process and Carbon-enhanced Metal-poor Stars. *ApJ*, 831(2):171, Nov. 2016. doi: 10.3847/0004-637X/831/2/171.

T. T. Hansen, J. Andersen, B. Nordström, T. C. Beers, J. Yoon, and L. A. Buchhave. The role of binaries in the enrichment of the early Galactic halo. I. r-process-enhanced metal-poor stars. *A&A*, 583:A49, Nov. 2015. doi: 10.1051/0004-6361/201526812.

T. T. Hansen, J. Andersen, B. Nordström, T. C. Beers, V. M. Placco, J. Yoon, and L. A. Buchhave. The role of binaries in the enrichment of the early Galactic halo. II. Carbon-enhanced metal-poor stars: CEMP-no stars. *A&A*, 586:A160, Feb 2016a. doi: 10.1051/0004-6361/201527235.

T. T. Hansen, J. Andersen, B. Nordström, T. C. Beers, V. M. Placco, J. Yoon, and L. A. Buchhave. The role of binaries in the enrichment of the early Galactic halo. III. Carbon-enhanced metal-poor stars - CEMP-s stars. *A&A*, 588:A3, Apr. 2016b. doi: 10.1051/0004-6361/201527409.

T. Hartwig, N. Yoshida, M. Magg, A. Frebel, S. C. O. Glover, F. A. Gómez, B. Griffen, M. N. Ishigaki, A. P. Ji, R. S. Klessen, B. W. O'Shea, and N. Tominaga. Descendants of the first stars: the distinct chemical signature of second-generation stars. *MNRAS*, 478(2):1795–1810, Aug 2018. doi: 10.1093/mnras/sty1176.

A. Helmi. Streams, substructures and the early history of the Milky Way. *arXiv e-prints*, art. arXiv:2002.04340, Feb. 2020.

A. Helmi, C. Babusiaux, H. H. Koppelman, D. Massari, J. Veljanoski, and A. G. A. Brown. The merger that led to the formation of the Milky Way's inner stellar halo and thick disk. *Nature*, 563:85–88, Nov. 2018. doi: 10.1038/s41586-018-0625-x.

A. Helmi, M. Irwin, A. Deason, E. Balbinot, V. Belokurov, J. Bland-Hawthorn, N. Christlieb, M. R. L. Cioni, S. Feltzing, E. K. Grebel, G. Kordopatis, E. Starkenburg, N. Walton, and C. C. Worley. 4MOST Consortium Survey 1: The Milky Way Halo Low-Resolution Survey. *The Messenger*, 175:23–25, Mar 2019. doi: 10.18727/0722-6691/5120.

W. Herschel. On the Construction of the Heavens. *Philosophical Transactions of the Royal Society of London Series I*, 75:213–266, Jan. 1785.

Y. Huang, B. Q. Chen, H. B. Yuan, H. W. Zhang, M. S. Xiang, C. Wang, H. F. Wang, C. Wolf, G. C. Liu, and X. W. Liu. Milky Way Tomography with the SkyMapper Southern Survey. I. Atmospheric Parameters and Distances of One Million Red Giants. *ApJS*, 243(1):7, Jul 2019. doi: 10.3847/1538-4365/ab1f72.

R. A. Ibata, G. Gilmore, and M. J. Irwin. A dwarf satellite galaxy in Sagittarius. *Nature*, 370(6486):194–196, Jul 1994. doi: 10.1038/370194a0.

Ž. Ivezić, S. M. Kahn, J. A. Tyson, B. Abel, E. Acosta, R. Allsman, D. Alonso, Y. Al-Sayyad, S. F. Anderson, J. Andrew, J. R. P. Angel, G. Z. Angeli, R. Ansari, P. Antilogus, C. Araujo, R. Armstrong, K. T. Arndt, P. Astier, É. Aubourg, N. Auza, T. S. Axelrod, D. J. Bard, J. D. Barr, A. Barrau, J. G. Bartlett, A. E. Bauer, B. J. Bauman, S. Baumont, E. Bechtol, K. Bechtol, A. C. Becker, J. Becla, C. Beldica, S. Bellavia, F. B. Bianco, R. Biswas, G. Blanc, J. Blazek, R. D. Bland ford, J. S. Bloom, J. Bogart, T. W. Bond, M. T. Booth, A. W. Borgland, K. Borne, J. F. Bosch, D. Boutigny, C. A. Brackett, A. Bradshaw, W. N. Brand t, M. E. Brown, J. S. Bullock, P. Burchat, D. L. Burke, G. Cagnoli, D. Calabrese, S. Callahan, A. L. Callen, J. L. Carlin, E. L. Carlson, S. Chand rasekharan, G. Charles-Emerson, S. Chesley, E. C. Cheu, H.-F. Chiang, J. Chiang, C. Chirino, D. Chow, D. R. Ciardi, C. F. Claver, J. Cohen-Tanugi, J. J. Cockrum, R. Coles, A. J. Connolly, K. H. Cook, A. Cooray, K. R. Covey, C. Cribbs, W. Cui, R. Cutri, P. N. Daly, S. F. Daniel, F. Daruich, G. Daubard, G. Daues, W. Dawson, F. Delgado, A. Dellapenna, R. de Peyster, M. de Val-Borro, S. W. Digel, P. Doherty, R. Dubois, G. P. Dubois-Felsmann, J. Durech, F. Economou, T. Eifler, M. Eracleous, B. L. Emmons, A. Fausti Neto, H. Ferguson, E. Figueroa, M. Fisher-Levine, W. Focke, M. D. Foss, J. Frank, M. D. Freemon, E. Gangler, E. Gawiser, J. C. Geary, P. Gee, M. Geha, C. J. B. Gessner, R. R. Gibson, D. K. Gilmore, T. Glanzman, W. Glick, T. Goldina, D. A. Goldstein, I. Goodenow, M. L. Graham, W. J. Gressler, P. Gris, L. P. Guy, A. Guyonnet, G. Haller, R. Harris, P. A. Hascall, J. Haupt, F. Hernand ez, S. Herrmann, E. Hileman, J. Hoblitt, J. A. Hodgson, C. Hogan, J. D. Howard, D. Huang, M. E. Huffer, P. Ingraham, W. R. Innes, S. H. Jacoby, B. Jain, F. Jammes, M. J. Jee, T. Jenness, G. Jernigan, D. Jevremović, K. Johns, A. S. Johnson, M. W. G. Johnson, R. L. Jones, C. Juramy-Gilles, M. Jurić, J. S. Kalirai, N. J. Kallivayalil, B. Kalmbach, J. P. Kantor, P. Karst, M. M. Kasliwal, H. Kelly, R. Kessler, V. Kinnison, D. Kirkby, L. Knox, I. V. Kotov, V. L. Krabbendam, K. S. Krughoff, P. Kubánek, J. Kuczewski, S. Kulkarni, J. Ku, N. R. Kurita, C. S. Lage, R. Lambert, T. Lange, J. B. Langton, L. Le Guillou, D. Levine, M. Liang, K.-T. Lim, C. J. Lintott, K. E. Long, M. Lopez, P. J. Lotz, R. H. Lupton, N. B. Lust, L. A. MacArthur, A. Mahabal, R. Mand elbaum, T. W. Markiewicz, D. S. Marsh, P. J. Marshall, S. Marshall, M. May, R. McKercher, M. McQueen, J. Meyers, M. Migliore, M. Miller, D. J. Mills, C. Miraval, J. Moeyens, F. E. Moolekamp, D. G. Monet, M. Moniez, S. Monkewitz, C. Montgomery, C. B. Morrison, F. Mueller, G. P. Muller, F. Muñoz Arancibia, D. R. Neill, S. P. Newbry, J.-Y. Nief, A. Nomerotski, M. Nordby, P. O'Connor, J. Oliver, S. S. Olivier, K. Olsen, W. O'Mullane, S. Ortiz, S. Osier, R. E. Owen, R. Pain, P. E. Palecek, J. K. Parejko, J. B. Parsons, N. M. Pease, J. M. Peterson, J. R. Peterson, D. L. Petravick, M. E. Libby Petrick, C. E. Petry, F. Pierfederici, S. Pietrowicz, R. Pike, P. A. Pinto, R. Plante, S. Plate, J. P. Plutchak, P. A. Price, M. Prouza, V. Radeka, J. Rajagopal, A. P. Rasmussen, N. Regnault, K. A. Reil, D. J. Reiss, M. A. Reuter, S. T. Ridgway, V. J. Riot, S. Ritz, S. Robinson, W. Roby, A. Roodman, W. Rosing, C. Roucelle, M. R. Rumore, S. Russo, A. Saha, B. Sassolas, T. L. Schalk, P. Schellart, R. H. Schindler, S. Schmidt, D. P. Schneider, M. D. Schneider, W. Schoening, G. Schumacher, M. E. Schwamb, J. Sebag, B. Selvy, G. H. Sembroski, L. G. Seppala, A. Serio, E. Serrano, R. A. Shaw, I. Shipsey, J. Sick, N. Silvestri, C. T. Slater, J. A. Smith, R. C. Smith, S. Sobhani, C. Soldahl, L. Storrie-Lombardi, E. Stover, M. A. Strauss, R. A. Street, C. W. Stubbs, I. S. Sullivan, D. Sweeney, J. D. Swinbank, A. Szalay, P. Takacs, S. A. Tether, J. J. Thaler, J. G. Thayer, S. Thomas, A. J. Thornton, V. Thukral, J. Tice, D. E. Trilling, M. Turri, R. Van Berg, D. Vanden Berk, K. Vetter, F. Virieux, T. Vucina, W. Wahl, L. Walkowicz, B. Walsh, C. W. Walter, D. L. Wang, S.-Y. Wang, M. Warner, O. Wiecha, B. Willman, S. E. Winters, D. Wittman, S. C. Wolff, W. M. Wood-Vasey, X. Wu, B. Xin, P. Yoachim, and H. Zhan. LSST: From Science Drivers to Reference Design and Anticipated Data Products. *ApJ*, 873(2):111, Mar 2019. doi: 10.3847/1538-4357/ab042c.

W. Janesh, H. L. Morrison, Z. Ma, C. Rockosi, E. Starkenburg, X. X. Xue, H.-W. Rix, P. Harding, T. C. Beers, and J. Johnson. The SEGUE K Giant Survey. III. Quantifying Galactic Halo Substructure. *ApJ*, 816(2):80, Jan 2016. doi: 10.3847/0004-637X/816/2/80.

D. Kawata, J. Bovy, N. Matsunaga, and J. Baba. Galactic rotation from Cepheids with Gaia DR2 and effects of non-axisymmetry. *MNRAS*, 482(1):40–51, Jan. 2019. doi: 10.1093/mnras/sty2623.

S. C. Keller, B. P. Schmidt, M. S. Bessell, P. G. Conroy, P. Francis, A. Granlund, E. Kowald, A. P. Oates, T. Martin-Jones, T. Preston, P. Tisserand , A. Vaccarella, and M. F. Waterson. The SkyMapper Telescope and The Southern Sky Survey. *PASA*, 24(1):1–12, May 2007. doi: 10.1071/AS07001.

F. J. Kerr and D. Lynden-Bell. Review of galactic constants. *MNRAS*, 221:1023–1038, Aug 1986. doi: 10.1093/mnras/221.4.1023.

Y. K. Kim, Y. S. Lee, and T. C. Beers. Dependence of Galactic Halo Kinematics on the Adopted Galactic Potential. *ApJ*, 882(2):176, Sep 2019. doi: 10.3847/1538-4357/ab3660.

Y. S. Lee, T. C. Beers, T. Sivarani, C. Allende Prieto, L. Koesterke, R. Wilhelm, P. Re Fiorentin, C. A. L. Bailer-Jones, J. E. Norris, C. M. Rockosi, B. Yanny, H. J. Newberg, K. R. Covey, H.-T. Zhang, and A. L. Luo. The SEGUE Stellar Parameter Pipeline. I. Description and Comparison of Individual Methods. *AJ*, 136(5):2022–2049, Nov 2008. doi: 10.1088/0004-6256/136/5/2022.

Y. S. Lee, T. C. Beers, T. Masseron, B. Plez, C. M. Rockosi, J. Sobeck, B. Yanny, S. Lucatello, T. Sivarani, V. M. Placco, and D. Carollo. Carbon-enhanced Metal-poor Stars in SDSS/SEGUE. I. Carbon Abundance Estimation and Frequency of CEMP Stars. *AJ*, 146(5):132, Nov. 2013. doi: 10.1088/0004-6256/146/5/132.

Y. S. Lee, T. C. Beers, Y. K. Kim, V. Placco, J. Yoon, D. Carollo, T. Masseron, and J. Jung. Chemical Cartography. I. A Carbonicity Map of the Galactic Halo. *ApJ*, 836(1):91, Feb 2017. doi: 10.3847/1538-4357/836/1/91.

Y. S. Lee, T. C. Beers, and Y. K. Kim. Chemical Cartography. II. The Assembly History of the Galactic Stellar Halo Traced by Carbon-enhanced Metal-poor Stars. *ApJ*, 885(2):102, Nov 2019. doi: 10.3847/1538-4357/ab4791.

H. Li, K. Tan, and G. Zhao. A Catalog of 10,000 Very Metal-poor Stars from LAMOST DR3. *ApJS*, 238(2):16, Oct 2018. doi: 10.3847/1538-4365/aada4a.

J. Lian, D. Thomas, C. Maraston, T. C. Beers, C. Moni Bidin, J. G. Fernández-Trincado, D. A. García-Hernández, R. R. Lane, R. R. Munoz, C. Nitschelm, A. r. Roman-Lopes, and O. Zamora. The age-chemical abundance structure of the Galactic disc - II. α-dichotomy and thick disc formation. *MNRAS*, 497(2):2371–2384, July 2020. doi: 10.1093/mnras/staa2078.

S. Lucatello, S. Tsangarides, T. C. Beers, E. Carretta, R. G. Gratton, and S. G. Ryan. The Binary Frequency Among Carbon-enhanced, s-Process-rich, Metal-poor Stars. *ApJ*, 625(2):825–832, June 2005. doi: 10.1086/428104.

S. R. Majewski, R. P. Schiavon, P. M. Frinchaboy, C. Allende Prieto, R. Barkhouser, D. Bizyaev, B. Blank, S. Brunner, A. Burton, R. Carrera, S. D. Chojnowski, K. Cunha, C. Epstein, G. Fitzgerald, A. E. García Pérez, F. R. Hearty, C. Henderson, J. A. Holtzman, J. A. Johnson, C. R. Lam, J. E. Lawler, P. Maseman, S. Mészáros, M. Nelson, D. C. Nguyen, D. L. Nidever, M. Pinsonneault, M. Shetrone, S. Smee, V. V. Smith, T. Stolberg, M. F. Skrutskie, E. Walker, J. C. Wilson, G. Zasowski, F. Anders, S. Basu, S. Beland, M. R. Blanton, J. Bovy, J. R. Brownstein, J. Carlberg, W. Chaplin, C. Chiappini, D. J. Eisenstein, Y. Elsworth, D. Feuillet, S. W. Fleming, J. Galbraith-Frew, R. A. García, D. A. García-Hernández, B. A. Gillespie, L. Girardi, J. E. Gunn, S. Hasselquist, M. R. Hayden, S. Hekker, I. Ivans, K. Kinemuchi, M. Klaene, S. Mahadevan, S. Mathur, B. Mosser, D. Muna, J. A. Munn, R. C. Nichol, R. W. O'Connell, J. K. Parejko, A. C. Robin, H. Rocha-Pinto, M. Schultheis, A. M. Serenelli, N. Shane, V. Silva Aguirre, J. S. Sobeck, B. Thompson, N. W. Troup, D. H. Weinberg, and O. Zamora. The Apache Point Observatory Galactic Evolution Experiment (APOGEE). *AJ*, 154(3):94, Sept. 2017. doi: 10.3847/1538-3881/aa784d.

T. Matsuno, W. Aoki, and T. Suda. Origin of the Excess of High-energy Retrograde Stars in the Galactic Halo. *ApJ*, 874(2):L35, Apr 2019. doi: 10.3847/2041-8213/ab0ec0.

D. Mihalas. *Galactic astronomy : structure and kinematics of galaxies*. W.H. Freeman, San Francisco, 2nd ed.. edition, 1981. ISBN 0716712806.

H. L. Morrison, C. Flynn, and K. C. Freeman. Where Does the Disk Stop and the Halo Begin - Kinematics in a Rotation Field. *AJ*, 100:1191, Oct. 1990. doi: 10.1086/115587.

G. C. Myeong, N. W. Evans, V. Belokurov, J. L. Sand ers, and S. E. Koposov. The Sausage Globular Clusters. *ApJ*, 863(2):L28, Aug 2018. doi: 10.3847/2041-8213/aad7f7.

G. C. Myeong, E. Vasiliev, G. Iorio, N. W. Evans, and V. Belokurov. Evidence for two early accretion events that built the Milky Way stellar halo. *MNRAS*, 488(1): 1235–1247, Sep 2019. doi: 10.1093/mnras/stz1770.

J. E. Norris. Population Studies. XII. The Duality of the Galactic Halo. *ApJ*, 431: 645, Aug. 1994. doi: 10.1086/174516.

D. A. Ostlie and B. W. Carroll. *An Introduction to Modern Stellar Astrophysics*. Addison-Wesley Pub., 1996. ISBN 0201598809.

M. A. C. Perryman, L. Lindegren, J. Kovalevsky, E. Hog, U. Bastian, P. L. Bernacca, M. Creze, F. Donati, M. Grenon, M. Grewing, F. van Leeuwen, H. van der Marel, F. Mignard, C. A. Murray, R. S. Le Poole, H. Schrijver, C. Turon, F. Arenou, M. Froeschle, and C. S. Petersen. The Hipparcos Catalogue. *A&A*, 500:501–504, July 1997.

V. M. Placco, A. Frebel, T. C. Beers, and R. J. Stancliffe. Carbon-enhanced Metal-poor Star Frequencies in the Galaxy: Corrections for the Effect of Evolutionary Status on Carbon Abundances. *ApJ*, 797(1):21, Dec. 2014. doi: 10.1088/0004-637X/797/1/21.

V. M. Placco, A. Frebel, T. C. Beers, J. Yoon, A. Chiti, A. Heger, C. Chan, A. R. Casey, and N. Christlieb. Observational Constraints on First-Star Nucleosynthesis. II. Spectroscopy of an Ultra metal-poor CEMP-no Star. *ApJ*, 833(1):21, Dec. 2016. doi: 10.3847/0004-637X/833/1/21.

I. U. Roederer, V. M. Placco, and T. C. Beers. Detection of Phosphorus, Sulphur, and Zinc in the Carbon-enhanced Metal-poor Star BD+44 493. *ApJL*, 824(2):L19, June 2016. doi: 10.3847/2041-8205/824/2/L19.

S. Roeser, M. Demleitner, and E. Schilbach. The ppmxl catalog of positions and proper motions on the icrs. combining usno-b1.0 and the two micron all sky survey (2mass). *The Astronomical Journal*, 139(6):2440–2447, Apr 2010. ISSN 1538-3881. doi: 10.1088/0004-6256/139/6/2440. URL `http://dx.doi.org/10.1088/0004-6256/139/6/2440`.

S. G. Ryan and A. J. Norton. *Stellar Evolution and Nucleosynthesis*. Cambridge University Press, 2010. ISBN 9780521196093.

S. Salvadori, A. Ferrara, R. Schneider, E. Scannapieco, and D. Kawata. Mining the Galactic halo for very metal-poor stars. *MNRAS*, 401(1):L5–L9, Jan 2010. doi: 10.1111/j.1745-3933.2009.00772.x.

R. Schönrich, J. Binney, and W. Dehnen. Local kinematics and the local standard of rest. *MNRAS*, 403(4):1829–1833, Apr. 2010. doi: 10.1111/j.1365-2966.2010.16253.x.

R. Schönrich, M. Asplund, and L. Casagrande. On the alleged duality of the Galactic halo. *MNRAS*, 415(4):3807–3823, Aug. 2011. doi: 10.1111/j.1365-2966.2011.19003.x.

R. Schönrich, P. McMillan, and L. Eyer. Distances and parallax bias in Gaia DR2. *MNRAS*, 487(3):3568–3580, Aug. 2019. doi: 10.1093/mnras/stz1451.

M. Schwarzschild and B. Schwarzschild. A Spectroscopic Comparison Between - and Low-Velocity F Dwarfs. *ApJ*, 112:248, Sept. 1950. doi: 10.1086/145340.

L. Searle and R. Zinn. Composition of halo clusters and the formation of the galactic halo. *ApJ*, 225:357–379, Oct 1978. doi: 10.1086/156499.

F. Sestito, N. Longeard, N. F. Martin, E. Starkenburg, M. Fouesneau, J. I. González Hernández, A. Arentsen, R. Ibata, D. S. Aguado, R. G. Carlberg, P. Jablonka, J. F. Navarro, E. Tolstoy, and K. A. Venn. Tracing the formation of the Milky Way through ultra metal-poor stars. *MNRAS*, 484(2):2166–2180, Apr. 2019. doi: 10.1093/mnras/stz043.

F. Sestito, N. F. Martin, E. Starkenburg, A. Arentsen, R. A. Ibata, N. Longeard, C. Kielty, K. Youakim, K. A. Venn, D. S. Aguado, R. G. Carlberg, J. I. González Hernández, V. Hill, P. Jablonka, G. Kordopatis, K. Malhan, J. F. Navarro, R. Sánchez-Janssen, G. Thomas, E. Tolstoy, T. G. Wilson, P. A. Palicio, S. Bialek, R. Garcia-Dias, R. Lucchesi, P. North, Y. Osorio, L. R. Patrick, and L. Peralta de Arriba. The Pristine survey X: a large population of low-metallicity stars permeates the Galactic disk. *MNRAS*, Feb. 2020. doi: 10.1093/mnrasl/slaa022.

J. Sommer-Larsen and C. Zhen. Armchair cartography - a map of the galactic halo based on observationsof local, metal-poor stars. *MNRAS*, 242:10–24, Jan 1990. doi: 10.1093/mnras/242.1.10.

J. Sommer-Larsen, T. C. Beers, C. Flynn, R. Wilhelm, and P. R. Christensen. A Dynamical and Kinematic Model of the Galactic Stellar Halo and Possible Implications for Galaxy Formation Scenarios. *ApJ*, 481(2):775–781, May 1997. doi: 10.1086/304081.

E. Starkenburg, K. A. Oman, J. F. Navarro, R. A. Crain, A. Fattahi, C. S. Frenk, T. Sawala, and J. Schaye. The oldest and most metal-poor stars in the APOSTLE Local Group simulations. *MNRAS*, 465(2):2212–2224, Feb 2017. doi: 10.1093/mnras/stw2873.

P. B. Tissera, T. C. Beers, D. Carollo, and C. Scannapieco. Stellar haloes in Milky Way mass galaxies: from the inner to the outer haloes. *MNRAS*, 439(3):3128–3138, Apr 2014. doi: 10.1093/mnras/stu181.

E. B. Wilson. Probable inference, the law of succession, and statistical inference. *Journal of the American Statistical Association*, 22(158):209–212, 1927. doi: 10.1080/01621459.1927.10502953. URL `https://www.tandfonline.com/doi/abs/10.1080/01621459.1927.10502953`.

C. Wolf, C. A. Onken, L. C. Luvaul, B. P. Schmidt, M. S. Bessell, S.-W. Chang, G. S. Da Costa, D. Mackey, T. Martin-Jones, S. J. Murphy, T. Preston, R. A. Scalzo, L. Shao, J. Smillie, P. Tisserand, M. C. White, and F. Yuan. SkyMapper Southern Survey: First Data Release (DR1). *PASA*, 35:e010, Feb. 2018a. doi: 10.1017/pasa.2018.5.

C. Wolf, C. A. Onken, L. C. Luvaul, B. P. Schmidt, M. S. Bessell, S.-W. Chang, G. S. Da Costa, D. Mackey, T. Martin-Jones, S. J. Murphy, T. Preston, R. A. Scalzo, L. Shao, J. Smillie, P. Tisserand, M. C. White, and F. Yuan. SkyMapper Southern Survey: First Data Release (DR1). *PASA*, 35:e010, Feb 2018b. doi: 10.1017/pasa.2018.5.

B. Yanny, C. Rockosi, H. J. Newberg, G. R. Knapp, J. K. Adelman-McCarthy, B. Alcorn, S. Allam, C. Allende Prieto, D. An, K. S. J. Anderson, S. Anderson, C. A. L. Bailer-Jones, S. Bastian, T. C. Beers, E. Bell, V. Belokurov, D. Bizyaev, N. Blythe, J. J. Bochanski, W. N. Boroski, J. Brinchmann, J. Brinkmann, H. Brewington, L. Carey, K. M. Cudworth, M. Evans, N. W. Evans, E. Gates, B. T. Gänsicke, B. Gillespie, G. Gilmore, A. Nebot Gomez-Moran, E. K. Grebel, J. Greenwell, J. E. Gunn, C. Jordan, W. Jordan, P. Harding, H. Harris, J. S. Hendry, D. Holder, I. I. Ivans, Ž. Ivezič, S. Jester, J. A. Johnson, S. M. Kent, S. Kleinman, A. Kniazev, J. Krzesinski, R. Kron, N. Kuropatkin, S. Lebedeva, Y. S. Lee, R. French Leger, S. Lépine, S. Levine, H. Lin, D. C. Long, C. Loomis, R. Lupton, O. Malanushenko, V. Malanushenko, B. Margon, D. Martinez-Delgado, P. McGehee, D. Monet, H. L. Morrison, J. A. Munn, J. Neilsen, Eric H., A. Nitta, J. E. Norris, D. Oravetz, R. Owen, N. Padmanabhan, K. Pan, R. S. Peterson, J. R. Pier, J. Platson, P. Re Fiorentin, G. T. Richards, H.-W. Rix, D. J. Schlegel, D. P. Schneider, M. R. Schreiber, A. Schwope, V. Sibley, A. Simmons, S. A. Snedden, J. Allyn Smith, L. Stark, F. Stauffer, M. Steinmetz, C. Stoughton, M. SubbaRao, A. Szalay, P. Szkody, A. R. Thakar, T. Sivarani, D. Tucker, A. Uomoto, D. Vanden Berk, S. Vidrih, Y. Wadadekar, S. Watters, R. Wilhelm, R. F. G. Wyse, J. Yarger, and D. Zucker. SEGUE: A Spectroscopic Survey of 240,000 Stars with g = 14-20. *AJ*, 137(5):4377–4399, May 2009. doi: 10.1088/0004-6256/137/5/4377.

J. Yoon, T. C. Beers, V. M. Placco, K. C. Rasmussen, D. Carollo, S. He, T. T. Hansen, I. U. Roederer, and J. Zeanah. Observational Constraints on First-star Nucleosynthesis. I. Evidence for Multiple Progenitors of CEMP-No Stars. *ApJ*, 833 (1):20, Dec 2016. doi: 10.3847/0004-637X/833/1/20.

J. Yoon, T. C. Beers, S. Dietz, Y. S. Lee, V. M. Placco, G. Da Costa, S. Keller, C. I. Owen, and M. Sharma. Galactic Archeology with the AEGIS Survey: The Evolution of Carbon and Iron in the Galactic Halo. *ApJ*, 861(2):146, Jul 2018. doi: 10.3847/1538-4357/aaccea.

J. Yoon, T. C. Beers, D. Tian, and D. D. Whitten. Origin of the CEMP-no Group Morphology in the Milky Way. *ApJ*, 878(2):97, Jun 2019. doi: 10.3847/1538-4357/ab1ead.

J. Yoon, D. D. Whitten, T. C. Beers, Y. S. Lee, T. Masseron, and V. M. Placco. Identification of a Group III CEMP-no Star in the Dwarf Spheroidal Galaxy Canes Venatici I. *ApJ*, 894(1):7, May 2020. doi: 10.3847/1538-4357/ab7daf.

D. G. York, J. Adelman, J. Anderson, John E., S. F. Anderson, J. Annis, N. A. Bahcall, J. A. Bakken, R. Barkhouser, S. Bastian, E. Berman, W. N. Boroski, S. Bracker, C. Briegel, J. W. Briggs, J. Brinkmann, R. Brunner, S. Burles, L. Carey, M. A. Carr, F. J. Castander, B. Chen, P. L. Colestock, A. J. Connolly, J. H. Crocker, I. Csabai, P. C. Czarapata, J. E. Davis, M. Doi, T. Dombeck, D. Eisenstein, N. Ellman, B. R. Elms, M. L. Evans, X. Fan, G. R. Federwitz, L. Fiscelli, S. Friedman, J. A. Frieman, M. Fukugita, B. Gillespie, J. E. Gunn, V. K. Gurbani, E. de Haas, M. Haldeman, F. H. Harris, J. Hayes, T. M. Heckman, G. S. Hennessy, R. B. Hindsley, S. Holm, D. J. Holmgren, C.-h. Huang, C. Hull, D. Husby, S.-I. Ichikawa, T. Ichikawa, Ž. Ivezić, S. Kent, R. S. J. Kim, E. Kinney, M. Klaene, A. N. Kleinman, S. Kleinman, G. R. Knapp, J. Korienek, R. G. Kron, P. Z. Kunszt, D. Q. Lamb, B. Lee, R. F. Leger, S. Limmongkol, C. Lindenmeyer, D. C. Long, C. Loomis, J. Loveday, R. Lucinio, R. H. Lupton, B. MacKinnon, E. J. Mannery, P. M. Mantsch, B. Margon, P. McGehee, T. A. McKay, A. Meiksin, A. Merelli, D. G. Monet, J. A. Munn, V. K. Narayanan, T. Nash, E. Neilsen, R. Neswold, H. J. Newberg, R. C. Nichol, T. Nicinski, M. Nonino, N. Okada, S. Okamura, J. P. Ostriker, R. Owen, A. G. Pauls, J. Peoples, R. L. Peterson, D. Petravick, J. R. Pier, A. Pope, R. Pordes, A. Prosapio, R. Rechenmacher, T. R. Quinn, G. T. Richards, M. W. Richmond, C. H. Rivetta, C. M. Rockosi, K. Ruthmansdorfer, D. Sand ford, D. J. Schlegel, D. P. Schneider, M. Sekiguchi, G. Sergey, K. Shimasaku, W. A. Siegmund, S. Smee, J. A. Smith, S. Snedden, R. Stone, C. Stoughton, M. A. Strauss, C. Stubbs, M. SubbaRao, A. S. Szalay, I. Szapudi, G. P. Szokoly, A. R. Thakar, C. Tremonti, D. L. Tucker, A. Uomoto, D. Vanden Berk, M. S. Vogeley, P. Waddell, S.-i. Wang, M. Watanabe, D. H. Weinberg, B. Yanny, N. Yasuda, and SDSS Collaboration. The Sloan Digital Sky Survey: Technical Summary. *AJ*, 120(3): 1579–1587, Sep 2000. doi: 10.1086/301513.

Y. Yoshii. Density distribution of faint stars in the direction of the north galactic pole. *PASJ*, 34:365–379, Jan 1982.

K. Youakim, E. Starkenburg, D. S. Aguado, N. F. Martin, M. Fouesneau, J. I. González Hernández, C. Allende Prieto, P. Bonifacio, M. Gentile, C. Kielty, P. Côté, P. Jablonka, A. McConnachie, R. Sánchez Janssen, E. Tolstoy, and K. Venn. The Pristine survey - III. Spectroscopic confirmation of an efficient search for extremely metal-poor stars. *MNRAS*, 472(3):2963–2974, Dec. 2017. doi: 10.1093/mnras/stx2005.

Z. Yuan, G. C. Myeong, T. C. Beers, N. W. Evans, Y. S. Lee, P. Banerjee, D. Gudin, K. Hattori, H. Li, T. Matsuno, V. M. Placco, M. C. Smith, D. D. Whitten, and G. Zhao. Dynamical Relics of the Ancient Galactic Halo. *ApJ*, 891(1):39, Mar. 2020. doi: 10.3847/1538-4357/ab6ef7.

N. Zacharias, C. T. Finch, T. M. Girard, A. Henden, J. L. Bartlett, D. G. Monet, and M. I. Zacharias. The fourth us naval observatory ccd astrograph catalog (ucac4). *The Astronomical Journal*, 145(2):44, Jan 2013. ISSN 1538-3881. doi: 10.1088/0004-6256/145/2/44. URL `http://dx.doi.org/10.1088/0004-6256/145/2/44`.

G. Zhao, Y.-H. Zhao, Y.-Q. Chu, Y.-P. Jing, and L.-C. Deng. LAMOST spectral survey — An overview. *Research in Astronomy and Astrophysics*, 12(7):723–734, July 2012. doi: 10.1088/1674-4527/12/7/002.